THE UNIVERSITY OF CHICAGO

LIVING BIOELECTRONIC INTERFACE FOR INFLAMMATION AND INFECTION MANAGEMENT

A DISSERTATION SUBMITTED TO

THE FACULTY OF THE DIVISION OF THE PHYSICAL SCIENCES

IN CANDIDACY FOR THE DEGREE OF

DOCTOR OF PHILOSOPHY

DEPARTMENT OF CHEMISTRY

BY

SAEHYUN KIM

CHICAGO, ILLINOIS

AUGUST 2025

DEDICATION

To my beloved family and friends above and below

Table of Contents

List of Figures

List of Tables

Acknowledgements

Reflecting on my years at the University of Chicago, I am filled with immense gratitude for an experience shaped by curiosity, collaboration, and growth. The journey through both research and personal challenges was made meaningful by the incredible people who walked alongside me. This dissertation is not solely the result of my own effort—it represents the collective dedication, insight, and support of many.

I was privileged to work in an environment where collaboration thrived, surrounded by talented researchers whose contributions helped shape the path of this work. Among them, the most profound gratitude goes to my advisor, Dr. Bozhi Tian. His consistent support, thoughtful mentorship, and belief in my ideas were instrumental in bringing this research to life. Bozhi's warmth, encouragement, and genuine care extended beyond science—he has been both a mentor and a guide, fostering a lab culture that inspired creativity and camaraderie.

I am also thankful to my thesis committee: Dr. Bozhi Tian, Dr. Anna Wuttig, and Dr. Bryan Dickinson. Their insightful feedback and guidance greatly improved this work, and I am honored to have had their expertise in shaping my doctoral journey.

Many others at UChicago made these years unforgettable. I extend my thanks to Dr. Jiuyun Shi, Dr. Jiping Yue, Dr. Pengju Li, Dr. Changxu Sun, Dr. Jingcheng Ma, Dr. Ananth Kamath, Dr. Chuanwang Yang, Wen Li, and Zhe Cheng. Your companionship—both in the lab and outside it—has left a lasting impression on me.

To the friends I met during my first year, above and below, thank you for sharing in moments of joy and standing by me during the more difficult times. Your presence gave me strength and reminded me of the power of the community.

Lastly, I owe everything to my family. Their unwavering love has grounded me throughout this journey. My deepest thanks to Eunju Jang and Myeongsu Kim, my parents, and to my grandparents—for your constant support, patience, and encouragement. This accomplishment is as much yours as it is mine

Abstract

The field of bioelectronics bridges biology, electronics, and materials science to create devices that can sense and stimulate biological systems. These technologies enable early disease detection, personalized healthcare, and therapeutic intervention. Recently, the mismatch between rigid electronic components and dynamic, adaptive biological tissues has prompted a shift toward incorporating living materials (LMs) into bioelectronic systems.

Living materials—comprising of live microorganisms—exhibit adaptive, responsive properties reminiscent of living systems. Being innately bioactive, adaptive and capable of sensing their environment, LMs serve as active platforms for biosensing and regenerative medicine. Their integration with bioelectronics offers a path toward soft, bioactive, and reconfigurable devices for disease management.

This thesis investigates strategies for constructing living bioelectronic interfaces aimed at controlling inflammation and infection.

Chapter 2 explores the use of LMs as bioactive interfacial components for immunomodulation. We developed a system called *Active Bio-Integrated Living Electronics* (ABLE), which combines a bioelectronic framework with a hydrogel composite encapsulating *Staphylococcus epidermidis*. This living interface enables microbial-driven intervention in psoriasis through the release of bioactive compounds. The hydrogel, prepared by thermally releasing amylose polymers, maintains bacterial viability through its viscoelastic extracellular matrix. When combined with electrophysiological and wireless sensors, ABLE enables simultaneous treatment and monitoring of inflammatory skin disease.

Chapter 3 investigates how bioelectronics and LMs interact by studying microbial response at an electrified interface. Using a microelectronic platform, we uncovered an excitatory response in *S. epidermidis*, revealing that electrical stimuli from device can reversibly alter bacterial membrane potential. Remarkably, this excitability only emerged under acidic pH of healthy skin, suggesting that the bacterium's electrical responsiveness is environmentally gated. This phenomenon enabled targeted suppression of

biofilm formation using low, non-lethal voltages—offering a programmable and energy-efficient strategy for infection control.

Together, these studies demonstrate the potential of living biointerfaces in managing complex biological conditions. Looking forward, we anticipate that integration strategies between living and non-living components will continue to evolve, unlocking richer interactions and broader therapeutic applications.

Chapter 1. Introduction

*Chapter 1 adopts figures and text from ref (1): **Kim, S**.; Eig, E.; Tian, B. The Convergence of Bioelectronics and Engineered Living Materials. *Cell Reports Phys. Sci.* 2024, *5*, 102149.

1.1. Bioelectronics and living materials in healthcare

Bioelectronics is an interdisciplinary domain that combines biology, electronics, and materials science to design technologies capable of interacting with living tissues. These systems can both detect and influence biological activity, offering powerful tools for early diagnosis and tailored healthcare solutions. With their ability to capture physiological signals with high precision, bioelectronic devices are being developed not only for therapeutic interventions—such as restoring motor or sensory function and modulating neural circuits—but also for non-invasive diagnostics, continuous health monitoring, and personalized treatment strategies.[2,3]

Recent advances in bioelectronics focus on integrating living features like responsiveness, adaptability, memory, and self-healing capabilities. By re-creating adaptive and self-repairing properties of living systems, bioelectronic devices resist environmental stress and device fatigue, prolonging their lifespan.[4] Incorporating tissue-like properties such as softness, programmability, anisotropy, and strain stiffening allows seamless integration with biological tissues and prevents damage due to mechanical mismatch[5,6] The integration of memristors in bioelectronics enables new functionalities like neuromorphic computing and power-efficient data compression.[7] However, mimicking natural features with purely synthetic materials poses significant challenges. Therefore, integration of living materials (LMs) emerged as a new strategy to realizing dynamic living functionalities in bioelectronics.

The field of living materials (LMs) aims to recreate functional and responsive properties of life utilizing live microorganisms in a suitable vehicle. LMs are bioactive, perceive changes in their surroundings and dynamically reconfigure their properties, serving various purposes in biosensing and disease treatment[8,9] **Section 1.2** and **1.3** describes how the two fields – bioelectronics and LMs – struggles to imitate nature's

dynamic living properties on their own. **Section 1.4** describes the limited attempts at combining the two fields to create living bioelectronics and the synergies derived from it.

1.2 Strategies to impart living features in bioelectronics

The rigid inorganic materials used in bioelectronic devices often struggle to interface effectively with soft, dynamic, and responsive living tissues. Additionally, the requirement for power often leads to the use of large, bulky batteries, which in turn reduces their lifespan.[10] To address these challenges, exploring living characteristics within bioelectronics has emerged as a key focus for the next generation of this field. Traditional efforts have largely focused on blending stretchability and tissue-like viscoelasticity to improve biointerfaces.[11] However, integrating additional living attributes such as self-healing, adaptability, and memory shows promise in creating highly resilient, energy-efficient, and intelligent bioelectronic systems. This section introduces selected material engineering approaches aimed at incorporating living features into bioelectronics.

1.2.1. Self-healing and regeneration

The introduction of self-healing features in bioelectronics offers the potential to repair physical damage and restore previous properties and functionalities. One notable example is a self-healing material developed by Cooper et al., which used a polymeric material composed of alternating layers of polydimethylsiloxane and polypropylene glycol, each containing bisurea groups that confer self-healing capacity (**Figure 1-1A**).[12] The immiscible backbones of these polymers facilitated surface tension-mediated realignment, while their dynamic bisurea bonds enabled self-healing at higher temperatures. By incorporating insulating $SrTiO_3$ microparticles and conductive carbon nanoparticles (NPs), they created a pressure sensor that maintained sensing capacity despite misalignment, recovering nearly 96% of its capacitance through heat-stimulated realignment. Magnetic NdFeB nanoflakes provided external control over the realignment and healing process using a magnetic field. Other self-healing materials, enabled by

reversible hydrogen bonding and metal-coordination bonding,[13,14] have greatly improved fatigue resistance and long-term stability of bioelectronic devices.

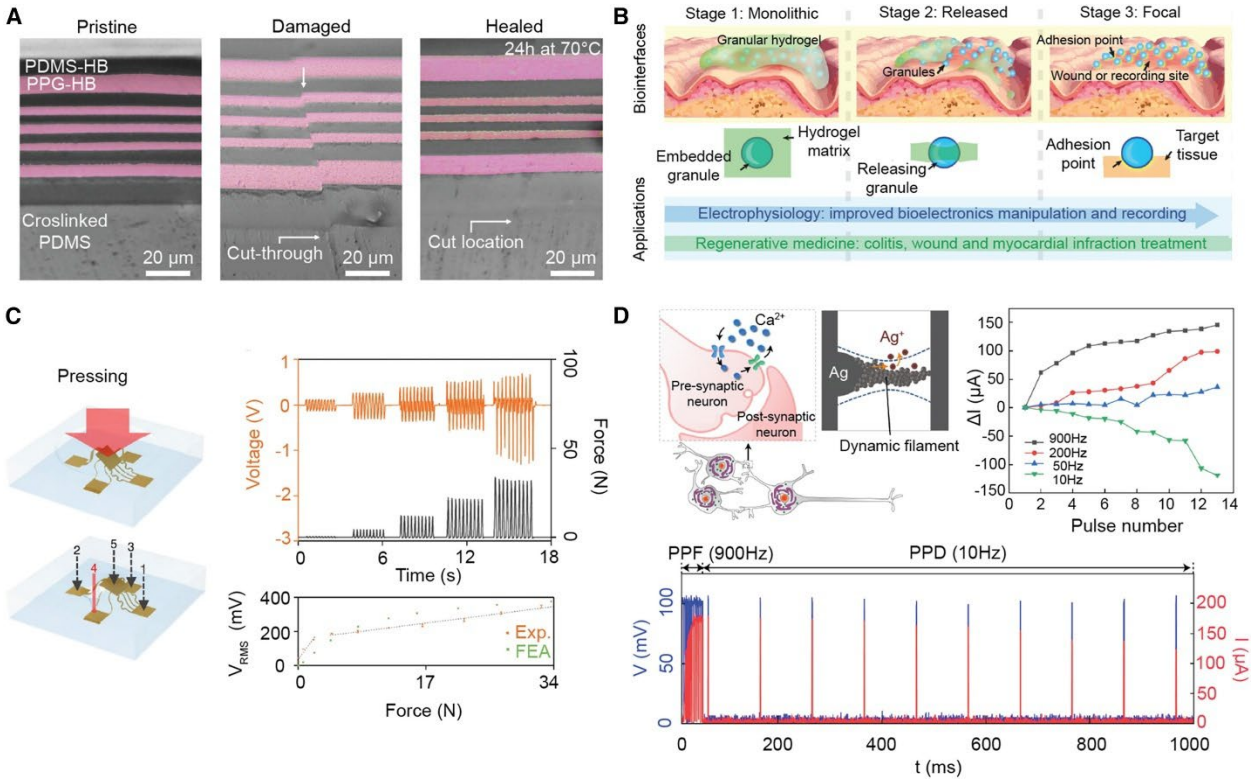

Figure 1-1. Material design strategies to impart living features in bioelectronics A. Differential miscibility drives surface tension-mediated realignment and self-healing of a multilayer material for bioelectronics. Reproduced with permission from Cooper et al., copyright 2023, AAAS.[12] **B.** Granules embedded in a gelatin matrix are released when exposed to body temperature, forming a focal biointerface that facilitates electrophysiology recording. Reproduced with permission from Shi et al., copyright 2024, Springer Nature.[15] **C.** Vibrations from movement allow piezoelectric generators to automatically harvest energy. Reproduced with permission from Han et al., copyright 2019, Springer Nature. **D.** Diffusion of AgNPs creates memory within memristive circuits through repeated electrical stimulation. Reproduced with permission from Fu et al., copyright 2020, Springer Nature.[16]

1.2.2 Stimuli-responsiveness

Bioelectronics mimic the ability of biological systems to respond to stimuli, adapting their function on demand. This capability is particularly useful for improving the conformity of the biointerface, which enhances signal recording efficacy, and for extending device lifespan by responding to changes in tissue conditions. For instance, Shi et al. developed a dynamic hydrogel matrix composed of gelatin that can dissolve and release starch granules in response to temperature and pH changes.[15] When the gelatin matrix dissolves upon exposure to physiological temperature, the released starch granules create a localized, cell-scale biointerface. By chemically altering the granules with therapeutic molecules, the researchers facilitated applications like wound healing and electrocardiogram signal recording (**Figure 1-1B**).

Another approach, by Jiao et al., involved developing a device that adjusts its shape and mechanical properties to match the target organ automatically in response to thermal stimuli.[17] Heating the device to body temperature softened the shape memory polymer substrate, allowing implantation through small incisions and improving conformity to the tissue it interfaces with. This enhances the effectiveness of its electrodes for temperature, potential, and pH sensing, crucial for diagnosing conditions like epilepsy or pericardial effusion. The substrate retains sufficient strength to maintain its shape over extended periods, thereby enhancing durability.

1.2.3 Self-powered system

Bioelectronic devices that generate their own power or harvest energy from their surroundings simplify integration with biological systems by eliminating bulky batteries and external wiring. For example, Han et al. developed self-powered bioelectronic devices using a three-dimensional (3D) piezoelectric generator that captures energy from natural animal movements (**Figure 1-1C**).[18] They employed a serpentine-shaped polyvinylidene difluoride generator with sandwiched electrodes, generating voltage from in-plane vibrations and out-of-plane oscillations. When implanted in a rodent's hind leg, this setup enabled energy harvesting from movement, thus enabling autonomous operation. In another study,

researchers reported thermoelectric generators consisting of Bi and Sb chalcogenides and Au-Ge electrodes that can generate power through the temperature difference between the body and surrounding air.[19] Photovoltaic generators have also been employed to generate energy through ambient light.[20]

1.2.4 Programmability

The ability to store information for long-term use is a crucial feature in permanent or implantable bioelectronics. This can be achieved through memristors, devices capable of retaining the amount of charge that flows through them. Fu et al. developed diffusive memristors designed to operate at biological voltages of 40–100 mV.[16] When an electrical signal passes through the memristor, it triggers the diffusion of AgNPs, forming a conductive filament (**Figure 1-1D**). This process is facilitated by protein nanowire-catalyzed reduction of Ag. Repeated stimulation enhances or depresses current, mimicking synaptic plasticity. These artificial neurons replicate temporal and spatial summation, showing potential for power-efficient bio-computing. In addition to electrical stimulation, repeated mechanical stretching can program the bulk electrical properties of bioelectronic devices. For instance, Lipomi et al. demonstrated reversible alterations in the material's electrical conductivity through strain-induced realignment of carbon nanofibers.[21]

1.3. Strategies to impart living features in LMs

In the preceding section, we briefly explored how bioelectronics achieve living properties through material engineering approaches. In contrast, LMs manifest living properties by incorporating functional microorganisms, typically into a synthetic or naturally occurring matrices. Genetic engineering of functional microorganisms and clever design of encapsulating matrix have advanced the application of LMs in biosensing and regenerative medicine. The following section details strategies for replicating living characteristics within LMs.

1.3.1 Programmability

LMs aim to replicate the programmability of natural systems by designing materials that can reconfigure their mechanical and biocatalytic properties. Gilbert et al. created LMs through a co-culture of

genetically programmed Saccharomyces cerevisiae and bacteriocellulose-producing *Komagataeibacter rhaeticus*.[22] *S. cerevisiae* secreted enzymes that functionalized the matrix, thereby altering the material's properties. The introduction of catalytic enzymes enabled the oxidation of environmental pollutants, while cellulase secretion reduced the matrix's stiffness. Optogenetic circuits were also integrated into the material, transforming the LMs into a living biosensor capable of detecting blue light and expressing fluorescent reporter proteins.

Biomineralization is a common strategy used to enhance mechanical properties. In one example, *Sporosarcina pasteurii* was encapsulated in gelatin microparticles embedded in a Ca^{2+}-crosslinked alginate hydrogel. When exposed to a mineralizing environment, the encapsulated bacteria hydrolyzed urea, producing carbonate ions that reacted with calcium ions to precipitate $CaCO_3$ minerals (**Figure 1-2A**). The hardening of the composite enabled it to withstand pressures of up to 3.5 MPa.[23] Integrating a synthetic polymer matrix can provide additional avenues for reconfiguring material properties. Yu et al. incorporated chloroplasts into a synthetic hydrogel containing a glucose-crosslinkable isocyanate group.[24] The photosynthesized glucose facilitated crosslinking of the hydrogel, enhancing its Young's modulus in response to light.

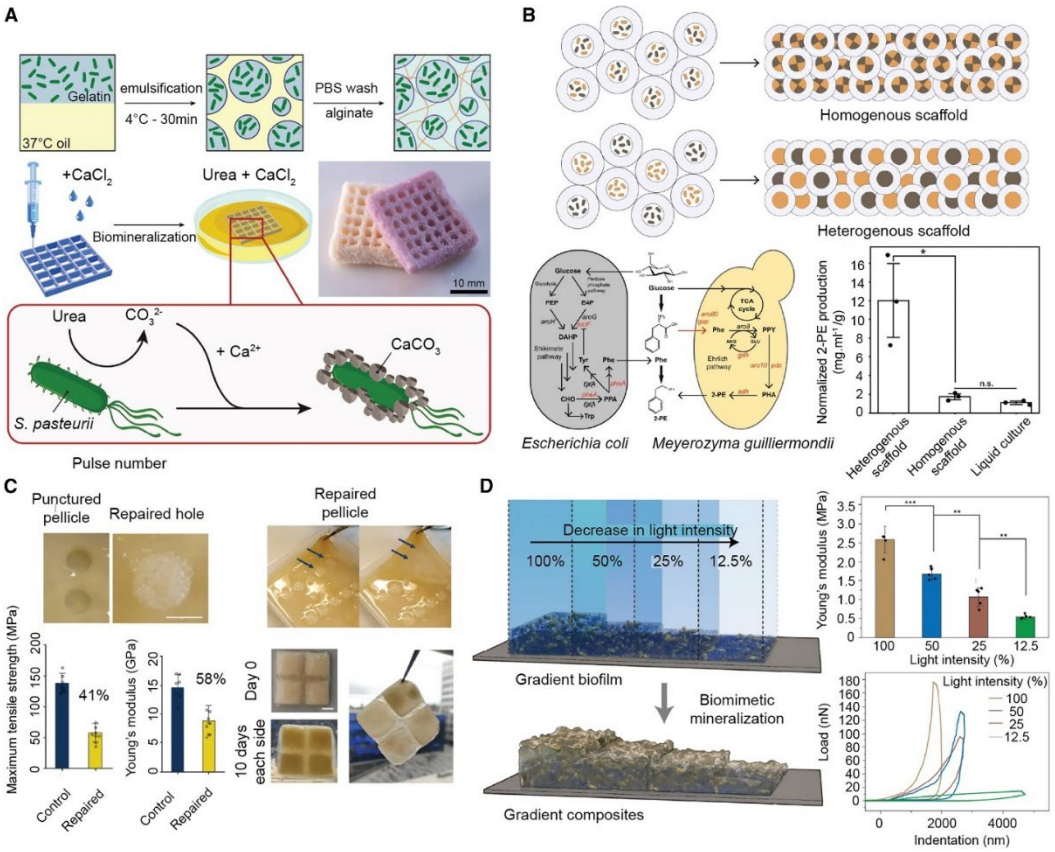

Figure 1-2. Strategies to imitate living features in LMs. A. *S. pasteurii*-driven biomineralization modifies the mechanical properties of a gelatin-alginate matrix in the presence of urea. Reproduced with permission from Hirsch et al., copyright 2023, Elsevier.[23] **B.** Compartmentalization of *E. coli* and *M. guilliermondii* into a heterogeneous core-shell microparticle scaffold enables efficient conversion of glucose into 2-PE through the cooperative action of the two organisms. Reproduced with permission from Ou et al., copyright 2023, Springer Nature.[25] **C.** Bacterial cellulose spheroids used as self-growing building blocks can heal punctured holes and glue fragmented synthetic material, allowing the recovery of tensile strength and Young's modulus. Scale bar, 5mm. Reproduced with permission from Caro-Astorga et al., copyright 2021, Springer Nature.[26] **D.** Light-inducible biofilm growth and biomineralization produce a gradient of biofilm height and Young's modulus at different light intensities. Reproduced with permission from Wang et al., copyright 2020, Springer Nature.[27]

1.3.2. Compartmentalization

LMs mimic compartmentalized interactions in nature by organizing microbes with distinct functionalities into modular building blocks. Achieved through 3D printing, separating different engineered cell types in hydrogel matrices can facilitate bio-computing. For example, multicellular logic has been achieved through compartmentalization, where operations such as NOT, AND, OR, and NAND are performed based on the spatial distribution and interactions of genetically engineered *E. coli*.[28] Also, separating bacterial strains with sender and receiver functions into different building blocks simplifies biosensing processes.[29]

The concept of division of labor can facilitate bioprocessing in LMs. Ou et al. compartmentalized engineered *E. coli* and *Meyerozyma guilliermondii* within microparticles consisting of a carboxymethylcellulose core and a gelatin/gelatin methacryloyl shell, crosslinked to create a heterogeneous scaffold.[25] Enzymatic cascades and interparticle metabolite transfer enabled the conversion of glucose to 2-phenylethanol (2-PE) through cooperative action of the two organisms (**Figure 1-2B**). Compartmentalization prevented competitive growth and promoted efficient mass transfer of metabolites, resulting in a 6-fold increase in 2-PE production compared to homogeneous counterparts.

1.3.3. Self-healing and regeneration

LMs emulate nature's ability for autonomous growth and regeneration by incorporating matrix-forming microorganisms. Bacterial cellulose, known for its high tensile strength, flexibility, biocompatibility, and degradability, is widely used as a self-growing matrix. Caro-Astorga et al. utilized millimeter-scale bacteriocellulose spheroids grown from shaking cultures of K. rhaeticus as modular building blocks to create 3D-shaped living materials.[26] These spheroid particles effectively sealed punctures in the bacterial cellulose pellicle, restoring its Young's modulus and even fusing fragmented synthetic materials together within 10 days (**Figure 1-2C**). Other than bacteriocellulose, biofilms can be used for self-regenerating material. In one example, Wang et al. developed living patterned and gradient composites

by combining light-inducible bacterial biofilm growth with biomimetic hydroxyapatite mineralization.26 The thickness of the biofilm was precisely controlled using blue light intensity, resulting in a gradient of Young's modulus (**Figure 1-2D**).

1.4. The convergence of bioelectronics and living materials

In summary, we explored how two distinct disciplines—bioelectronics and LMs—aim to replicate nature's living properties using innovative approaches. Bioelectronics primarily focuses on material engineering, while LMs emphasize genetic modification and the selection of functional microbes. For instance, bioelectronics achieve self-healing capabilities through dynamic bond-forming materials, whereas LMs usually attain regenerative properties by engineered organisms that secrete extracellular matrix. Bioelectronics achieve stimuli responsiveness by harnessing chemical and physical properties of synthetic materials, while LMs accomplish these traits via compartmentalizing microorganisms with genetically encoded logic gates. Despite their differing methodologies, their goal is harmonious. Recently, there has been an emerging effort to integrate bioelectronics and LMs to create living bioelectronics, which synergistically realize nature's dynamic living properties for disease treatments.

LMs with high electronic conductivity have replaced gold films as self-healing and stretchable interconnects. For example, Chen et al. developed engineered bacteria that self-assembles through nanobody (Nb)-antigen (Ag) pair adhesion (**Figure 1-3A and Figure 1-3B**).[30] This material, known as living assembled material by bacterial adhesion (LAMBA), was conductive and capable of rapid self-healing through cell growth and adhesion. When used as an electromyography sensor, sliced LAMBA maintained conductivity through multiple stretch cycles after healing, effectively addressing the fatigue issue in wearable devices. Additionally, LAMBA's conductivity could be enhanced by programming the expression of a protein that immobilizes AuNPs. This example shows that LMs with programmable electrical properties, fatigue resistance, and self-regeneration can enable the development of adaptable electronics that respond to environmental changes.

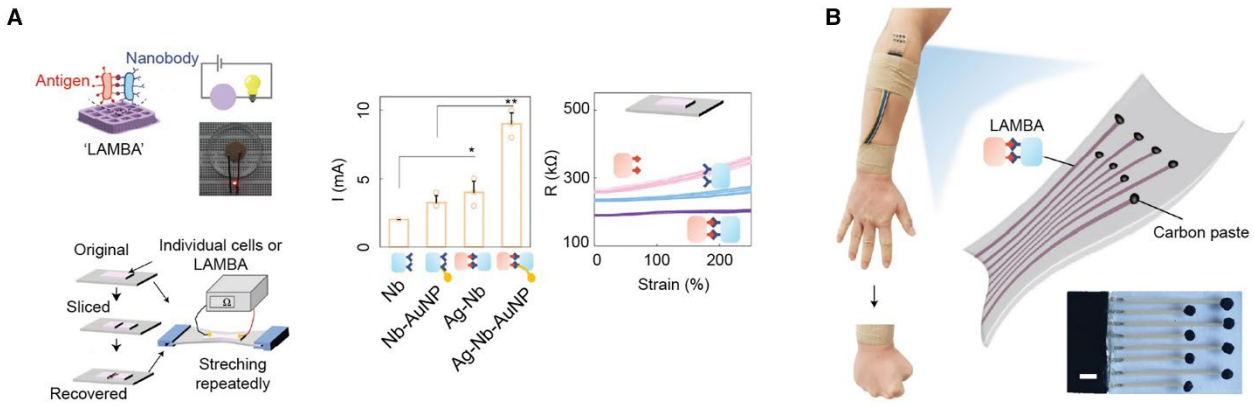

Figure 1-3. Emerging prospects in living bioelectronics. A. Conjugating *E. coli* that expresses Ag and Nb pair forms a LAMBA with programmable conductivity and the ability to recover damage induced by slicing and repeated stretching. **B.** LAMBA can be electronically integrated as a self-healing conductor in an electromyography sensor. Scale bar, 2mm. Reproduced with permission from Chen et al., copyright 2021, Springer Nature.[30]

LMs in bioelectronics can serve as a transducer for complex biological signals. For instance, Mimee and colleagues developed a hemoglobin-sensitive probiotic biosensor that expresses a luminescence reporter when exposed to gastrointestinal bleeding (**Figure 1-4A**).[31] This signal is then quantified by a photodetector, which wirelessly transmits photocurrent data for real-time monitoring in vivo. In a recent study, Atkinson et al. electrogenetically engineered *E. coli* to produce an electrical current in response to an endocrine disruptor (**Figure 1-4B**).[32] When encapsulated with conductive nanomaterials, the engineered *E. coli* detected the endocrine disruptor in urban water samples within minutes. These examples show how the integrated LMs can transduce complex biological signals into an output that can be precisely quantified by bioelectronics.

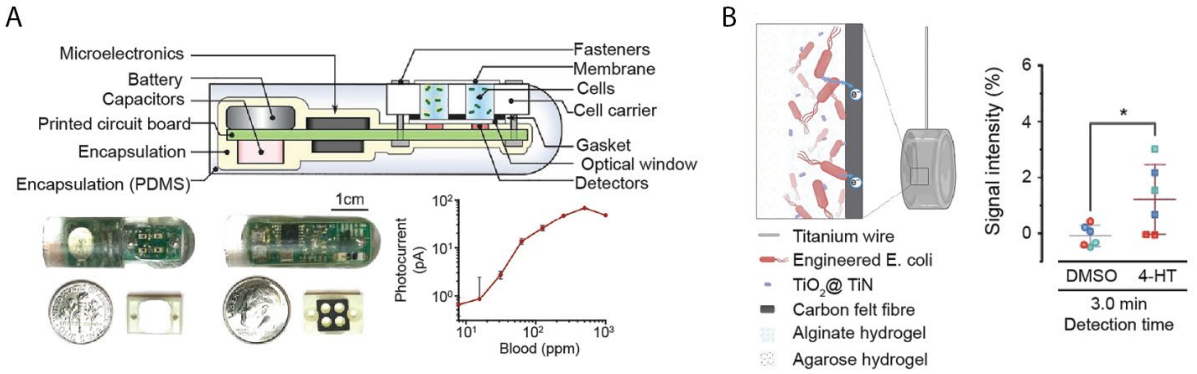

Figure 1-4. Emerging prospects in living bioelectronic sensors. A. Engineered *E. coli* produces luminescence in response to blood heme. When integrated with an ingestible microelectronic pill, equipped with photodetectors, the luminescence signal can be quantified as photocurrent and wirelessly transmitted for real-time monitoring of porcine gastric bleeding. Reproduced with permission from Mimee et al., copyright 2018, AAAS.[31] **B.** Electrogenetically engineered *E. coli* encapsulated in a conductive hydrogel scaffold enables fast detection of the endocrine disruptor 4-hydroxytamoxifen (4-HT) in urban water samples through EET. Reproduced with permission from Atkinson et al., copyright 2022, Springer Nature.[32]

1.5 Current Status of living bioelectronic interfaces

Living materials have been interfaced with bioelectronics as self-healing conductive interconnects and biosensing transducers. However, integration beyond these functions remains limited. In **Part 2**, we explore integration of LMs as a bioactive interface in electronic devices, revealing unique synergies that enable effective immunomodulation. In **Part 3**, we investigate how bioelectronics and LMs can interact by probing microbial response at the electrified interface, demonstrating how we can leverage the bioelectronics-LMs interaction for infection management (**Figure 1-5**).

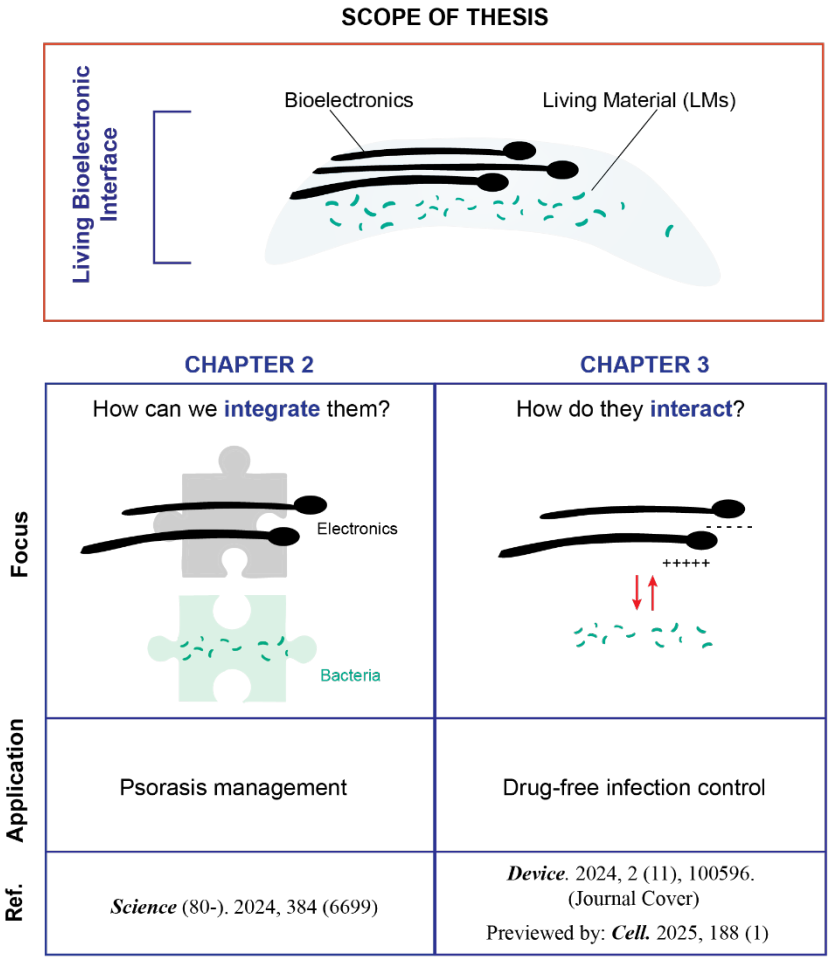

Figure 1-5. Outline of the topics to be discussed in chapter 2 and chapter 3.

1.5. Bibliography

(1) Kim, S.; Eig, E.; Tian, B. The Convergence of Bioelectronics and Engineered Living Materials. *Cell Reports Phys. Sci.* **2024**, *5*, 102149. https://doiW.org/10.1016/j.xcrp.2024.102149.

(2) Prominski, A.; Li, P.; Miao, B. A.; Tian, B. Nanoenabled Bioelectrical Modulation. *Accounts Mater. Res.* **2021**, *2* (10), 895–906. https://doi.org/10.1021/accountsmr.1c00132.

(3) Mostafalu, P.; Tamayol, A.; Rahimi, R.; Ochoa, M.; Khalilpour, A.; Kiaee, G.; Yazdi, I. K.; Bagherifard, S.; Dokmeci, M. R.; Ziaie, B.; Sonkusale, S. R.; Khademhosseini, A. Smart Bandage for Monitoring and Treatment of Chronic Wounds. *Small* **2018**, *14* (33), 1–9. https://doi.org/10.1002/smll.201703509.

(4) Li, P.; Kim, S.; Tian, B. Nanoenabled Trainable Systems: From Biointerfaces to Biomimetics. *ACS Nano* **2022**, *16* (12), 19651–19664. https://doi.org/10.1021/acsnano.2c08042.

(5) Sun, C.; Cheng, Z.; Abu-Halimah, J.; Tian, B. Perspectives on Tissue-like Bioelectronics for Neural Modulation. *iScience* **2023**, *26* (5), 106715. https://doi.org/10.1016/j.isci.2023.106715.

(6) Fang, Y.; Yang, X.; Lin, Y.; Shi, J.; Prominski, A.; Clayton, C.; Ostroff, E.; Tian, B. Dissecting Biological and Synthetic Soft-Hard Interfaces for Tissue-Like Systems. *Chem. Rev.* **2022**, *122* (5), 5233–5276. https://doi.org/10.1021/acs.chemrev.1c00365.

(7) Van De Burgt, Y.; Lubberman, E.; Fuller, E. J.; Keene, S. T.; Faria, G. C.; Agarwal, S.; Marinella, M. J.; Alec Talin, A.; Salleo, A. A Non-Volatile Organic Electrochemical Device as a Low-Voltage Artificial Synapse for Neuromorphic Computing. *Nat. Mater.* **2017**, *16* (4), 414–418. https://doi.org/10.1038/NMAT4856.

(8) Rodrigo-Navarro, A.; Sankaran, S.; Dalby, M. J.; del Campo, A.; Salmeron-Sanchez, M. Engineered Living Biomaterials. *Nat. Rev. Mater.* **2021**, *6* (12), 1175–1190. https://doi.org/10.1038/s41578-021-00350-8.

(9) Praveschotinunt, P.; Duraj-Thatte, A. M.; Gelfat, I.; Bahl, F.; Chou, D. B.; Joshi, N. S. Engineered E. Coli Nissle 1917 for the Delivery of Matrix-Tethered Therapeutic Domains to the Gut. *Nat. Commun.* **2019**, *10* (1). https://doi.org/10.1038/s41467-019-13336-6.

(10) Jiang, Y.; Ji, S.; Sun, J.; Huang, J.; Li, Y.; Zou, G.; Salim, T.; Wang, C.; Li, W.; Jin, H.; Xu, J.; Wang, S.; Lei, T.; Yan, X.; Peh, W. Y. X.; Yen, S. C.; Liu, Z.; Yu, M.; Zhao, H.; Lu, Z.; Li, G.; Gao, H.; Liu, Z.; Bao, Z.; Chen, X. A Universal Interface for Plug-and-Play Assembly of Stretchable Devices. *Nature* **2023**, *614* (7948), 456–462. https://doi.org/10.1038/s41586-022-05579-z.

(11) Li, P.; Kim, S.; Tian, B. Beyond 25 Years of Biomedical Innovation in Nano-Bioelectronics. *Device* **2024**, *2*, 100401. https://doi.org/10.1016/j.device.2024.100401.

(12) Cooper, C. B.; Root, S. E.; Michalek, L.; Wu, S.; Lai, J.-C.; Khatib, M.; Oyakhire, S. T.; Zhao, R.; Qin, J.; Bao, Z. Autonomous Alignment and Healing in Multilayer Soft Electronics Using Immiscible Dynamic Polymers. *Science (80-.).* **2023**, *380* (6648), 935–941. https://doi.org/10.1126/science.adh0619.

(13) Ge, G.; Lu, Y.; Qu, X.; Zhao, W.; Ren, Y.; Wang, W.; Wang, Q.; Huang, W.; Dong, X. Muscle-Inspired Self-Healing Hydrogels for Strain and Temperature Sensor. *ACS Nano* **2020**, *14* (1), 218–228. https://doi.org/10.1021/acsnano.9b07874.

(14) Oh, J. Y.; Son, D.; Katsumata, T.; Lee, Y.; Kim, Y.; Lopez, J.; Wu, H.-C.; Kang, J.; Park, J.; Gu, X.; Mun, J.; Wang, N. G.-J.; Yin, Y.; Cai, W.; Yun, Y.; Tok, J. B.-H.; Bao, Z. Stretchable Self-Healable Semiconducting Polymer Film for Active-Matrix Strain-Sensing Array. *Sci. Adv* **2019**, *5* (11). https://doi.org/10.1126/sciadv.aav3097.

(15) Shi, J.; Lin, Y.; Li, P.; Mickel, P.; Sun, C.; Parekh, K.; Ma, J.; Kim, S.; Ashwood, B.; Meng, L.; Luo, Y.; Chen, S.; Tsai, H.-M.; Cham, C. M.; Zhang, J.; Cheng, Z.; Abu-Halimah, J. A.; Chen, J.; Griffin, P.; Chang, E. B.; Král, P.; Yue, J.; Tian, B. Monolithic-to-Focal Evolving Biointerfaces in Tissue Regeneration and Bioelectronics. *Nat. Chem. Eng.* **2024**, *1* (1), 73–86. https://doi.org/10.1038/s44286-023-00008-y.

(16) Fu, T.; Liu, X.; Gao, H.; Ward, J. E.; Liu, X.; Yin, B.; Wang, Z.; Zhuo, Y.; Walker, D. J. F.; Yang, J. J.; Chen, J.; Lovley, D. R.; Yao, J. Bioinspired Bio-Voltage Memristors. *Nat. Commun.* **2020**, *11* (1). https://doi.org/10.1038/s41467-020-15759-y.

(17) Jiao, Y.; Zhang, Y.; Feng, H.; Li, H.; Wang, Z.; Wang, P.; Wang, Y.; Zheng, N.; Xie, T.; Ma, Y.; Feng, X. A Multifunctional Bioelectronic Device with Switchable Rigidity and Reconfigurable Shapes for Comprehensive Diagnosis. *Adv. Electron. Mater.* **2023**, *9* (7), 2201343. https://doi.org/10.1002/aelm.202201343.

(18) Han, M.; Wang, H.; Yang, Y.; Liang, C.; Bai, W.; Yan, Z.; Li, H.; Xue, Y.; Wang, X.; Akar, B.; Zhao, H.; Luan, H.; Lim, J.; Kandela, I.; Ameer, G. A.; Zhang, Y.; Huang, Y.; Rogers, J. A. Three-Dimensional Piezoelectric Polymer Microsystems for Vibrational Energy Harvesting, Robotic Interfaces and Biomedical Implants. *Nat. Electron.* **2019**, *2* (1), 26–35. https://doi.org/10.1038/s41928-018-0189-7.

(19) Ren, W.; Sun, Y.; Zhao, D.; Aili, A.; Zhang, S.; Shi, C.; Zhang, J.; Geng, H.; Zhang, J.; Zhang, L.; Xiao, J.; Yang, R. High-Performance Wearable Thermoelectric Generator with Self-Healing, Recycling, and Lego-like Reconfiguring Capabilities. *Sci. Adv* **2021**, *7* (7). https://doi.org/10.1126/sciadv.abe0586.

(20) Bhatnagar, P.; Patel, M.; Nguyen, T. T.; Kim, S.; Kim, J. Transparent Photovoltaics for Self-Powered Bioelectronics and Neuromorphic Applications. *J. Phys. Chem. Lett.* **2021**, *12* (51), 12426–12436. https://doi.org/10.1021/acs.jpclett.1c03514.

(21) Lipomi, D. J.; Vosgueritchian, M.; Tee, B. C. K.; Hellstrom, S. L.; Lee, J. A.; Fox, C. H.; Bao, Z. Skin-like Pressure and Strain Sensors Based on Transparent Elastic Films of Carbon Nanotubes. *Nat. Nanotechnol.* **2011**, *6* (12), 788–792. https://doi.org/10.1038/nnano.2011.184.

(22) Gilbert, C.; Tang, T. C.; Ott, W.; Dorr, B. A.; Shaw, W. M.; Sun, G. L.; Lu, T. K.; Ellis, T. Living Materials with Programmable Functionalities Grown from Engineered Microbial Co-Cultures. *Nat. Mater.* **2021**, *20* (5), 691–700. https://doi.org/10.1038/s41563-020-00857-5.

(23) Hirsch, M.; Lucherini, L.; Zhao, R.; Clarà Saracho, A.; Amstad, E. 3D Printing of Living Structural Biocomposites. *Mater. Today* **2023**, *62* (February), 21–32. https://doi.org/10.1016/j.mattod.2023.02.001.

(24) Yu, K.; Feng, Z.; Du, H.; Xin, A.; Hoon, K.; Li, K.; Su, Y.; Wang, Q. Photosynthesis-Assisted Remodeling of Three-Dimensional Printed Structures. *PNAS* **2021**, *118* (3), 1–9. https://doi.org/10.1073/pnas.2016524118.

(25) Ou, Y.; Cao, S.; Zhang, Y.; Zhu, H.; Guo, C.; Yan, W.; Xin, F.; Dong, W.; Zhang, Y.; Narita, M.; Yu, Z.; Knowles, T. P. J. Bioprinting Microporous Functional Living Materials from Protein-Based Core-Shell Microgels. *Nat. Commun.* **2023**, *14* (1). https://doi.org/10.1038/s41467-022-35140-5.

(26) Caro-Astorga, J.; Walker, K. T.; Herrera, N.; Lee, K. Y.; Ellis, T. Bacterial Cellulose Spheroids as Building Blocks for 3D and Patterned Living Materials and for Regeneration. *Nat. Commun.* **2021**, *12* (1), 1–9. https://doi.org/10.1038/s41467-021-25350-8.

(27) Wang, Y.; An, B.; Xue, B.; Pu, J.; Zhang, X.; Huang, Y.; Yu, Y.; Cao, Y.; Zhong, C. Living Materials Fabricated via Gradient Mineralization of Light-Inducible Biofilms. *Nat. Chem. Biol.* **2021**, *17* (3), 351–359. https://doi.org/10.1038/s41589-020-00697-z.

(28) Liu, X.; Yuk, H.; Lin, S.; Parada, G. A.; Tang, T. C.; Tham, E.; de la Fuente-Nunez, C.; Lu, T. K.; Zhao, X. 3D Printing of Living Responsive Materials and Devices. *Adv. Mater.* **2018**, *30* (4), 1–9. https://doi.org/10.1002/adma.201704821.

(29) Tang, T. C.; Tham, E.; Liu, X.; Yehl, K.; Rovner, A. J.; Yuk, H.; de la Fuente-Nunez, C.; Isaacs, F. J.; Zhao, X.; Lu, T. K. Hydrogel-Based Biocontainment of Bacteria for Continuous Sensing and Computation. *Nat. Chem. Biol.* **2021**, *17* (6), 724–731. https://doi.org/10.1038/s41589-021-00779-6.

(30) Chen, B.; Kang, W.; Sun, J.; Zhu, R.; Yu, Y.; Xia, A.; Yu, M.; Wang, M.; Han, J.; Chen, Y.; Teng, L.; Tian, Q.; Yu, Y.; Li, G.; You, L.; Liu, Z.; Dai, Z. Programmable Living Assembly of Materials

by Bacterial Adhesion. *Nat. Chem. Biol.* **2022**, *18* (3), 289–294. https://doi.org/10.1038/s41589-021-00934-z.

(31) Mimee, M.; Nadeau, P.; Hayward, A.; Carim, S.; Flanagan, S.; Jerger, L.; Collins, J.; Mcdonnell, S.; Swartwout, R.; Citorik, R. J.; Bulovi, V.; Langer, R.; Traverso, G.; Chandrakasan, A. P.; Lu, T. K. An Ingestible Bacterial-Electronic System to Monitor Gastrointestinal Health. *Science (80-.).* **2018**, *360* (6391), 915–918. https://doi.org/10.1126/science.aas9315.

(32) Atkinson, J. T.; Su, L.; Zhang, X.; Bennett, G. N.; Silberg, J. J.; Ajo-Franklin, C. M. Real-Time Bioelectronic Sensing of Environmental Contaminants. *Nature* **2022**, *611* (7936), 548–553. https://doi.org/10.1038/s41586-022-05356-y.

Chapter 2. Active Biointegrated Living Electronics (ABLE) for Inflammation Management

*Chapter 2 adopts figures and text from ref (1): Shi, J.†; **Kim, S.†;** Li, P.; Dong, F.; Yang, C.; Nam, B.; Han, C.; Eig, E.; Shi, L. L.; Niu, S.; Yue, J.; Tian, B. Active Biointegrated Living Electronics for Managing Inflammation. *Science (80-.).* **2024**, *384* (6699), 1023–1030. Adapted with permission from Shi et al., copyright 2024, AAAS.

2.1 Introduction

2.1.1 Biointerface for inflammation management

Biomaterials that synergistically incorporate biomechanical,[2–4] biogenic,[5–7] and bioelectrical[8–10] properties offer the potential to establish lifelike, seamless, and multifaceted biointerfaces with tissues. Bioelectronics, in particular, have become indispensable for capturing physiological signals,[11–14] monitoring inflammation as a diagnostic tool,[15,16] and executing biological modulation for targeted treatments.[17,18] However, the primary challenge with traditional bioelectronics is their integration with biological tissues, which arises from disparities in mechanical, chemical, and biological attributes (**Figure 2-1A and Figure 2-1B**.[19,20] The mechanical discrepancies in bioelectronics can lead to interfacial discontinuities, compromising signal fidelity.[21,22] Although hydrogels act as an intermediary layer to bridge the mechanical gap between electronics and biological systems, they may fall short in providing the necessary cellular functions for tissue modulation (**Figure 2-1C**).[23,24] Consequently, contemporary bioelectronics, when used to monitor inflammatory conditions, lack the biogenic capacity for concurrent immunoregulation.[15] This limitation restricts the versatility of bioelectronics in addressing the complexities of various diseases. To expand the role of bioelectronics in tissue restoration and monitoring, there is a pressing need to design interface with enhanced bioactivity. Inherent biological systems such as bacteria and mammalian cells naturally exhibit cellular signal generation and transmission, which may be leveraged for inflammation management.[25] However, the integration of these living entities into bioelectronics remains a challenge, mainly due to the absence of precise control mechanisms and a thorough understanding of the dynamics between foreign cells and host diseases.

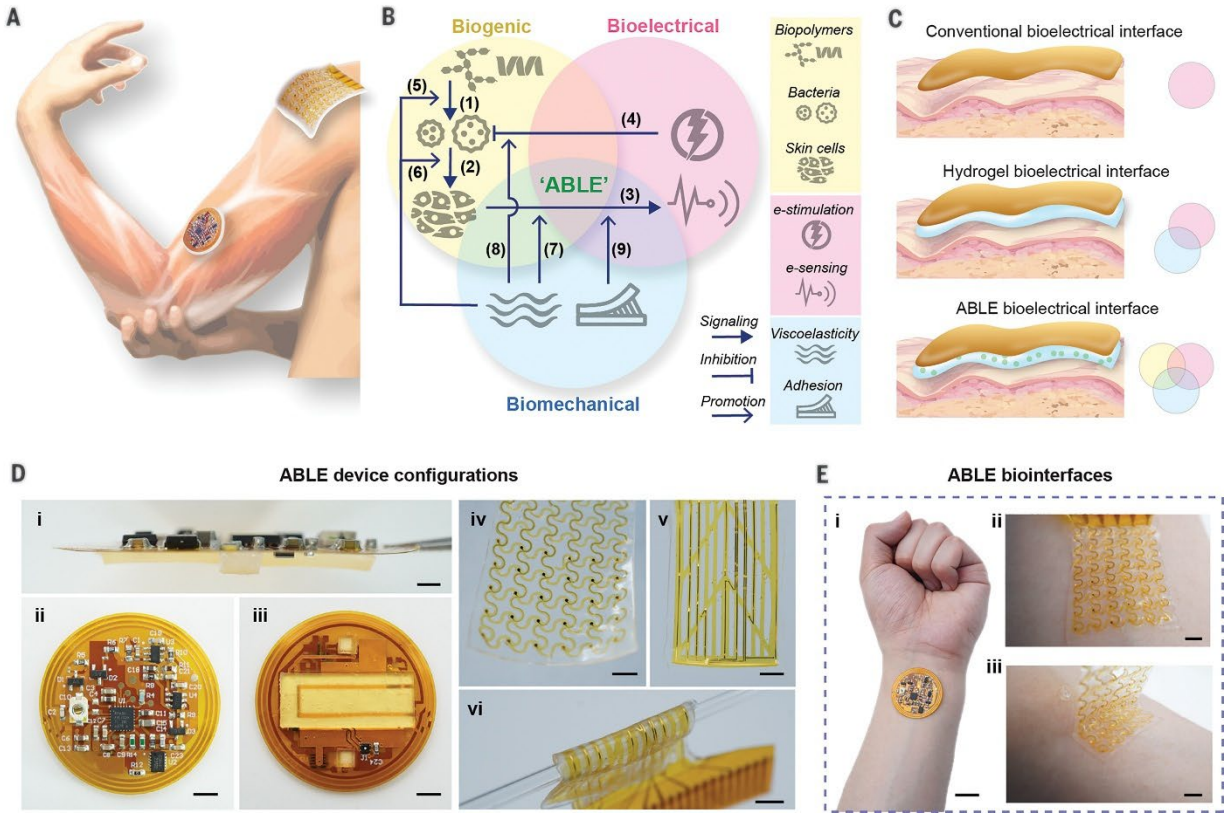

Figure 2-1. Living bioelectronics device with bioactive interface enables wireless skin disease diagnosis and therapy. A. Schematic illustrates that living bioelectronics enable information collection, disease diagnosis, and therapy delivery. **B**. The interplay across the three key dimensions through bioelectronics, hydrogel, and bacteria is crucial for biointegrated living electronics functionality. (1) Biopolymer enhances bacterial viability. (2) Bacteria modulate the skin immune environment. (3) Bioelectronics collects information from skin through electrical sensing (e-sensing). (4) Bioelectronics manages the biosafety of bacteria through electrical stimulation (e-stimulation). (5) Hydrogel encapsulation promotes long-term storage and viability of bacteria. (6) Viscoelasticity of the living hydrogel ensures a stable interaction with skin tissue. (7) Viscoelasticity of the hydrogel facilitates information collection from skin. (8) Biomechanical properties of the hydrogel assist biohazard management. (9) Skin-adhesion property of the hydrogel improves long-term information collection. **C**. Compared to conventional bioelectronics interfaces, ABLE combines functionalities across the bioelectrical, biomechanical, and biogenic domains. **D.** Photographs display the various ABLE device configurations. Scale bars: (i) 2 mm;

(ii), (iii) 4 mm; (iv), (v), (vi) 3 mm. **E**. Photographs show the ABLE bioelectrical interfaces. Scale bars: (i) 15 mm; (ii) 3 mm; (iii) 5 mm.

2.1.2 Design principle of ABLE

We introduce the active biointegrated living electronics (ABLE) platform (**Figure 2-1-D and Figure 2-1E**). The ABLE platform comprises a living hydrogel at the tissue-electronics interface to impart essential biogenic properties for skin immunoregulation. The skin commensal bacterium *Staphylococcus epidermidis* from human skin flora was chosen as the living component in biointerfaces, which provides bioelectronics with capabilities to regulate inflammation and promote skin regeneration. The ABLE platform multifunctionality arises from synergistic interaction between the biogenic, biomechanical, and bioelectrical realms (**Figure 2-1B**). Biogenic polymers enhance bacterial viability (**Figure 2-1B**, item 1), and the bacteria themselves modulate the skin's immune environment (**Figure 2-1B**, item 2). The bioelectronics within the system facilitate electrical sensing (e-sensing) to gather information from the skin (**Figure 2-1B,** item 3) and utilize electrical stimulation (e-stimulation) to manage the biosafety of bacteria (**Figure 2-1B**, item 4), addressing long-standing biohazard concerns of handling synthetic living materials with opportunistic pathogens.[26,27] The living hydrogel plays multiple roles: Its encapsulation fosters prolonged bacterial storage and viability (**Figure 2-1B**, item 5), and its viscoelastic properties ensure stable skin interaction (**Figure 2-1B**, item 6), aid in information collection from the skin (**Figure 2-1B**, item 7), and assist in biohazard management (**Figure 2-1B**, item 8). Lastly, the hydrogel's skin-adhesion property facilitates long-term data acquisition (**Figure 2-1B**, item 9).

2.2 Results and Discussion

2.2.1 Design and evaluation of the biogenic matrix in ABLE

We chose a hydrogel composite as the primary matrix for the living ABLE biointerface owing to its biomechanical and structural resemblance to biological tissues.[20] We incorporated *S. epidermidis* as the living component, because this species is part of the human skin flora and can modulate biological activity

in skin cells.[28] To ensure the functionality of the living biointerface, the hydrogel matrix must support bacterial viability, with bioelectrical and biomechanical capabilities for interfacing with electronics and biological tissue.

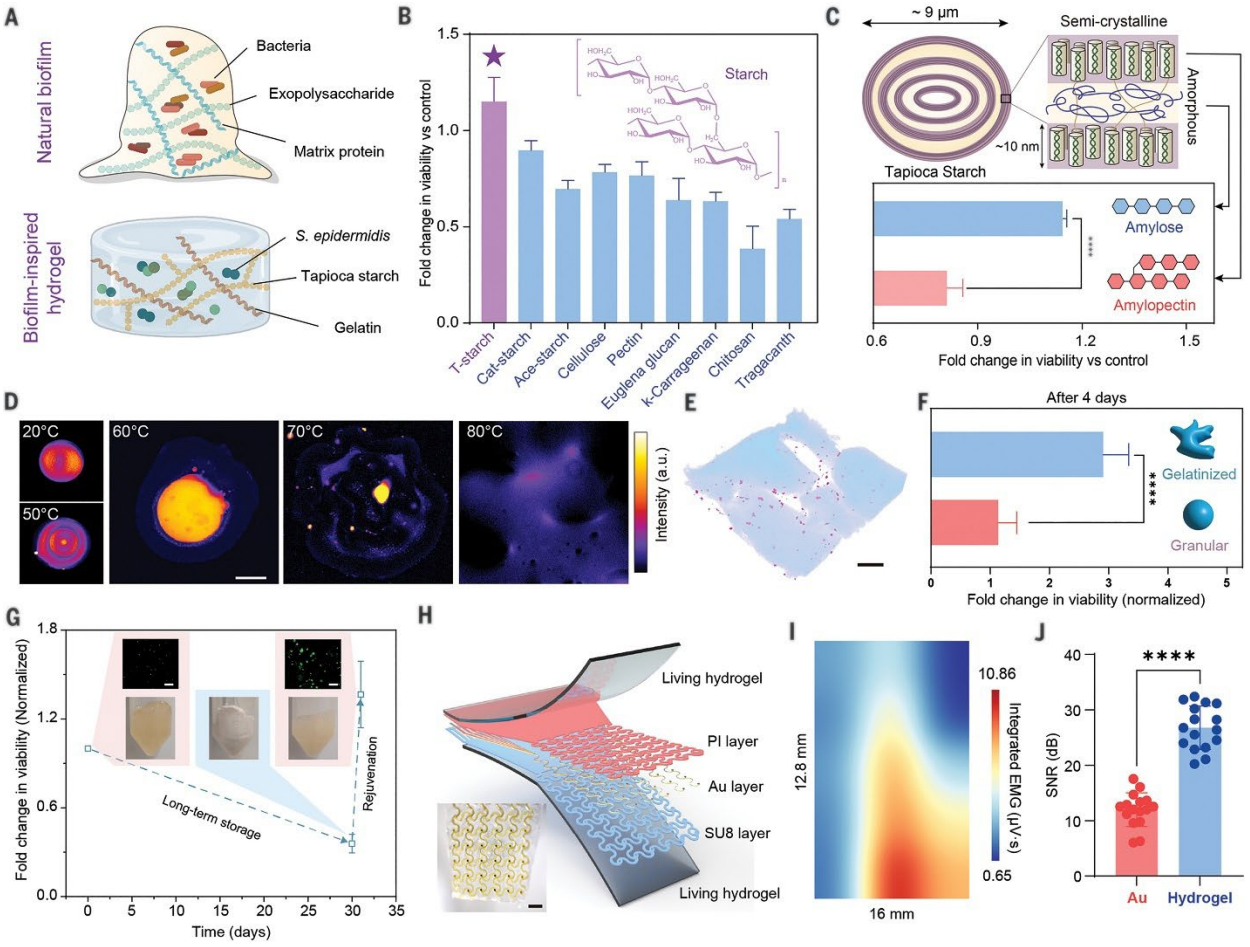

Fig. 2-2. Rational design of living biointerface for bioelectronics with biogenic, biomechanical, and bioelectrical functionality. A. Mimicking the natural composition of biofilm, gelatin and starch are used as the protein and polysaccharide polymer in constructing the double network hydrogel, i.e., the living biointerface. **B**. Tapioca starch best sustains bacteria viability among various polysaccharides. $n = 5$ independent experiments. **C**. During gelatinization, amylose leaks from the amorphous lamella inside the starch granules and enhances bacteria viability. $n = 5$ independent experiments. **D**. Fluorescent images indicate the structural transformation of starch granules after thermal treatment at different temperatures. Scale bar, 10 μm. **E.** Confocal microscope imaging shows the distribution of *S. epidermidis* inside the living

hydrogel matrix. Bacteria are stained with FM1-43 (red) and starch is stained with 8-amino-1,3,6-pyrenetrisulfonic acid (blue). Scale bar, 15 μm. **F.** Gelatinization of starch promotes bacteria viability in the living hydrogel matrix for at least 4 days. $n = 5$ independent experiments. **G**. Bacteria can be stored within the hydrogel matrix over a long-term period and rejuvenated with an overnight culture. Scale bar, 20 μm. $n = 5$ independent experiments. **H**. Schematic diagram and photograph show the structural configuration of the living hydrogel hybrid mesh electronics device for sEMG recording. Scale bar, 3 mm. **I**. Spatial intensity map reveals the sEMG activity across the 15 electrical channels at the rat leg. Size of region: 16 mm (horizontal) by 12.8 mm (vertical). **J**. Comparison of SNR in gold bioelectronics biointerface versus living hydrogel coating indicated that living hydrogel-coated bioelectronics facilitate electrophysiological recording. $n = 15$ independent channels. *P* values are determined by paired *t* test, two tailed. All data are presented as mean values ± SD.

In designing a hydrogel matrix conducive to the long-term viability of *S. epidermidis* (**Figure 2-1B,** item 1), we drew inspiration from natural biofilms that promote bacterial survival and community regulation.[29] To emulate the major biofilm components of proteinaceous matrix and exopolysaccharides, we created a biocompatible hydrogel matrix using a dual network of protein and polysaccharide polymers (Figure 2.2-A). We selected gelatin as the main protein matrix given its natural origin and superior hydrogel-forming properties.[30] To identify the polysaccharide component, we screened a library of materials including various biogenic and synthetic polymers. Tapioca starch best supported *S. epidermidis* viability and was selected as the polysaccharide (**Figure 2-2B and Figure 2-2C**). We further applied a gelatinization and retrogradation process through a heating-cooling cycle. This process diminished the crystallinity of the starch, altering the granular morphology and diffusing out the granule-enclosed amylose (**Figure 2-2D**). The hydrated starch with exposed amylose content formed a biocompatible network with which bacteria interact (**Figure 2-2C-E**). Gelatinization of starch prolongs bacterial viability inside hydrogel matrix (**Figure 2.2-F**). Altogether, we crafted a protein-polysaccharide hydrogel for bacterial encapsulation and immobilization (**Figure 2-2E and Figure 2-3**), which promoted prolonged bacterial viability of at least 4

days (**Figure 2-2F**). Additionally, the freeze-dried living hydrogel can be preserved for 30 days at −80°C. Owing to the hydrogel's ability to support bacterial growth, any loss of bacterial viability during storage can be recovered beyond its initial level by allowing the rehydrated hydrogel to sit at room temperature overnight. This feature, along with the stability of electronic devices, indicates potential for industrialization and distribution (**Figure 2-2G**).

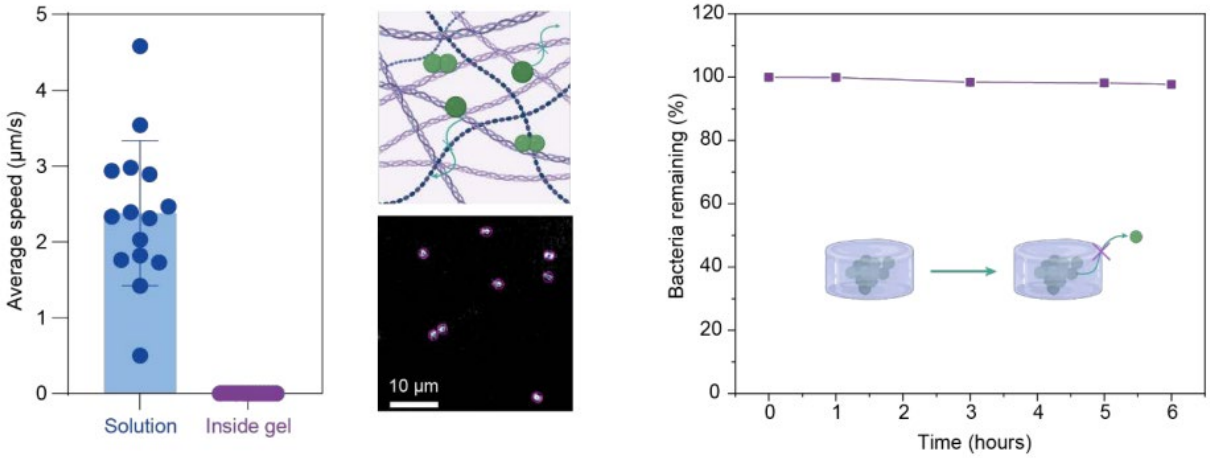

Figure 2-3. Hydrogel immobilizes the motion of encapsulated bacteria. Bacteria display significantly reduced motion speed within the hydrogel matrix compared to the culture medium, suggesting that the living hydrogel effectively restricts the movement of bacteria within the matrix. Scale bar, 10 μm. Data are presented as mean ± standard error of mean. (n=3)

The living hydrogels display favorable bioelectrical and biomechanical characteristics, facilitating integration of bioelectronic devices with biological tissues (**Figure 2-1B**). The living hydrogels have a high water content (>75%), possess tissue-compliant ultrasoftness (shear modulus of 4 kPa), and remain stable across environmental variations (**Figure 2-4**). The strain- and frequency-dependent modulus, fast stress relaxation, and mechanical hysteresis further confirmed the viscoelasticity (**Figure 2-4**). Such tissue-mimicking biomechanical properties promote a conformal biointerface with tissues, for seamless integration of bioelectronics (**Figure 2-5**). Furthermore, the abundance of hydroxyl groups in the starch polymer endows the living hydrogel with adhesive properties, enhancing the stability of the bioelectronic devices on the tissue.

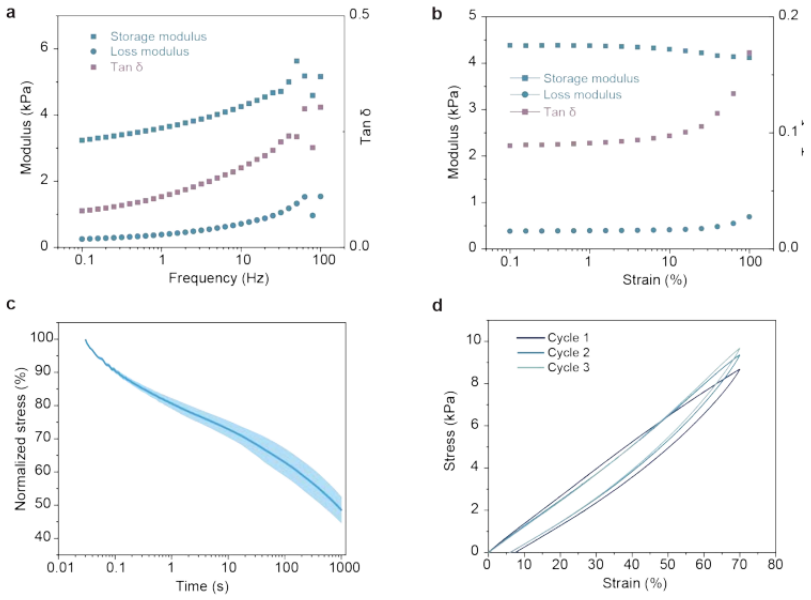

Figure. 2-4. Mechanical tests demonstrate the living hydrogel is soft and viscoelastic. (a) Storage modulus (G'; left axis), Loss modulus (G''; left axis), and tan δ (G''/G'; right axis) are shown as a function of frequency at 1% of strain. (b) Storage modulus (G'; left axis), Loss modulus (G''; left axis), and tan δ (G''/G'; right axis) are shown as a function of strain at 1Hz frequency. (c) The stress relaxation test shows the living hydrogel has fast relaxation behaviors. (d) The strain-stress curve illustrates that the living hydrogel undergoes energy dissipation during the cyclic mechanical loading. n=5 for each test.

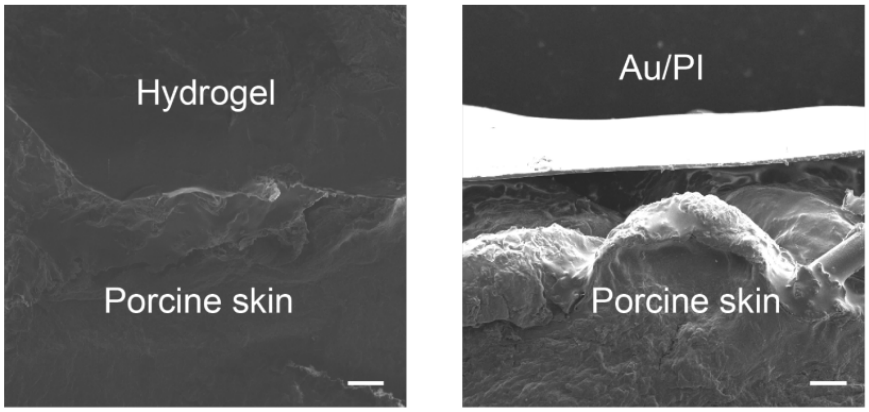

Figure 2-5. SEM images of starch gelatin hydrogel and Au/Polyimide film attached on porcine skin. Viscoelasticity enables conformal attachment of starch-gelatin hydrogel on the rugged skin surface. Scale bar, 200 μm

We constructed a 15-channel mesh electronics array from bipolar input for surface electromyography (sEMG) intensity mapping (**Figure 2-2H**). We interfaced the electrophysiology-based ABLE device with the skin on a rat's leg and recorded the EMG signals evoked by sciatic nerve stimulation. Forming a the stable and conformal biointerface, the ABLE device resolved a high sEMG spatial intensity map over an area of 16 mm by 12.8 mm (**Figure 2-2I**), with an average signal-to-noise ratio (SNR) of 26.76 dB. By contrast, a gold biointerface (electronics without living hydrogel) recorded EMG signals with an SNR of 12.00 dB, indicating that the conformal nature of the ABLE facilitates electrophysiological signal transmission (**Figure 2-2J**).

2.2.2 Skin disease monitoring and therapy with ABLE

We applied the ABLE devices to a psoriasis mouse model (**Figure 2-6A**). Psoriasis is a chronic inflammatory disease that affects ~125 million people worldwide, with no complete cure.[31] Current treatment options often involve small-molecule drugs with potential systemic side effects. We conducted a series of preclinical evaluations using ABLE in the imiquimod (IMQ)–induced psoriasis model.[32] This model is widely used in in vivo research because of its clinical and histological similarities to human psoriasis, including characteristic symptoms such as desquamation, thickening of the epithelial structure, skin inflammation, and dysregulated host skin microbiota.[33]

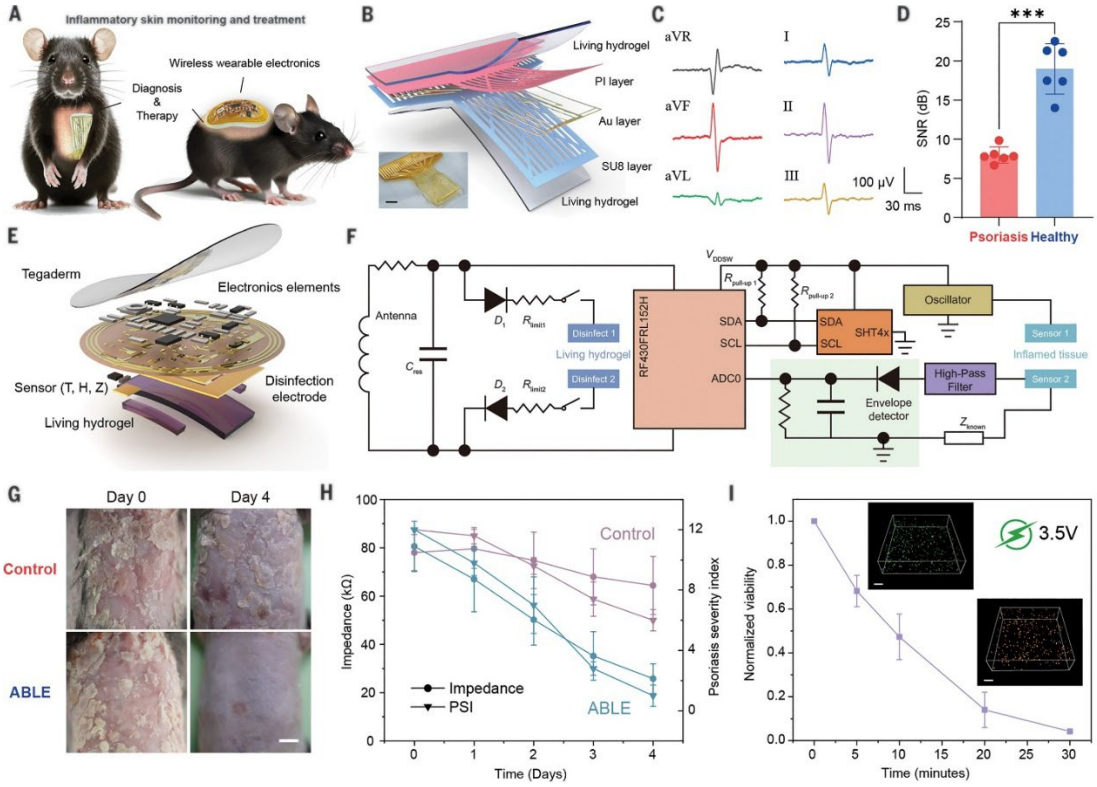

Figure 2-6. ABLE enables electrophysiological signal recording, diagnosis of psoriasis, and treatment of psoriasis. A. Schematic showing ABLE functionality in diagnosis and treatment of psoriasis. **B.** Schematic diagram and photograph show the structural configuration of the living hydrogel hybrid mesh electronics device for sECG recording. Scale bar, 5 mm. **C**. Representative six-lead electrocardiogram signals reveal heart rhythm in I, II, III, aVL, aVR, and aVF leads. **D**. Living bioelectronics device reports lower SNR in ECG recording in psoriasiform skin compared to controls. n = 6 independent channels. **E**. Schematic diagram shows the structural configuration of FPCB-based ABLE. **F**. Circuit diagram of wireless bioelectronics for skin monitoring and living hydrogel modulation. **G**. Representative photographs at day 0 and day 4 showing that ABLE treats psoriasis. Psoriasiform features including erythema, induration, and desquamation, are all substantially diminished. Scale bar, 5 mm. **H.** Impedance of psoriasis skin lesions, as measured using ABLE, indicates recovery progress. Results align with the psoriasis severity index (PSI). n = 5 independent animals. **I**. Disinfection electrodes on ABLE disinfect the living hydrogel through 3.5-V direct voltage within 30 min. Insets show confocal images of living hydrogel before (upper) and after

(lower) disinfection. Bacteria were stained with Baclight Live/Dead kit containing SYTO9/PI. Scale bar, 20 μm. $n = 5$ independent experiments. Control: mice with imiquimod (IMQ)–induced psoriasis, no treatment. ABLE: mice with IMQ-induced psoriasis, treated with active biointegrated living electronics. *P* values are determined by paired *t* test, two tailed. All data are presented as mean values ± SD.

We fabricated a mesh electronics device with a spin-coated living interface for six-lead surface electrocardiogram (sECG) recording (**Figure 2-6B**). Upon attachment to the chest area of healthy mice, the ABLE stably recorded the six-lead ECG (I, II, III, aVL, aVR, and aVF) with an average SNR of 18.97 dB (**Figure 2-6C**). By contrast, the ABLE recorded a significantly lower SNR of 7.96 dB in mice with psoriasis symptoms (**Figure 2-6D**), mainly attributed to the thickening of the psoriasiform skin. Hence, alterations in recorded electrophysiological signals offer qualitative information in the detection of skin diseases. When the ABLE device was applied to psoriatic skin for 4 days, we found that the SNR of recorded ECG was largely enhanced (day 0 versus day 4 recording) (**Figure 2-7**). This correlated with the visible improvements in psoriasisform features upon application of ABLE (**Figure 2-6G**). This improvement suggests that the living components within the ABLE system play an important role in mitigating the symptoms of psoriasis in mouse skin. These results demonstrate how the ABLE system may be used to record electrophysiological signals while concurrently providing biogenic cues through living components to regulate inflammatory skin diseases.

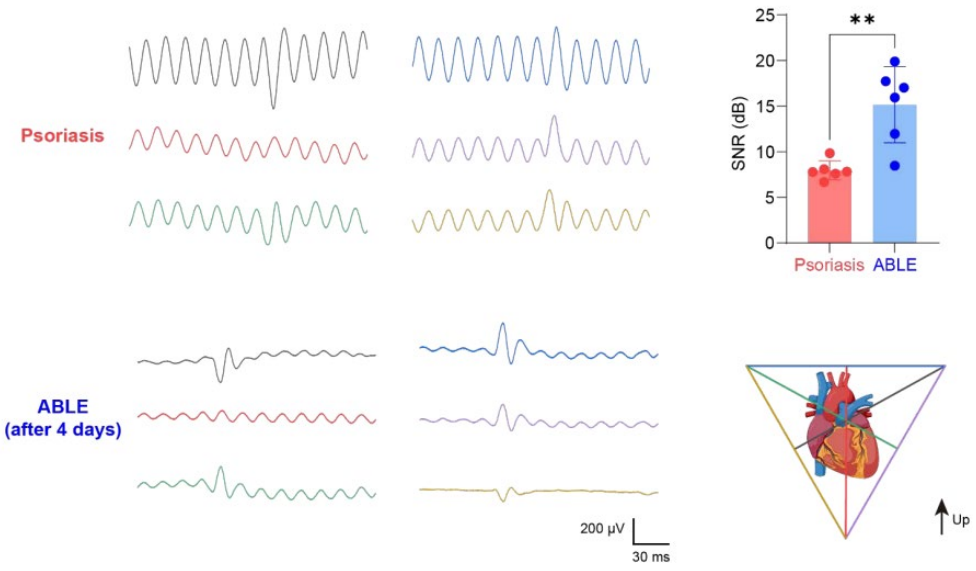

Figure 2-7. The 6-lead ECG signals acquired from each individual channel. It demonstrates a significant enhancement in signal-to-noise ratio (SNR) following a 4-day ABLE treatment period. P values are determined by paired t-test, two tailed. Data are presented as mean values ± SD. n=6 for each group.

To investigate the potential of ABLE in real-time monitoring and therapy and active circuit control, we created a battery-free, wireless flexible printed circuit board (FPCB). The FPCB-based ABLE can achieve comprehensive interplay between the three components (i.e., hydrogel, bacteria, electronics) (**Figure 2-1B and Figure 2-6E**). It is capable of (i) wireless energy harvesting and data transfer; (ii) real-time disease progress monitoring through skin impedance, humidity, and temperature sensing; and (iii) on-demand bacterial disinfection (**Figure 2-6F**). The acquired sensing data can be wirelessly transferred and remotely analyzed to monitor disease recovery progress and provide information for bacterial modulation.[34] Using the FPCB-based ABLE device, we could track the decrease in skin impedance upon alleviation of psoraisisform features during four days of treatment (**Figure 2-6H**).

2.2.3 Electrical interactions between bioelectronics and living hydrogel

Although application of living hydrogel in bioelectronics interfaces improved bioactivity for disease management, it presents practical challenges.[26] One major concern is that the *S. epidermidis* can

proliferate and colonize on skin, leading to infections and the development of virulence factors (34). Further, households are not equipped with proper biohazard containers to safely discard bacteria-laden materials. Thus, our FPCB included two modulation electrodes with triggers for delivering electrical current in terminal disinfection (**Figure 2-1B**). To maximize disinfection efficiency, we added a thin Au film to the back of the FPCB, which promotes reactive oxygen species generation in the hydrogels-electronics interface (**Figure 2-8**).

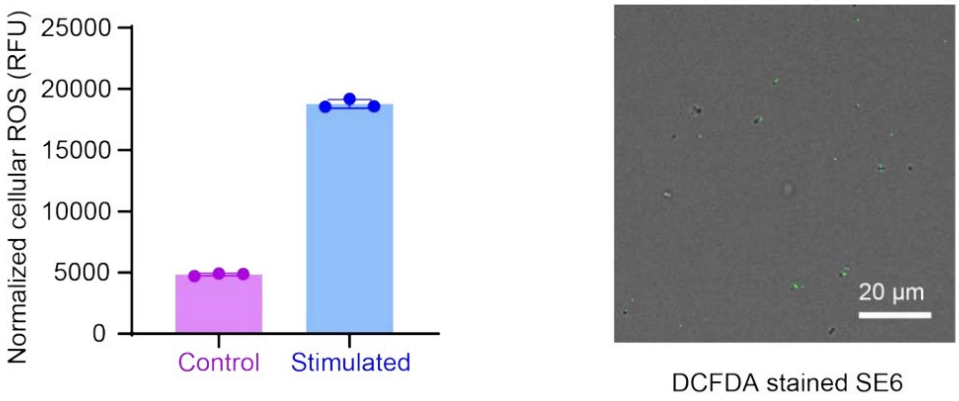

Figure 2-8. **DCFDA/H2DCFDA staining of living material shows intracellular ROS level increase upon electrical field (EF) stimulation.** Gelatin-encapsulated *S.epidermidis* treated for 3.5V, 10 min shows about 4x higher intracellular ROS fluorescence intensity compared to unstimulated control, when normalized with % viability from LIVE/DEAD assay. Data are presented as mean values ± SD. n=3 for each group.

Using bioelectronics for disinfection management, we can apply opportunistic pathogens (e.g., commensal bacteria) to the skin and minimize their potential long-term influences on skin health (**Figure 2-9**). Notably, ABLE is a general platform accommodating various bacterial species by providing both a supporting matrix and disinfection approaches (**Figure 2-10**). Moreover, upon treatment completion, two disinfection electrodes positioned in the ABLE deliver direct current to the living hydrogel interface for 30 min of disinfection (**Figure 2-6I** and **Figure 2-11**). This process effectively disinfects the bacteria present

within the living interface, as supported by the confocal microscope imaging (**Figure 2-6I**) This feature substantially reduces the biohazard risk associated with the living hydrogel.

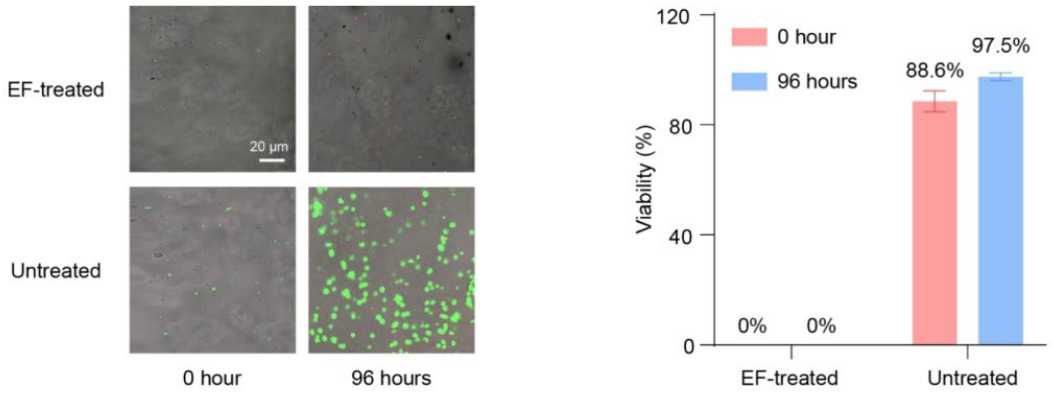

Figure 2-9. The electrically disinfected samples with *S. epidermidis* displayed neither proliferation nor any increase in viability after 96 hours. After 96 hours of growth at room temperature, disinfected bacteria showed low viability, which indicates that the bacteria were thoroughly deactivated. Bacteria are stained with SYTO9 (green)/PI (red). Data are presented as mean values ± SD. n=3 for each group.

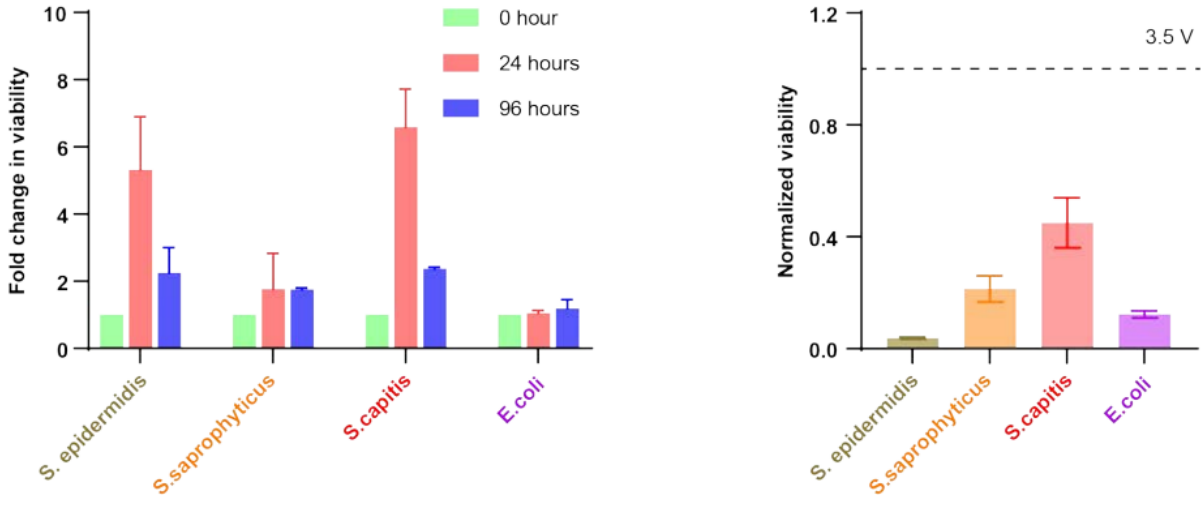

Figure 2-10. Different bacterial species can be incorporated into the ABLE design. (Left) Skin bacterial species, including Staphylococcus capitis and Staphylococcus saprophyticus, along with an

engineered bacterial strain such as Escherichia coli DH5α, demonstrate high viability within the hydrogel after 96 hours. (Right) Additionally, all these bacteria can be electrochemically disinfected through the ABLE control system using 3.5 V for 30 minutes. Data are presented as mean values ± SD. (n=3).

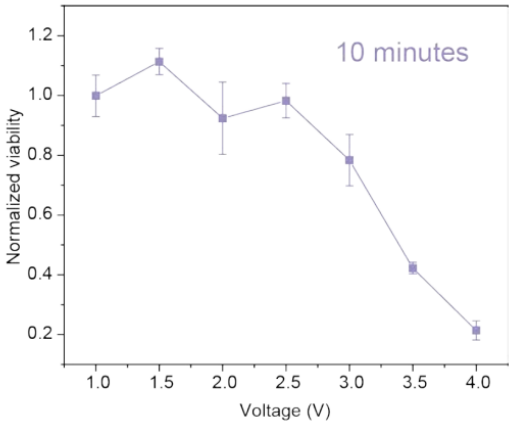

Figure 2-11. **A higher voltage output demonstrates a faster disinfection efficiency for living bioelectronics.** The disinfection time is set for 10 minutes. Data are presented as mean values ± SD. (n=3).

2.2.4 Mechanistic investigations of ABLE-based therapy

We studied how ABLE modulates the cellular environment in inflammatory skin conditions through biogenic cues (**Figure 2-1B).** Although the role of *S. epidermidis* in mediating skin homeostasis is widely known,[28,35] there is minimal literature on its therapeutic effects in psoriasis, let alone translation to clinic. Hematoxylin and eosin (H&E) staining showed significant reduction of epidermal thickening (hyperplasia), parakeratosis and cutaneous inflammation in skin lesions following ABLE treatment (**Figure 2-12A**). The hydrogel matrix alone in combination with the bioelectronics device (i.e., vehicle without bacterial component) showed limited therapeutic effect on psoriasis (**Figure 2-13**).

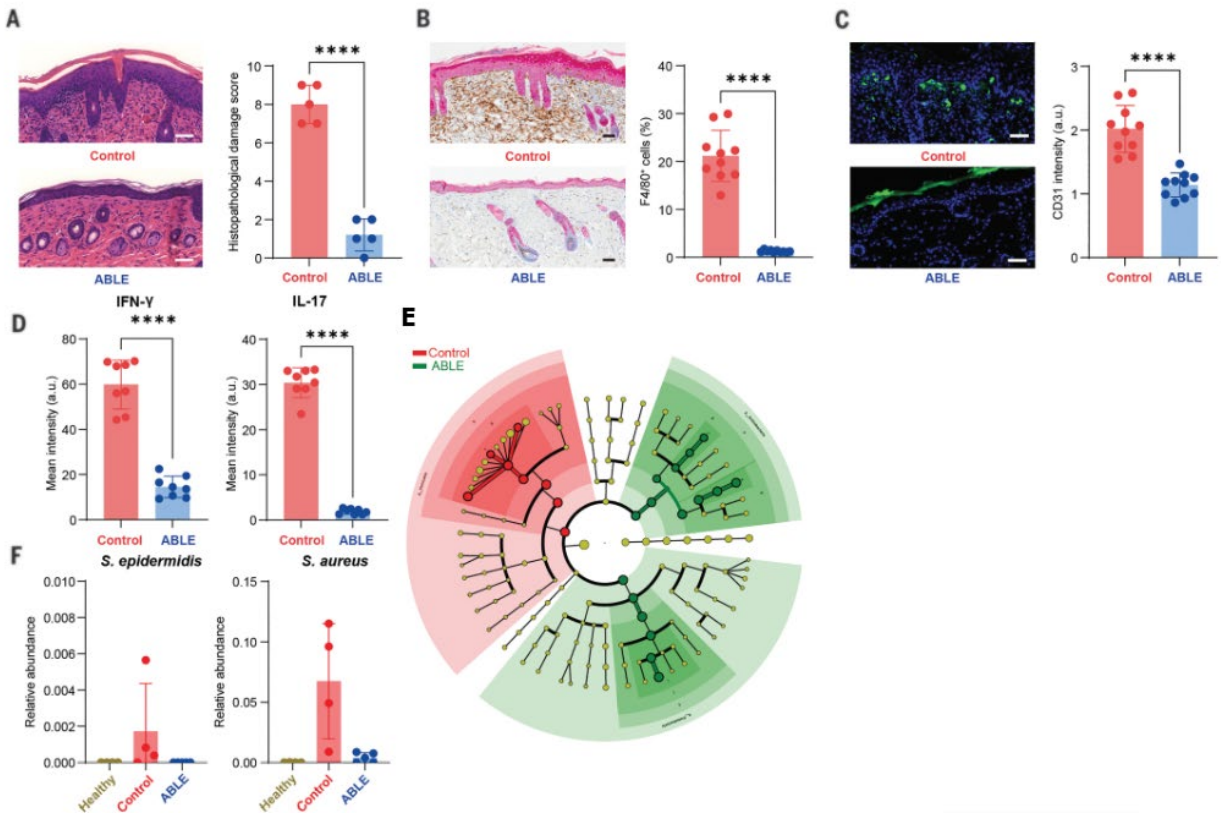

Figure 2-12. ABLE for studying living biointerface-tissue interaction in disease treatment. A. Representative images of H&E staining show substantially reduced pathological damage in psoriatic skin lesions of ABLE-treated mice. Scale bar, 50 μm. Histological score analysis shows a lower level of histological inflammation and tissue damage. n = 5 independent animals. **B**. Representative dual-immunohistochemical images of cytokeratin 14 and F4/80 staining indicate significantly decreased percentages of dendritic cells and macrophages in psoriatic skin lesions of ABLE-treated mice. Scale bar, 50 μm. n = 10 independent samples. **C**. Representative immunofluorescent images of CD31 staining indicate significantly decreased blood vessel formation in skin lesions of ABLE-treated mice. False positive signals in the ABLE image are due to unspecified staining in the stratum corneum. Scale bar, 50 μm. n = 10 independent samples. **D.** Cytokine analysis of the skin lesion indicates significant down regulation of IFN-γ and IL-17, which play an important role in inflammatory cell recruitment and regulate keratinocyte hyperplasia. n = 8 independent samples. **E**. LEfSe taxa analysis indicates altered bacterial diversity following ABLE treatment. **F**. *S. epidermidis* is barely detected on skin during ABLE treatment. Relative

abundance of *S. aureus* is reduced after ABLE treatment. $n \geq 3$ independent animals. **G**. Heatmap shows expression profile of psoriasis-related genes.

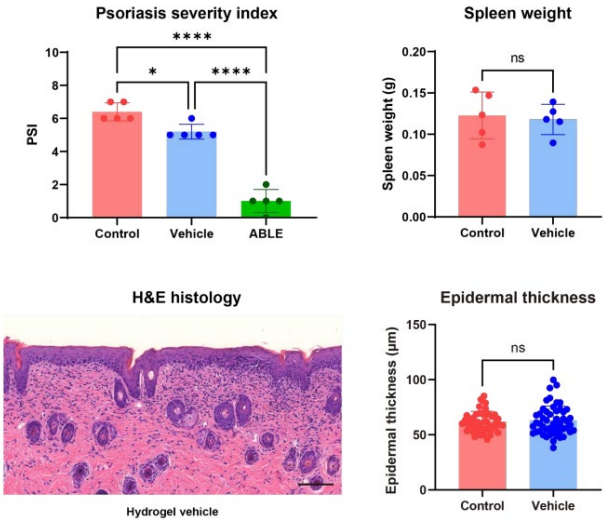

Figure 2-13. Hydrogel as the vehicle interface has limited therapeutic effect in treating psoriasis. Bioelectronics with non-living hydrogel matrix does not reduce the skin psoriasiform symptoms as indicated by psoriasis severity index (PSI). Besides, the symptoms regarding splenomegaly and psoriasiform hyperplasia still exist. Scale bar, 100 μm. P values are determined by t-test, twotailed. Data are presented as mean values ± SD. Images are representative of n = 5 different mice

Immunohistochemistry analysis (IHC) of cytokeratin 14 and F4/80 demonstrated a notable decrease in macrophages activities after ABLE treatment (**Figure 2-12B**). CD31 immunofluorescence and IHC staining both revealed fewer dilated blood vessels in ABLE-treated samples after 4 days compared to controls (mice with IMQ-induced psoriasis, no treatment) (**Figure 2-12C**). Cytokine profiling analysis showed reduced levels of inflammatory cytokines, with notable reductions in interleukin-17 (IL-17), interferon-γ (IFN-γ), tumor necrosis factor–α (TNF-α), and IL-1, which play a crucial role in promoting recruitment of inflammatory cells to psoriatic plaque lesions, regulating keratinocyte proliferation, and

disease development (**Figure 2-12D**). These findings collectively highlight the potential of living bioelectronics in modulating the inflammatory microenvironment and key aspects of psoriasis pathogenesis, including immune dysregulation, cellular proliferation, neovascularization, and cytokine-mediated inflammation.

To gain further insight into ABLE modulation of skin microbiota, we conducted 16S ribosomal RNA gene sequencing analysis of the treated skin samples. Linear discriminant analysis effect size (LEfSe) results indicated that ABLE effectively modulated the skin microbiota, inducing a transition from a psoriatic state to a healthier state (**Figure 2-12E**). A principal coordinates analysis plot of beta diversity showed that skin microbiota profiles in ABLE-treated mice were distinct from those in the control group but quite close to those in healthy mice (**Figure 2-14**). At the species level, we observed a low abundance of *S. epidermidis* on the skin (**Figure 2-12F**), indicating low *S. epidermidis*–related safety concern under the bioelectronics control. Furthermore, the abundance of S. aureus, a species known to be associated with psoriasis progression,[36] was also significantly reduced (**Figure 2-12F**). Altogether, changes in bacterial abundance can probably be attributed to the mutual interactions between different bacterial species and *S. epidermidis*.[37]

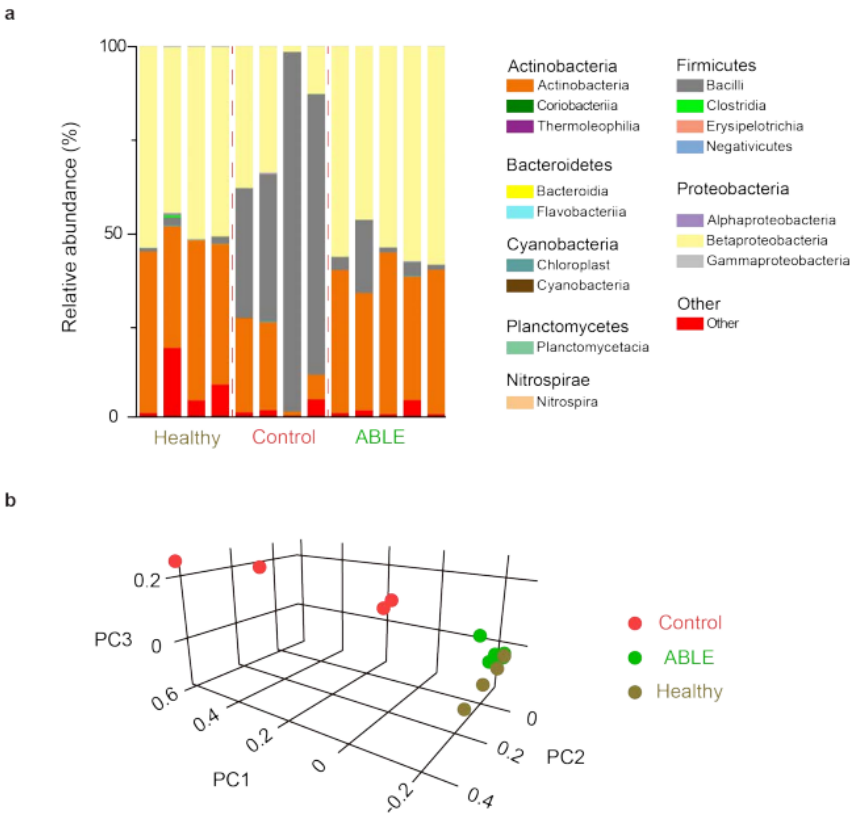

Figure 2-14. 16S rRNA sequencing result indicates that the ABLE could modulate the skin microbiota towards healthy conditions (a)Taxa composition plots illustrate the skin microbial compositions at different taxonomy levels from phylum to class. (b) Principal Coordinates Analysis (PCoA) plot of beta diversity revealed that ABLE-treated mice had distinct skin microbiota profiles from control group, but quite similar to healthy mice.

We sought to investigate the molecular mechanisms underlying ABLE-based regulation of the immune system and skin microbiota. Previous research has reported the inverse relationship between *S. epidermidis* and *S. aureus*, wherein *S. epidermidis* activates the host innate and adaptive immune system against *S. aureus* by the toll-like receptor 2 (TLR2) on dendritic cells.[28] This knowledge prompted us to explore the therapeutic effect of ABLE in the TLR2-knockout (KO) mouse strain B6.129-Tlr2$^{tm1Kir/J}$. We found that ABLE treatment in TLR2-KO mice did not result in the same therapeutic effects observed for wild-type mice (**Figure 2-15**).

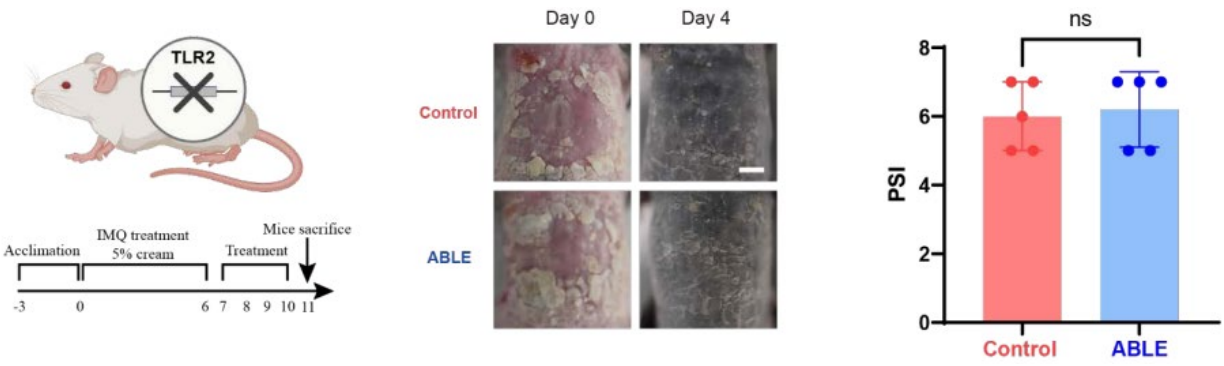

Figure 2-15. ABLE treatment didn't show therapeutic effects on psoriatic skin of TLR2 knockout (TLR2 KO) mice. (Left) schematic of the experimental design. (Middle) on Day 4 post ABLE treatment (ABLE), the psoriatic skin looks similar to the untreated control group (Control), in terms of the severity of psoriatic symptoms. This indicates no obvious therapeutic effects by ABLE. (Right) PSI score indicates that ABLE treatment didn't significantly alleviate psoriatic symptoms on Day 4. Scale bar, 5 mm. P values are determined by t-test, two-tailed. Data are presented as mean values ± SD. n=5 for each group.

Furthermore, we investigated the contribution of TLR2 ligands produced by S. epidermidis to the anti-psoriasis effect of ABLE system (**Figure 2-16**). In vitro cellular cytokine analysis indicates that lipoteichoic acid (LTA) derived from *S. epidermidis can* down-regulate the expression of psoriasis-related cytokines and chemokines in plasmacytoid dendritic cells and epidermal cells (**Figure 2-17**). These pieces of evidence suggest that LTA might act as one of the TLR2 ligands mediating ABLE's immunoregulation function.

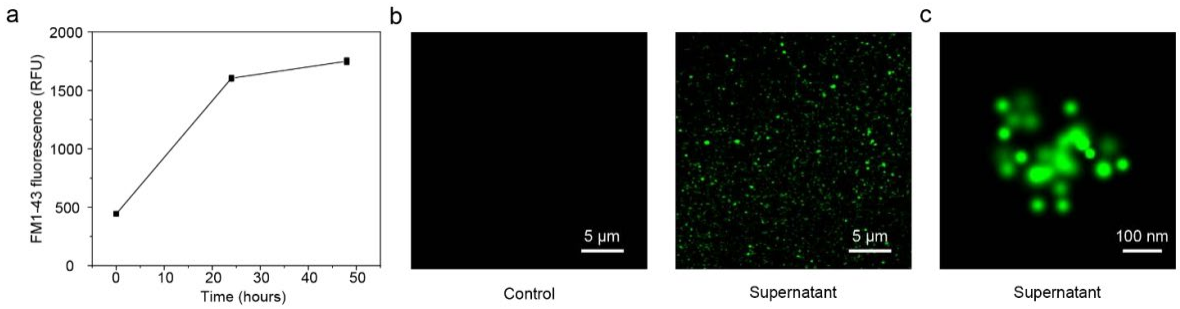

Figure 2-16. Bacterial debris and fragments are released from the living hydrogels. All samples were collected from the supernatant solution in contact with the ABLE device which was filtered with 0.22 μm

syringe filter to remove bacterial cells before measurement and imaging. (a) The FM1-43 membrane probe shows increased fluorescence over time, indicating the release of nonviable bacterial remnants from the living hydrogels. (b) Confocal microscope images reveal the presence of lipoteichoic acid (LTA; green), a bioactive compound potentially related to the therapeutic effect, in the supernatant. Scale bar, 5 µm. (c) dSTORM imaging provides a superresolution image of LTA-labelled bacteria debris. Scale bar, 100 nm. Data are presented as mean values ± SD. (n=3).

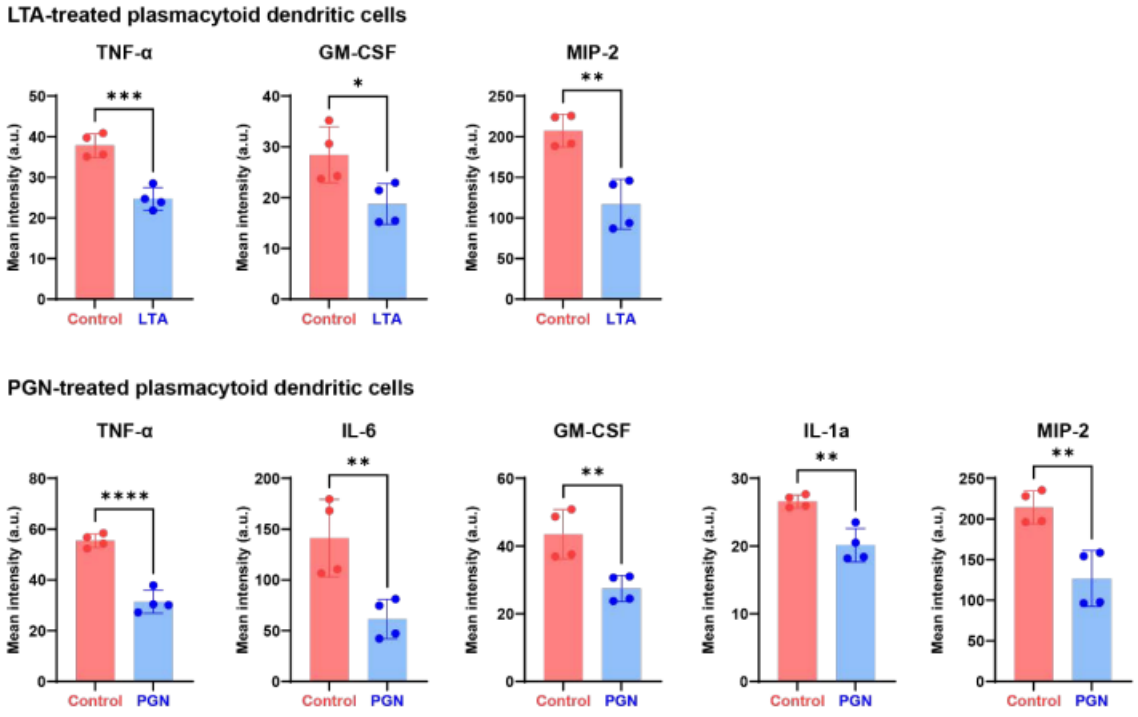

Figure 2-17. Lipoteichoic acid (LTA) and peptidoglycan (PGN) from *S. epidermidis* show the capabilities to downregulate the psoriasis-related cytokines in plasmacytoid dendritic cells. P values are determined by t-test, two-tailed. Data are presented as mean values ± SD. n=3 for each group.

2.3 Discussion and outlook

We validated how LMs can be integrated in bioelectronics as a soft and bioactive interfacial material for treating complex autoimmune disease. We delved into the synergy that can arise through such integration, spanning biogenic, bioelectrical and biomechanical domains. Importantly, we demonstrated that bioelectronics can actively regulate LMs through application of DC current, controlling bacterial viability and bioactivity. Part 3 of this thesis delves deeper into the active interaction between the electronic and living components in the context of infection control.

2.4. Experimental

2.4.1 Synthesis of hydrogel composite

A starch gelatin hydrogel was prepared by mixing tapioca starch (15 wt%), gelatin (10 wt%), and deionized water or tryptic soy broth (TSB) medium (cat. no. 22092). The mixture was then heated in an oil bath at 80°C for 30 minutes to facilitate the gelatinization of starch. Subsequently, the hydrogel was transferred to a 4°C refrigerator for gelation. To create a living hydrogel, Staphylococcus epidermidis (S. epidermidis; strain NIHLM087, kindly provided by Dr. Julia Segre at NIH, NCBI taxonomy ID: NCBI:txid979201) was cultured in TSB medium at 37°C until the optical density at 600 nm (OD600) reached a range of 2.80 to 3.00. Then, 1ml of cultured bacteria solution was aseptically added and vigorously mixed with the starch-gelatin hydrogel at 42 °C water bath. Identical protocol was used for synthesis of living hydrogel containing Staphylococcus capitis (ATCC #35661), Staphylococcus saprophyticus (ATCC #15305) or Escherichia coli DH5α (Thermo Fisher Scientific #18265017). For the synthesis of granular starch-gelatin hydrogel, gelatin and TSB medium were mixed and heated at 80°C for 30 minutes. After cooling the mixture in a 42°C water bath, tapioca starch was aseptically added. To synthesize polyacrylamide hydrogel, AA (3.5 wt%), APS (0.1 wt%) and MBAA (0.01 wt%) were mixed vigorously in deionized water. After 30 minutes, the accelerator TEMED (0.02 wt%) was added into the mixture and quickly mixed before pouring into acrylic molds for subsequent polymerization at room temperature.

2.4.2. Confocal laser scanning microscopy

Staphylococcus epidermidis was subjected to staining using the LIVE/DEAD BacLight Bacterial Viability Kit (Molecular Probes), following the guidelines provided by the manufacturer. The stained samples were then visualized using a Stellaris8 falcon WLL confocal microscope, equipped with a 63x objective. In the microscope images, live cells exhibited a green fluorescence (SYTO9), while dead cells appeared red (PI). To determine the percentage of viability, individual cells or colonies were threshold and counted using ImageJ software. For the reconstruction of Zstack images, Imaris from Oxford Instruments was employed. To visualize the process of starch gelatinization, the reducing ends of tapioca starch were marked with 8-amino-1,3,6- pyrenetrisulfonic acid (APTS). The hydrogel was soaked in an APTS solution (20mM, mixed in 15% acetic acid), followed by the addition of 500mM sodium cyanoborohydride. This blend was incubated at 25°C for 15 hours, then rinsed five times with deionized water to remove any unattached dye. It was later suspended in 50% glycerol to deter water evaporation. Visualization was done using a Stellaris8 Falcon WLL confocal microscope with a 100x objective lens. The excitation was set at 488nm with a detection range of 500 to 580 nm. To visualize bacterial distribution within the hydrogel matrix, the APTS-marked hydrogel was heated to 42°C, and Staphylococcus epidermidis, stained with FM1-43 (5μM), was introduced. Post-solidification, image was captured on two separate channels. Acquired images were processed using ImageJ software and then reconstructed using Imaris by Oxford Instruments.

2.4.3 Polymer screening

To conduct the polymer biocompatibility test, a mixture was prepared by combining 3 ml of TSB containing Staphylococcus epidermidis with an OD600 of 0.25-0.30 and 1% w/v of polymers as outlined in Table S1. Tragacanth and glucomannan (0.5%) was used at lower w/v percentages as the polymer formed gel which could not be pipetted at 1%. The resulting polymer-bacteria suspension was then placed inside an orbital shaker and incubated at 37°C, shaking at a speed of 200 rpm for a duration of 3 hours. Before and after the incubation period, 100 μl of the suspension was sampled and mixed in a 1:1 ratio with the BacTiter-Glo™ Microbial Cell Viability Assay kit (Promega). The luminescence emitted by the samples was measured

using a Synergy Neo HTS Plate Reader. The fold change in viability was determined by dividing the luminescence reading obtained after 3 hours of incubation by the luminescence reading obtained at 0 hour and further normalized by the control group without any polymers.

Table 2.1. List of chemicals used for compatibility test with *S. epidermidis*

Chemicals	Vendor	Product No.
Starch acetate (Ace-starch)	BOC Sciences	9045-28-7
Cationic starch (Cat-starch)	BOC Sciences	56780-58-6
Cellulose, microcrystaline, powder, 20 µm	Sigma-Aldrich	310697-1KG
Chitosan	Sigma-Aldrich	417963-100G
β-1,3-glucan from *Euglena gracilis*	Sigma-Aldrich	M2378-100G
Pectin citrus	Alfa Aesar	J61021.22
Kappa-Carrageenan	Acros Organics	431591000
Tragacanth	Sigma-Aldrich	G1128-100G
Poly(ethylene glycol), average Mn 950-1050	Sigma-Aldrich	P3515-1KG
Poly(vinyl alcohol), Mw 85000-124000	Sigma-Aldrich	363146-500G
Polyethylene	Sigma-Aldrich	427799-1KG
Nanoclay, hydrophilic bentonite	Sigma-Aldrich	682659-500G
Nanoclay, surface modified, contains 35-45 wt. % dimethyl dialkyl (C14-C18) amine	Sigma-Aldrich	682624-500G

2.4.4. Long-term viability test

To monitor the long-term viability of S. epidermidis, S. capitis, S. saprophyticus, and E.coli DH5α within the hydrogel phase, samples of starch gelatin hydrogel (granular and gelatinized) were collected at 0 hour, 24 hours, and 96 hours. These samples were placed in glass vials and weighed. To dissolve the sampled hydrogel, 10 ml of PBS was added, and the vials were incubated at 42°C for 10 minutes. The resulting solution, containing the released bacteria, was mixed with the BacTiter-Glo™ Microbial Cell Viability Assay kit (Promega #G8230) in a 1:1 ratio. The luminescence emitted by the samples was recorded using

a Synergy Neo HTS Plate Reader. To obtain normalized viability measurements, the raw luminescence values were divided by the sampled mass of the hydrogel and further normalized by the viability measurement obtained at 0 hour, serving as the reference point.

2.4.5. Long-term storage of the living hydrogel

For freeze-drying storage, an Eppendorf tube filled with a starch-gelatin hydrogel with live S. epidermidis was frozen in a dry ice/ethanol bath for 20 minutes. It was then subjected to freezedrying in a FreeZone 4.5 Liter Benchtop Freeze Dryer at -43°C for a day, and later stored in a freezer set at -80°C. After 30 days, the dried hydrogel was rehydrated with 10ml of deionized water, left at room temperature for two hours, and a sample was taken for viability measurements. This rehydrated mixture was allowed to sit at room temperature overnight for rejuvenation, and another sample was taken for viability measurements at 31 days. To dissolve the sampled hydrogel, 10 ml of PBS was added, followed by heating at 42°C for 10 minutes. The ensuing liquid, which contained the liberated bacteria, was combined at an equal ratio with the BacTiter-Glo™ Microbial Cell Viability Assay kit (Promega #G8230). Using a Synergy Neo HTS Plate Reader, the luminescence from the samples was measured. To obtain normalized viability measurements, the raw luminescence values were divided by the sampled mass of the hydrogel and further normalized by the viability measurement obtained at 0 hour, serving as the reference point. Identical protocol was followed for living hydrogel stored in 4°C, -20°C and -80°C, except that freeze-drying was not performed.

2.4.6 Intracellular reactive oxygen species (ROS) assay

A 2 mm thick living hydrogel was placed onto the patterned disinfection electrodes. Subsequently, electrical stimulation was applied to the living hydrogel at a condition of 3.5 V for a duration of 10 minutes. Following the electrical stimulation, the samples were liquefied and then diluted 10- fold with phosphate-buffered saline (PBS) to ensure the complete release of bacterial cells. The released cells were washed once with PBS and resuspended in a staining solution obtained from the DCFDA/H2DCFDA - Cellular ROS Assay Kit (ab113851). The intracellular ROS level was measured using a Synergy Neo HTS Plate Reader. To

standardize the raw fluorescence intensity, it was divided by the percentage viability determined using the LIVE/DEAD BacLight Bacterial Viability Kit.

2.4.7. Scanning electron microscope

A scanning electron microscope (SEM; Carl Zeiss, Merlin) was used to image the morphology of multiple samples, including S. epidermidis-encapsulated living hydrogels, porcine skin attached to living hydrogels and Au/PI film. Samples were fixed in 3% glutaraldehyde, followed by washing in DI water and dehydration with an increasing ethanol gradient. Samples were dried in a critical point dryer (Leica EM CPD300) and 8nm Pt/Pd coating was applied before imaging with the SEM at 10kV.

2.4.8. Living hydrogel disinfection demonstration

The living hydrogel with S. epidermidis was first put onto disinfection electrodes and then the electrical potential was applied for the desired duration. Subsequently, a sample of the treated hydrogel was collected and measured inside a glass vial. The sampled hydrogel was dissolved by adding 10 ml of PBS and incubating the mixture at 42°C for 15 minutes. The resulting solution, containing the released bacteria, was combined with the BacTiter-Glo™ Microbial Cell Viability Assay kit (Promega #G8230) in a 1:1 ratio. Luminescence was measured using a Synergy Neo HTS Plate Reader. Concurrently, a control group sample was run in parallel, following an identical procedure, except without electric stimulation. The raw luminescence data obtained was normalized by the sampled mass, and the differences between the control and treated groups were calculated to determine the normalized viability. Identical protocol was used for disinfection of living hydrogel containing S. capitis, S. saprophyticus, or E. coli DH5α. For demonstrating thoroughness of disinfection, living hydrogel containing S. epidermidis was disinfected at 3.5V for 30 min. The disinfected and untreated control samples were drop casted on separate glass bottom dishes and left at room temperature. At 0 hours and 96 hours, the samples in the glass bottom dishes were treated with SYTO9/PI and imaged on Leica Stellaris8 Falcon WLL confocal microscope with a 63x objective lens. Percentage viability in stained area was quantified using ImageJ. For disinfection of bacteria in liquid

culture, overnight-cultured S. epidermidis was diluted in a 1:10 ratio in TSB medium. 400 µl of the diluted bacterial solution was drop casted the disinfection electrode contained by a PDMS mold and the electrical potential was applied for the desired duration. The resulting suspension was mixed with BacTiter-Glo™ Microbial Cell Viability Assay kit (Promega #G8230) in 1:1 ratio and the viability were quantified identical to the disinfection of living hydrogel.

2.4.9. Bacterial motility test

To prepare the solution phase sample, SYTO9-stained *S. epidermidis* was resuspended in fresh TSB medium (OD600=1.0). For the gel phase sample, SYTO9-stained *S. epidermidis* was enclosed within a starch-gelatin hydrogel. A volume of 10 µl from either the liquid suspension or the starchgelatin hydrogel was then added to a 50 mm glass-bottom dish and covered with a glass coverslip. To facilitate imaging, the glass-bottom dish was placed on an INUB-ONICS TOKAI HIT Standard Heating Stage Top Incubator (UNIV-D56) set to a temperature of 25°C. Using a Nikon Ti2 microscope with 488 nm excitation, a video of *S. epidermidis* was recorded. Subsequently, the video was analyzed using the TrackMate plugin in ImageJ. The average speed of individual cells was calculated by dividing the total displacement by the tracking time.

2.4.10. Quantification & characterization of released components

For quantification of released bacteria, 10 ml of PBS was added to the starch-gelatin hydrogel contained in a glass vial. During incubation at room temperature, aliquots of PBS were collected at 0, 1, 3, 5, and 6 hours. After 6 hours, the vials were heated to 42°C for 10 minutes to completely release bacteria into the PBS solution. The samples were mixed with the BacTiter-Glo™ Microbial Cell Viability Assay kit (Promega, G8230) in a 1:1 ratio, and luminescence was measured using a Synergy Neo HTS Plate Reader. The percentage of released bacteria was quantified by comparing the luminescence of the PBS aliquots with that of the totally released fractions. For the quantification of released bacterial debris and fragments, the living hydrogel was synthesized as described earlier, except that Tris-buffered LB was used instead of TSB. 5 ml of Tris-buffered LB was added on top of the starch-gelatin hydrogel, and aliquots were collected at 0

hour, 24 hours, and 48 hours at room temperature. Aliquots were centrifuged for 5 min at 5000 rpm and filtered with a 0.22 μm syringe filter to remove impurities. The solution was plated on tryptic soy broth agar to confirm the absence of viable bacteria. The resulting solution containing released bacterial fragments was stained with 5 μM FM1-43 (Invitrogen, T3163). The fluorescence was measured with a Synergy Neo HTS Plate Reader.

2.4.11. Visualizing lipoteichoic acid (LTA) in released debris

To visualize lipoteichoic acid (LTA), the solution containing the released bacterial debris was drop-cast onto a poly-L-lysine-coated glass bottom dish and left to attach overnight at room temperature. After attachment, the glass bottom dish was washed three times with PBS, and the attached cell fragments were fixed with 4% (v/v) formaldehyde for 15 minutes. Following fixation, any unreacted aldehyde groups were neutralized with 0.2% $NaBH_4$, followed by additional washing with PBS. The LTA antibody mAB 55 (#HM2048, Hycult Biotech) was diluted 1:100 in a blocking buffer (3% BSA in PBS) and applied to the glass bottom dish. After incubating for 1 hour at room temperature, the buffer was removed, and the dish was washed three times with PBS. The samples were then stained with Goat anti-Mouse IgG (H+L) Secondary Antibody - Alexa Fluor™ 488 (Invitrogen, A-11001) at a 1:100 dilution for 1 hour at room temperature. For confocal microscopy imaging, the washed samples were submerged in PBS and imaged using a Stellaris8 Falcon WLL confocal microscope with a 100x objective lens. A negative control sample, subjected to the same staining procedure but with PBS replacing the bacterial debris solution, showed no signal under identical imaging conditions. For dSTORM imaging, the washed samples were initially submerged in STORM buffer, comprising 100 mM cysteamine, 5% glucose (w/v), 0.5 mg/ml glucose oxidase, and 38 μg/ml catalase in PBS. Imaging was conducted using an ONI Nanoimager with 140mw laser power (488 nm). Localization filters from the Nanoimager software were applied to visualize the reconstructed images.

2.4.12. Electrical analysis

For electrical characterization of starch-gelatin hydrogel, two Pt wire electrodes (Sigma-Aldrich, BASMW1032) were inserted into starch-gelatin hydrogel contained in a glass vial. Potentiostatic electrochemical impedance spectroscopy (PEIS) and cyclic voltammetry (CV) measurements were conducted using the electrochemical workstation (Biologic SP-200). The impedance measurement spanned a frequency range of 100 kHz to 1 Hz, utilizing a sinusoidal amplitude of 20 mV. Cyclic voltammetry was performed at the scan rate of 100 mV/s.

2.4.13. Mechanical analysis

A rotational ARES rheometer (TA Instruments) equipped with parallel plates was employed to evaluate the viscoelastic properties of the living hydrogel. To preserve the hydration of the hydrogel, the samples were surrounded with water throughout the experiments. Prior to each measurement, a slight contact force was applied to ensure proper contact between the plates and samples. The samples were allowed to soak for 100 seconds, enabling relaxation and rebalancing within the surrounding environment. The shear modulus was determined by subjecting the samples to an oscillatory shear strain of 1% at a frequency of 1Hz, unless stated otherwise. To explore the effects of humidity and temperature on the mechanical properties of living hydrogels, a Discovery HR-30 shear rheometer (TA Instruments) equipped with a relative humidity accessory was used, following the same procedure. The adhesion strength was tested using the standard tensile test (ASTM F2258) at the Zwick-Roell ZwickiLine Z0.5. All tests were conducted at a constant tensile speed of 50 mm/min. Fourier-Transform Infrared Spectroscopy (FTIR) To investigate the molecular interaction between starch and gelatin macromolecules, the different hydrogel samples with D2O (Sigma Aldrich) was measured by the Shimadzu IRTracer-100 Fourier transform infrared spectrophotometer

2.4.14. Fabrication of the flexible printed circuit board

Custom-designed flexible printed circuit boards were manufactured by commercial vendors, such as PCBWay, in compliance with the ISO 9001 certificate. The electronic components integrated into the circuit

boards included passive elements like capacitors, resistors, and diodes. Additionally, the boards had a temperature and humidity sensor (Sensirion, model no. SHT40-AD1F-R2 or SHT45-AD1F-R2), an ISO 15693 sensor transponder with a programmable low-power microcontroller (Texas Instruments, model no. RF430FRL152H), a crystal oscillator (Epson Timing, model no. SG-3030LC 32.7680KB6:PURE SN), and two operational amplifiers (STMicroelectronics, model no. TSV620AILT). All circuit components were soldered using leadfree no-clean solder (Chip Quik Inc., model no. Sn96.5Ag3Cu0.5 (96.5/3/0.5), melting point range of 217~220 °C)) through hot-air blowing. To optimize bacterial electrical modulation efficiency, two stimulation electrodes were patterned with 100 nm Au metal layers for bacterial disinfection electrode geometry or bacteria stimulation electrode geometry using an electron-beam evaporator (EvoVac, Angstrom Engineering). To prevent chronic electrochemical corrosion of the electrodes, silver/silver chloride (Ag/AgCl) conducting paste (Nagase ChemteX, model no. CI-4040) was applied and printed onto electrode area, followed by curing on a hot plate at 70 °C for 30 minutes. The original electrode area was subsequently encapsulated with an elastomeric polyurethane coating (Smooth-On, model no. Clear Flex 50) and cured at 70 °C for 30 minutes. The living hydrogel interface was positioned between the two disinfection electrodes, while the non-living hydrogel interface was placed separately on the two sensing electrodes. For the sterilization procedure, once users have finished using the ABLE device, or in any emergency, they can activate the disinfection electrode by closing its trigger. A complete disinfection typically requires 30 minutes. Extending this waiting period slightly is recommended for optimal results. After the disinfection process, the user can dispose of the used living bioelectronics

2.4.15. Fabrication of mesh electronics and hydrogel hybrid

The initial cleaning of a P-type wet oxide silicon wafer (#HS39626-WO, NOVA Electronic Materials) was performed, which involves immersion in acetone and isopropyl alcohol (IPA) for 3 minutes each within an ultrasonic bath. Following this, hexamethyldisilazane (HDMS) is applied to the wafer as a treatment. A solution of poly (pyromellitic dianhydride-co-4,4′-oxydianiline) (Sigma Aldrich, 575801-1L) is then added to the treated wafer using a spin-coating method at a speed of 1500 rpm. To cure the applied solution, the

wafer is then heated in a resist oven at a temperature of 300 degrees Celsius for a span of 3 hours, after which it is allowed to cool down naturally to room temperature. The end result is a polyimide (PI) film of approximately 5 micrometers in thickness. The PI-coated wafer then undergoes another round of spin-coating, this time with AZ nlof 2020, followed by an exposure process to develop patterns. The wafer is then subjected to an evaporation process with 5 nm Titanium and 200 nm Gold, which is followed by a lift-off in AZ NMP to get rid of the photoresist. Subsequently, the wafer is patterned with AZ 40XT-11D, which serves as a protective mask against etching. The patterned PI layer is achieved via Reactive Ion Etching (RIE) in a Plasma-Therm Inductively Coupled Plasma (ICP) Fluoride Etch. Post-etching, the photoresist is removed by soaking in N-Methyl-2-pyrrolidone (NMP) within an 80-degree Celsius bath for 10 minutes. The encapsulation layer, composed of SU-8 3005 (MicroChem Corp), is patterned to cover the metal interconnects while leaving the sensing pads and bottom pads exposed to interface with cardiac tissues. Finally, to retrieve the mesh electrode, it can be detached using a water-soluble transfer tape. Alternatively, manual peeling is an option, provided it does not cause any damage to the devices. Hydrogel hybridization is made by attaching mesh electronics to the hydrogel-coated PDMS. The hydrogel layer is formed by spin-coating hydrogel precursor solution with different revolutions per minute (rpm). After cooling down and trimming, the hydrogel-hybrid devices were carefully peeled off from the PDMS substrate.

2.4.16. Fabrication of conventional bioelectronics

The fabrication of microneedle bioelectronics involved assembling disposable hypodermic needles (22 G x 1 ½", Air-Tite Products) in the same pattern as the flexible mesh electrodes. This process began with the patterning of acrylic plates using a laser cutter (VLS 4.60), creating an array of holes tailored for needle insertion. After inserting the needles into these holes, they were secured in place using epoxy glue (MG Chemicals). Subsequently, the needles were soldered to a 36-pin wire adapter (Intan Technologies) to complete the assembly. The fabrication of planar multichannel electrode arrays adopts a similar procedure to that of the flexible mesh designs, allowing for patterning on silicon wafers, glasses, and polyimides. This

procedure is similar to that of flexible mesh fabrication, except it does not involve polyimide substrate curing, reactive ion etching, or peel-of.

2.4.17. Animals

The care of animals, including mice and rats, adhered to federal, state, and local guidelines. All animal experiments were conducted in compliance with the regulations and were approved by the Institutional Animal Care and Use Committee (IACUC) at the University of Chicago. The animals including C57BL/6J mice (JAX #000664), B6.129-Tlr2tm1Kir/J (TLR2 KO) mice (JAX #004650), B6(Cg)-Tlr4tm1.2Karp/J (TLR4 KO) mice (JAX #029015), and Sprague Dawley rats were either obtained through mating or purchased from commercial vendors such as Jackson Lab (JAX) and Charles River. The animal room was maintained in an environment with humidity of 40-60 % and the temperature of 18-23 °C under a 12-h light/12-h dark cycle. The animals were allowed free access to food and water. All animal procedures were approved by the IACUC in protocols # 72378 (rat) and 72621 (mice).

2.4.18. Rat in vivo electromyography (EMG) recording

An adult rat ranging between 12 and 24 weeks and inclusive of both genders, was deeply anesthetized using 2-4% isoflurane. Fur from the animal's hindquarters was removed using surgical clippers and depilatory cream. A midline incision was made in the skin, following which the fascial plane between the gluteus maximus and the anterior head of the biceps femoris was opened, thereby exposing the sciatic nerve. The nerve was gently drawn-out using sutures, and a flexible Ti-Au/Polyimide electrode (thickness 10 nm/200 nm/5 μm) was coiled around the nerve bundle for the purpose of electrical stimulation. Then the hydrogel-coated mesh electrode was adhered to the rat's leg to facilitate multi-channel EMG recordings in response to sciatic nerve stimulation. Electrical stimulation was performed using a 2 ms biphasic electrical current ranging from 100 to 800 μA, which elicited muscle movement. For the recording process, an Intantech RHD USB interface board and an RHD 16-channel bipolar-input recording headstage were employed.

Signals were recorded at a rate of 20 kS s-1 within the 100-1000 Hz bandwidth. All signal-to-noise ratio (SNR) in this paper is defined as:

$$SNR_{dB} = 10\ log_{10}(\frac{P_{signal}}{P_{noise}})$$

2.4.19. Psoriasis model

Eight-week-old male C57BL/6J mice (JAX #000664), B6.129-Tlr2tm1Kir/J (TLR2 KO) mice (JAX #004650), and B6(Cg)-Tlr4tm1.2Karp/J (TLR4 KO) mice (JAX #029015) were housed in groups of five mice per cage and acclimatized for 3 days before inclusion in the investigation. To induce psoriasiform dermatitis, the mice were shaved and topically applied with 5% IMQ cream (Perrigo Pharmaceutical) for 7 consecutive days unless otherwise noted. The IMQ induced mice were either treated with ABLE system, methotrexate, or the hydrogels containing lipoteichoic acid (LTA) or peptidoglycan (PGN) extracted from *S. epidermidis*, LTA inhibitor LtaS-IN-1 (Med Chem Express #HY-135813) treated *S. epidermidis* or Proteinase K (Sigma #3115836001) for 4 days. For the therapeutic experiments, living bioelectronics with or without living components were topically applied to mouse dorsal skin for skin sensing and therapy. Methotrexate was orally administered daily at a dose of 1 mg/ml in a 0.5% carboxymethyl cellulose (CMC) solution. Proteinase K was used at a concentration of 1 mg/ml. The quantity of lipoteichoic acid (LTA) and peptidoglycan (PGN) used is equivalent to their respective purification yields from the bacteria in living hydrogel systems. LtaS-IN-1 was co-cultured with bacteria at a concentration of 10 μmol/L overnight. Tegaderm (3 M™) or band-aid were then used to fix the position of bioelectronics. Dressing was changed every day. During the experiment, changes in skin psoriasiform information including erythema, induration, and desquamation were recorded daily. The mice were euthanized on the last day of the experiment and their skin and spleen were harvested for histological evaluation and other assays, such as cytokine profiling and flow cytometry analysis. The general psoriasis symptoms, including the redness, scaling, and thickness (induction) of murine skin, were evaluated to score the “Psoriasis severity index (PSI)”, which assesses the severity of the induced erythema, desquamation, and induration of the psoriasis. Each parameter was

measured on a scale of 0–4 (from none to the maximum damage). The sum of these four values was the value of the PSI index, with the maximum value of 12

2.4.20. Lipid teichoic acid (LTA) extraction

In a typical experiment, the *S. epidermidis* bacterial pellets from a 10 ml overnight culture were resuspended in 50 mL of 0.1 M sodium citrate buffer (pH 4.7) and sonicated for 30 minutes in an ice-cold bath. Then, the suspension was mixed with 50 mL of n-butyl alcohol and stirred for 2 hours using a magnetic stirrer. After phase separation by centrifugation, the LTA-containing aqueous phase was collected, dialyzed against pure water overnight, and then lyophilized. The crude extract was purified using octyl agarose gel CL-4B, which was pre-equilibrated with 15% n-propanol in 0.1 M ammonium acetate solution (pH 4.7), and then eluted with a linear gradient of 15–60% n-propanol in 0.1 M ammonium acetate buffer. The eluent containing LTA was dialyzed overnight and aliquoted into 10 tubes for further use.

2.4.20. Peptidoglycan (PGN) extraction

In a typical experiment, the *S. epidermidis* bacterial pellets from a 10 ml overnight culture were resuspended in 5 ml of 1 M sodium chloride and boiled at 100°C for 20 minutes. After centrifugation at 10,000 rpm for 5 minutes, the pellets were washed with ddH2O and resuspended in 5 ml of ddH2O for incubation in a sonicated water bath for 30 minutes. Then, 2.5 ml of digestion solution I (15 µg/ml DNase and 60 µg/ml RNase in 0.1 M TRIS/HCl, pH 6.8) was added, followed by incubation at 37°C on a shaker for 60 minutes. Next, 500 µl of digestion solution II (50 µg/ml trypsin in ddH2O) was added, with incubation for an additional 60 minutes under the same conditions. The enzymes were inactivated by heating at 100°C for 3 minutes, then the pellets were collected (5 min at 10,000 rpm). After washing with 2.5 ml of ddH2O, the pellets were resuspended in 2.5 ml of 1 M HCl and incubated for 4 hours at 37°C on a shaker. The samples were centrifuged and washed with ddH2O until the pH reached 5–6. Subsequently, the pellet was resuspended in 1.25 ml of digestion buffer (12.5 mM sodium dihydrogen phosphate, pH 5.5) to an OD578 of 3.0, and 1/10 volume of mutanolysin solution (5,000 U/ml of mutanolysin in ddH2O) was added. The

mixture was incubated for 16 hours at 37°C with shaking at 150 rpm. Mutanolysin was inactivated by boiling for 3 minutes at 100°C, followed by centrifugation, and the supernatant containing peptidoglycan was aliquoted into 10 tubes for further use.

2.4.21. Cells isolation and cytokine analysis

Psoriatic mouse skin was harvested after euthanasia and incubated at room temperature in a Dispase solution (5 mg/ml in DMEM/F12 medium) for 2 hours. The epidermis was then physically separated from the dermis and cultured on polycarbonate cell culture inserts (pore size 0.4 μm) with complete DMEM medium (4.5 g/L glucose, 10% fetal bovine serum (FBS), 2 mM Lglutamine, 100 units/mL penicillin G, 100 μg/mL streptomycin). Equally distribute 100 μL of the purified LTA or peptidoglycan solution on top of the isolated psoriatic epidermis and collect 0.5 mL culture medium in 24 hours for mouse cytokine profiling. The separated dermis was used for dendritic cell extraction. Briefly, the dermal tissues were digested in 1X triple enzyme digestion solution (0.1 g collagenase type IV (Sigma Cat. C5318), 2000 Units DNase Type IV (Sigma Cat. D5025), 10 mg Hyaluronidase Type V (Sigma Cat. H6254) in 100 mL HBSS without calcium or magnesium) at 37°C for 30 minutes to 1 hour. Filter through a 70 μm nylon mesh, spin down the dissociated cells and seed the resuspended cells in 5ml of density gradient medium Lymphoprep (StemCell Technologies Cat. 07801) to enrich mononuclear cell layers. The enriched fractions after being washed were used to extract plasmacytoid dendritic cell population with plasmacytoid dendritic cell enrichment kit (Miltenyi Biotec #130-107-093). Seed 105-6 of the extracted cells into 24-well plates with complete RPMI 1640 medium for culture. Add 50 μL of the purified LTA or peptidoglycan solution to the medium and collect 0.5 mL culture medium in 24 hours for mouse cytokine profiling.

2.4.22. Histology, immunohistochemistry, and immunofluorescence

For tissue histological analysis, Hematoxylin and eosin (H&E), and CD4, CD8, ki-67, CD31, CK14, F4/80 histological tissue sections were prepared and stained by the Human Tissue Resource Center at the University of Chicago. Anti-mouse CD4 (Sysy-HistoSure, Cat#HS-360-117, Clone: 78H9D2, rat IgG2b,

kappa light chain, 1:200 dilution), anti-mouse CD8 (eBioscince Affymetrix, Cat#14-0808-82, rat monoclonal antibody, Clone: 4SM15, rat IgG2a, kappa light chain, 1:800 dilution), anti-CD31 (abcam, Cat#ab28364, lot#GR3247742-25, Rabbit antibody, 1:450 dilution) for IF staining, anti-Ki67 (ThermoScientific, Cat#RM-9106-s, Clone: SP6, Rabbit monoclonal antibody, 1:400 dilution), and anti-mouse F4/80 antibody (AbD Serotec, Cat#MCA497GA, 1:200 dilution) were used for IHC staining. Anti-F4/80 (Biorad, #MCA497, rat IgG2b, 1:400 diliution) /Cytokeratin 14 (ProteinTech Group, #10143-1-AP, rabbit polyclonal antibody, 1:200 dilution) were used for dual IHC staining. All the tissue histological results were analyzed by the CaseViewer software (3DHISTECH) and QuPath (0.4.0). The histological damage, including hyperplasia, parakeratosis, neutrophil infiltration, loss of granular layer, dilated capillaries, dermal inflammation on a scale of 0–4 (from none to the maximum damage, was scored based on the H&E-stained skin tissue sections. The sum of all above values was the value of the histological damage score. The thickness of the epidermal layer and the counting of IHC positive cells were analyzed through ImageJ

2.4.23. Murine in-vivo 6- lead electrocardiogram (ECG) recording

The procedure was carried out on an adult mouse, including both healthy individuals and those exhibiting psoriasis on the chest. The subjects were deeply anesthetized using 2-4% isoflurane. A 6-lead living hydrogel-hybrid mesh electrode was adhered to a specific area covering the mouse's chest, strategically aligned to conform to the standard positions for frontal plane ECG leads (I, II, III, aVR, aVL, and aVF). The recording procedure employed an Intantech RHD USB interface board and an RHD 16- channel bipolar-input recording headstage. Signals were recorded at a rate of 20 kS s-1 , within the bandwidth range of 0.6 - 100 Hz.

2.4.24. Cytokine analysis

The Mouse Cytokine Array, Panel A (R&D Systems #ARY006) utilizes capture antibodies spotted onto a nitrocellulose membrane to allow high-throughput multi-analyte profiling of 40 cytokines, chemokines, and

more in a single sample. For cytokine assays, fresh skin psoriatic skin tissues were harvested and homogenized in cold RIPA buffer. Subsequently, 200 µg of lysate was used for each array by following the manufacturers' instructions. Array images were collected and analyzed using the Bio-rad Gel Doc XR+ Imaging System.

2.4.25. Flow cytometry

Psoriatic skin tissues were harvested after euthanasia and trimmed into small pieces of the similar weight for digestion in 1X triple enzyme digestion solution (0.1 g collagenase type IV (Sigma Cat. C5318), 2000 Units DNase Type IV (Sigma Cat. D5025), 10 mg Hyaluronidase Type V (Sigma Cat. H6254) in 100 mL HBSS without calcium or magnesium) at 37°C for 30 minutes to 1 hour. The mixture was filtered through a 70 µm nylon mesh, the dissociated cells were spun down, and the resuspended cells were seeded in a density gradient medium, Lymphoprep (StemCell Technologies Cat. 07801), to enrich mononuclear cell layers. The enriched fractions, after being washed, were co-stained with MitoView 405 (Biotium #70070, 100 nM) for living cell labeling and the antibody anti-mouse CD4-PE-vio615 (Miltenyi Biotec Cat. 130-118-455, 1:50 dilution). The stained samples were analyzed on the BD LSR Fortessa 4-15 benchtop analyzer at the UChicago flow cytometry core for immune cell population analysis. The output data were generated using NovoExpress software at the UChicago flow cytometry core.

2.4.26. Microbiome analysis

Three groups of mice (C57BL/6) were prepared for skin microbiome analysis: 1) The first group (Healthy) was healthy mice; 2) The second group (Control) was the mice with IMQ-induced psoriasis; 3) The third group was the mice with IMQ-induced psoriasis and treated with living bioelectronics for 4 days. Skin tissue samples from three different groups were collected and analyzed by the ZymoBIOMICS® Targeted 16S Sequencing Service (Zymo Research, Irvine, CA). DADA2 was used to infer unique amplicon sequence variants from raw reads.[38] Chimeric sequences and potential sequencing errors were removed using the DADA2 pipeline. We used Uclust from Qiime version 1.9.1, a 16S database designed and curated

as a reference, for taxonomy assignment. Linear discriminant analysis Effect Size (LEfSe) was used to identify taxonomies with significant abundance among different groups.[39] PCoA plots were performed using internal scripts. Quantitative real-time PCR was used to quantify the absolute abundance and the results were displayed as the number of gene copies.

2.4.27. Quantitative RT-PCR

SYBR Green real-time PCR was used to detect if the following bacterial strains existed in the posttreatment hydrogel: *S. epidermidis, Staphylococcus aureus, Delftia acidovorans, Microbacterium aerolatum, Rhodococcus erythropolis*. These strains were chosen because they were detected in the 16S rRNA sequencing results of the psoriatic skin samples in this study. The total RNA molecules in the hydrogel (pre- and post-treatment) were extracted using the Qiagen RNeasy Mini Kit (Cat. No. 74104). Quantitative RT-PCR was conducted using Takara's One-Step TB Green® PrimeScript™ RT-PCR Kit II (Perfect Real Time) (Cat. No. RR086A). Each reaction (20 μL) contained 200 ng of total RNA, 0.4 μM of primers, and 10 μL of 2x Master mix. Multiplex real-time PCR was performed on an ABI 7500 real-time PCR system (Applied Biosystems). A melting curve was added at the end of the PCR cycle to evaluate the specificity of the PCR amplification. The nucleotide sequences of 16S rRNAs of *S. epidermidis* (Se), Staphylococcus aureus (Sa), *Delftia acidovorans* (Da), *Microbacterium aerolatum* (Ma), *Rhodococcus erythropolis* (Re), were retrieved from the previous 16S rRNA sequencing results and used in the design of primer sequences, which were evaluated for specificity using the standard nucleotide comparison tool: BLASTN. Primer sequences: Se-u: TGGCACGGCTGGTATTAGAG Se-d: GACAGGATGCGCGATACTTG Sa-u: CAAGCACAAGGCAGTGGTAT Sa-d: GTGGCGTTGCAATCTCCTTA Da-u: AAAGCCTGATCCAGCAATGC Da-d: GATTAACGCTCGCACCCTAC Re-u: CGTTTGTGAAAACCAGCAGC Re-d: CTTTCGTTCCTCAGCGTCAG Ma-u: TAGCAGGGAAGAAGCGAGAG Ma-d: GTTGAGCCTCGGGATTTCAC

2.4.28. Statistical Analysis

The image data was processed and analyzed using ImageJ. GraphPad Prism 9.4.1 was employed for all statistical analyses. Unless stated otherwise, the error bars represent the standard deviation. For biological data analysis, multiple t-tests or one-way ANOVA were performed. A significance threshold of $P < 0.05$ was used to determine statistical significance. In transcriptome analysis, the P value is the Wald test p-value and Padj is the Benjamini-Hochberg adjusted p-value. In the figure panels, the following symbols were used to indicate significance levels: "ns" for non-significant ($P > 0.05$), "*" for $P < 0.05$, "**" for $P < 0.01$, "***" for $P < 0.001$, and "****" for $P < 0.0001$.

2.5. Bibliography

(1) Shi, J.; Kim, S.; Li, P.; Dong, F.; Yang, C.; Nam, B.; Han, C.; Eig, E.; Shi, L. L.; Niu, S.; Yue, J.; Tian, B. Active Biointegrated Living Electronics for Managing Inflammation. *Science (80-.).* **2024**, *384* (6699), 1023–1030. https://doi.org/10.1126/science.adl1102.

(2) Jiang, Y. Topological Supramolecular Network Enabled High-Conductivity, Stretchable Organic Bioelectronics. *Science (80-.).* **2022**, *375* (6587), 1411–1417. https://doi.org/10.1126/science.abn8347.

(3) Boys, A. J.; Carnicer-Lombarte, A.; Güemes-Gonzalez, A.; van Niekerk, D. C.; Hilton, S.; Barone, D. G.; Proctor, C. M.; Owens, R. M.; Malliaras, G. G. 3D Bioelectronics with a Remodellable Matrix for Long-Term Tissue Integration and Recording. *Adv. Mater.* **2023**, *35* (8). https://doi.org/10.1002/adma.202207847.

(4) Hu, H.; Huang, H.; Li, M.; Gao, X.; Yin, L.; Qi, R.; Wu, R. S.; Chen, X.; Ma, Y.; Shi, K.; Li, C.; Maus, T. M.; Huang, B.; Lu, C.; Lin, M.; Zhou, S.; Lou, Z.; Gu, Y.; Chen, Y.; Lei, Y.; Wang, X.; Wang, R.; Yue, W.; Yang, X.; Bian, Y.; Mu, J.; Park, G.; Xiang, S.; Cai, S.; Corey, P. W.; Wang, J.; Xu, S. A Wearable Cardiac Ultrasound Imager. *Nature* **2023**, *613* (7945), 667–675. https://doi.org/10.1038/s41586-022-05498-z.

(5) Liu, X.; Inda, M. E.; Lai, Y.; Lu, T. K.; Zhao, X. Engineered Living Hydrogels. *Adv. Mater.* **2022**, *34* (26), 2201326. https://doi.org/10.1002/adma.202201326.

(6) Inda-Webb, M. E.; Jimenez, M.; Liu, Q.; Phan, N. V.; Ahn, J.; Steiger, C.; Wentworth, A.; Riaz, A.; Zirtiloglu, T.; Wong, K.; Ishida, K.; Fabian, N.; Jenkins, J.; Kuosmanen, J.; Madani, W.; McNally, R.; Lai, Y.; Hayward, A.; Mimee, M.; Nadeau, P.; Chandrakasan, A. P.; Traverso, G.; Yazicigil, R. T.; Lu, T. K. Sub-1.4 Cm3 Capsule for Detecting Labile Inflammatory Biomarkers in Situ. *Nature* **2023**, *620* (7973), 386–392. https://doi.org/10.1038/s41586-023-06369-x.

(7) Jiang, X.; Feng, T.; An, B.; Ren, S.; Meng, J.; Li, K.; Liu, S.; Wu, H.; Zhang, H.; Zhong, C. A Bi-Layer Hydrogel Cardiac Patch Made of Recombinant Functional Proteins. *Adv. Mater.* **2022**, *34* (19), 1–11. https://doi.org/10.1002/adma.202201411.

(8) Ramadi, K. B.; McRae, J. C.; Selsing, G.; Su, A.; Fernandes, R.; Hickling, M.; Rios, B.; Babaee,

S.; Min, S.; Gwynne, D.; Jia, N. Z.; Aragon, A.; Ishida, K.; Kuosmanen, J.; Jenkins, J.; Hayward, A.; Kamrin, K.; Traverso, G. Bioinspired, Ingestible Electroceutical Capsules for Hunger-Regulating Hormone Modulation. *Sci. Robot.* **2023**, *8* (77), 1–13. https://doi.org/10.1126/SCIROBOTICS.ADE9676.

(9) Nan, K.; Feig, V. R.; Ying, B.; Howarth, J. G.; Kang, Z.; Yang, Y.; Traverso, G. Mucosa-Interfacing Electronics. *Nat. Rev. Mater.* **2022**, *7* (11), 908–925. https://doi.org/10.1038/s41578-022-00477-2.

(10) Terrell, J. L.; Tschirhart, T.; Jahnke, J. P.; Stephens, K.; Liu, Y.; Dong, H.; Hurley, M. M.; Pozo, M.; McKay, R.; Tsao, C. Y.; Wu, H. C.; Vora, G.; Payne, G. F.; Stratis-Cullum, D. N.; Bentley, W. E. Bioelectronic Control of a Microbial Community Using Surface-Assembled Electrogenetic Cells to Route Signals. *Nat. Nanotechnol.* **2021**, *16* (6), 688–697. https://doi.org/10.1038/s41565-021-00878-4.

(11) Wang, M.; Yang, Y.; Min, J.; Song, Y.; Tu, J.; Mukasa, D.; Ye, C.; Xu, C.; Heflin, N.; McCune, J. S.; Hsiai, T. K.; Li, Z.; Gao, W. A Wearable Electrochemical Biosensor for the Monitoring of Metabolites and Nutrients. *Nat. Biomed. Eng.* **2022**, *6* (11), 1225–1235. https://doi.org/10.1038/s41551-022-00916-z.

(12) Cheng, W.; Wang, X.; Xiong, Z.; Liu, J.; Liu, Z.; Jin, Y.; Yao, H.; Wong, T. S.; Ho, J. S.; Tee, B. C. K. Frictionless Multiphasic Interface for Near-Ideal Aero-Elastic Pressure Sensing. *Nat. Mater.* **2023**, *22* (11), 1352–1360. https://doi.org/10.1038/s41563-023-01628-8.

(13) Jiang, Y.; Ji, S.; Sun, J.; Huang, J.; Li, Y.; Zou, G.; Salim, T.; Wang, C.; Li, W.; Jin, H.; Xu, J.; Wang, S.; Lei, T.; Yan, X.; Peh, W. Y. X.; Yen, S. C.; Liu, Z.; Yu, M.; Zhao, H.; Lu, Z.; Li, G.; Gao, H.; Liu, Z.; Bao, Z.; Chen, X. A Universal Interface for Plug-and-Play Assembly of Stretchable Devices. *Nature* **2023**, *614* (7948), 456–462. https://doi.org/10.1038/s41586-022-05579-z.

(14) Guan, Y. S.; Ershad, F.; Rao, Z.; Ke, Z.; da Costa, E. C.; Xiang, Q.; Lu, Y.; Wang, X.; Mei, J.; Vanderslice, P.; Hochman-Mendez, C.; Yu, C. Elastic Electronics Based on Micromesh-Structured Rubbery Semiconductor Films. *Nat. Electron.* **2022**, *5* (12), 881–892. https://doi.org/10.1038/s41928-022-00874-z.

(15) Song, E.; Xie, Z.; Bai, W.; Luan, H.; Ji, B.; Ning, X.; Xia, Y.; Baek, J. M.; Lee, Y.; Avila, R.; Chen, H. Y.; Kim, J. H.; Madhvapathy, S.; Yao, K.; Li, D.; Zhou, J.; Han, M.; Won, S. M.; Zhang, X.; Myers, D. J.; Mei, Y.; Guo, X.; Xu, S.; Chang, J. K.; Yu, X.; Huang, Y.; Rogers, J. A. Miniaturized Electromechanical Devices for the Characterization of the Biomechanics of Deep Tissue. *Nat. Biomed. Eng.* **2021**, *5* (7), 759–771. https://doi.org/10.1038/s41551-021-00723-y.

(16) Gao, Y.; Nguyen, D. T.; Yeo, T.; Lim, S. Bin; Tan, W. X.; Madden, L. E.; Jin, L.; Kenan Long, J. Y.; Bakar Aloweni, F. A.; Angela Liew, Y. J.; Ling Tan, M. L.; Ang, S. Y.; Maniya, S. D. O.; Abdelwahab, I.; Loh, K. P.; Chen, C. H.; Becker, D. L.; Leavesley, D.; Ho, J. S.; Lim, C. T. A Flexible Multiplexed Immunosensor for Point-of-Care in Situ Wound Monitoring. *Sci. Adv.* **2021**, *7* (21), 1–16. https://doi.org/10.1126/sciadv.abg9614.

(17) Ouyang, W.; Lu, W.; Zhang, Y.; Liu, Y.; Kim, J. U.; Shen, H.; Wu, Y.; Luan, H.; Kilner, K.; Lee, S. P.; Lu, Y.; Yang, Y.; Wang, J.; Yu, Y.; Wegener, A. J.; Moreno, J. A.; Xie, Z.; Wu, Y.; Won, S. M.; Kwon, K.; Wu, C.; Bai, W.; Guo, H.; li Liu, T.; Bai, H.; Monti, G.; Zhu, J.; Madhvapathy, S. R.; Trueb, J.; Stanslaski, M.; Higbee-Dempsey, E. M.; Stepien, I.; Ghoreishi-Haack, N.; Haney, C. R.; il Kim, T.; Huang, Y.; Ghaffari, R.; Banks, A. R.; Jhou, T. C.; Good, C. H.; Rogers, J. A. A Wireless and Battery-Less Implant for Multimodal Closed-Loop Neuromodulation in Small Animals. *Nat. Biomed. Eng.* **2023**. https://doi.org/10.1038/s41551-023-01029-x.

(18) Park, J.; Jin, K.; Sahasrabudhe, A.; Chiang, P. H.; Maalouf, J. H.; Koehler, F.; Rosenfeld, D.; Rao, S.; Tanaka, T.; Khudiyev, T.; Schiffer, Z. J.; Fink, Y.; Yizhar, O.; Manthiram, K.; Anikeeva, P. In Situ Electrochemical Generation of Nitric Oxide for Neuronal Modulation. *Nat. Nanotechnol.* **2020**, *15* (8), 690–697. https://doi.org/10.1038/s41565-020-0701-x.

(19) Wang, C.; Chen, X. C.; Wang, L.; Makihata, M.; Liu, H.-C. L.; Zhou, T.; Zhao, X. Bioadhesive Ultrasound for Long-Term Continuous Imaging of Diverse Organs. *Science (80-.).* **2022**, *377* (6605), 517–523. https://doi.org/10.1126/science.abm6222.

(20) Zhou, T.; Yuk, H.; Hu, F.; Wu, J.; Tian, F.; Roh, H.; Shen, Z.; Gu, G.; Xu, J.; Lu, B.; Zhao, X. 3D Printable High-Performance Conducting Polymer Hydrogel for All-Hydrogel Bioelectronic Interfaces. *Nat. Mater.* **2023**, *22* (7), 895–902. https://doi.org/10.1038/s41563-023-01569-2.

(21) Yang, Q.; Wei, T.; Yin, R. T.; Wu, M.; Xu, Y.; Koo, J.; Choi, Y. S.; Xie, Z.; Chen, S. W.; Kandela, I.; Yao, S.; Deng, Y.; Avila, R.; Liu, T. L.; Bai, W.; Yang, Y.; Han, M.; Zhang, Q.; Haney, C. R.; Benjamin Lee, K.; Aras, K.; Wang, T.; Seo, M. H.; Luan, H.; Lee, S. M.; Brikha, A.; Ghoreishi-Haack, N.; Tran, L.; Stepien, I.; Aird, F.; Waters, E. A.; Yu, X.; Banks, A.; Trachiotis, G. D.; Torkelson, J. M.; Huang, Y.; Kozorovitskiy, Y.; Efimov, I. R.; Rogers, J. A. Photocurable Bioresorbable Adhesives as Functional Interfaces between Flexible Bioelectronic Devices and Soft Biological Tissues. *Nat. Mater.* **2021**, *20* (11), 1559–1570. https://doi.org/10.1038/s41563-021-01051-x.

(22) Deng, J.; Yuk, H.; Wu, J.; Varela, C. E.; Chen, X.; Roche, E. T.; Guo, C. F.; Zhao, X. Electrical Bioadhesive Interface for Bioelectronics. *Nat. Mater.* **2021**, *20* (2), 229–236. https://doi.org/10.1038/s41563-020-00814-2.

(23) Rochford, A. E.; Carnicer-Lombarte, A.; Kawan, M.; Jin, A.; Hilton, S.; Curto, V. F.; Rutz, A. L.; Moreau, T.; Kotter, M. R. N.; Malliaras, G. G.; Barone, D. G. Functional Neurological Restoration of Amputated Peripheral Nerve Using Biohybrid Regenerative Bioelectronics. *Sci. Adv.* **2023**, *9* (12), 1–10. https://doi.org/10.1126/sciadv.add8162.

(24) Lim, C.; Hong, Y. J.; Jung, J.; Shin, Y.; Sunwoo, S. H.; Baik, S.; Park, O. K.; Choi, S. H.; Hyeon, T.; Kim, J. H.; Lee, S.; Kim, D. H. Tissue-like Skin-Device Interface for Wearable Bioelectronics by Using Ultrasoft, Mass-Permeable, and Low-Impedance Hydrogels. *Sci. Adv.* **2021**, *7* (19), 1–11. https://doi.org/10.1126/sciadv.abd3716.

(25) Karin, M.; Clevers, H. Reparative Inflammation Takes Charge of Tissue Regeneration. *Nature* **2016**, *529* (7586), 307–315. https://doi.org/10.1038/nature17039.

(26) Tang, T. C.; An, B.; Huang, Y.; Vasikaran, S.; Wang, Y.; Jiang, X.; Lu, T. K.; Zhong, C. Materials Design by Synthetic Biology. *Nat. Rev. Mater.* **2021**, *6* (4), 332–350. https://doi.org/10.1038/s41578-020-00265-w.

(27) Rodrigo-Navarro, A.; Sankaran, S.; Dalby, M. J.; del Campo, A.; Salmeron-Sanchez, M. Engineered Living Biomaterials. *Nat. Rev. Mater.* **2021**, *6* (12), 1175–1190. https://doi.org/10.1038/s41578-021-00350-8.

(28) Severn, M. M.; Horswill, A. R. Staphylococcus Epidermidis and Its Dual Lifestyle in Skin Health and Infection. *Nat. Rev. Microbiol.* **2023**, *21* (2), 97–111. https://doi.org/10.1038/s41579-022-00780-3.

(29) Sauer, K.; Stoodley, P.; Goeres, D. M.; Hall-Stoodley, L.; Burmølle, M.; Stewart, P. S.; Bjarnsholt, T. The Biofilm Life Cycle: Expanding the Conceptual Model of Biofilm Formation. *Nat. Rev. Microbiol.* **2022**, *20* (10), 608–620. https://doi.org/10.1038/s41579-022-00767-0.

(30) Baumgartner, M.; Hartmann, F.; Drack, M.; Preninger, D.; Wirthl, D.; Gerstmayr, R.; Lehner, L.; Mao, G.; Pruckner, R.; Demchyshyn, S.; Reiter, L.; Strobel, M.; Stockinger, T.; Schiller, D.; Kimeswenger, S.; Greibich, F.; Buchberger, G.; Bradt, E.; Hild, S.; Bauer, S.; Kaltenbrunner, M. Resilient yet Entirely Degradable Gelatin-Based Biogels for Soft Robots and Electronics. *Nat. Mater.* **2020**, *19* (10), 1102–1109. https://doi.org/10.1038/s41563-020-0699-3.

(31) Greb, J. E.; Goldminz, A. M.; Elder, J. T.; Lebwohl, M. G.; Gladman, D. D.; Wu, J. J.; Mehta, N. N.; Finlay, A. Y.; Gottlieb, A. B. Psoriasis. *Nat. Rev. Dis. Prim.* **2016**, *2*. https://doi.org/10.1038/nrdp.2016.82.

(32) Liang, H.; Yan, Y.; Wu, J.; Ge, X.; Wei, L.; Liu, L.; Chen, Y. Topical Nanoparticles Interfering with the DNA-LL37 Complex to Alleviate Psoriatic Inflammation in Mice and Monkeys. *Sci. Adv.* **2020**, *6* (31), 1–14. https://doi.org/10.1126/sciadv.abb5274.

(33) Bracho-Sanchez, E.; Rocha, F. G.; Bedingfield, S. K.; Partain, B. D.; Macias, S. L.; Brusko, M. A.; Colazo, J. M.; Fettis, M. M.; Farhadi, S. A.; Helm, E. Y.; Koenders, K.; Kwiatkowski, A. J.; Restuccia, A.; Morales, B. S.; Wanchoo, A.; Avram, D.; Allen, K. D.; Duvall, C. L.; Wallet, S. M.; Hudalla, G. A.; Keselowsky, B. G. Suppression of Local Inflammation via Galectin-Anchored Indoleamine 2,3-Dioxygenase. *Nat. Biomed. Eng.* **2023**, *7* (9), 1156–1169. https://doi.org/10.1038/s41551-023-01025-1.

(34) Yuanwen Jiang; Trotsyuk, A. A.; Niu, S.; Henn, D.; Chen, K.; Shih, C.-C.; Larson, M. R.; Mermin-Bunnell, A. M.; Mittal, S.; Lai, J.-C.; Saberi, A.; Beard, E.; Jing, S.; Zhong, D.; Steele, S. R.; Sun, K.; Jain, T.; Zhao, E.; Neimeth, C. R.; Viana, W. G.; Tang, J.; Sivaraj, D.; Padmanabhan, J.; Rodrigues, M.; Perrault, D. P.; Chattopadhyay, A.; Maan, Z. N.; Leeolou, M. C.; Bonham, C. A.; Hyung Kwon, S.; Kussie, H. C.; Fischer, K. S.; Gurusankar, G.; Liang, K.; Zhang, K.; Nag, R.; Snyder, M. P.; Januszyk, M.; Gurtner, G. C.; Bao, Z. Wireless Closed-Loop Smart Bandage for Chronic Wound Management and Accelerated Tissue Regeneration. *bioRxiv* **2022**, 2022.01.16.476432.

(35) Linehan, J. L.; Harrison, O. J.; Han, S. J.; Byrd, A. L.; Vujkovic-Cvijin, I.; Villarino, A. V.; Sen, S. K.; Shaik, J.; Smelkinson, M.; Tamoutounour, S.; Collins, N.; Bouladoux, N.; Dzutsev, A.; Rosshart, S. P.; Arbuckle, J. H.; Wang, C. R.; Kristie, T. M.; Rehermann, B.; Trinchieri, G.; Brenchley, J. M.; O'Shea, J. J.; Belkaid, Y. Non-Classical Immunity Controls Microbiota Impact on Skin Immunity and Tissue Repair. *Cell* **2018**, *172* (4), 784-796.e18. https://doi.org/10.1016/j.cell.2017.12.033.

(36) Terui, H.; Yamasaki, K.; Wada-Irimada, M.; Onodera-Amagai, M.; Hatchome, N.; Mizuashi, M.; Yamashita, R.; Kawabe, T.; Ishii, N.; Abe, T.; Asano, Y.; Aiba, S. Staphylococcus Aureus Skin Colonization Promotes SLE-like Autoimmune Inflammation via Neutrophil Activation and the IL-23/IL-17 Axis. *Sci. Immunol.* **2022**, *7* (76), 1–19. https://doi.org/10.1126/sciimmunol.abm9811.

(37) Byrd, A. L.; Belkaid, Y.; Segre, J. A. The Human Skin Microbiome. *Nat. Rev. Microbiol.* **2018**, *16* (3), 143–155. https://doi.org/10.1038/nrmicro.2017.157.

(38) Callahan, B. J.; McMurdie, P. J.; Rosen, M. J.; Han, A. W.; Johnson, A. J. A.; Holmes, S. P. DADA2: High-Resolution Sample Inference from Illumina Amplicon Data. *Nat. Methods* **2016**, *13* (7), 581–583. https://doi.org/10.1038/nmeth.3869.

(39) Segata, N.; Izard, J.; Waldron, L.; Gevers, D.; Miropolsky, L.; Garrett, W. S.; Huttenhower, C. Metagenomic Biomarker Discovery and Explanation. *Genome Biol.* **2011**, *12* (R60).

Chapter 3. Bioelectronic drug-free control of opportunistic pathogens through selective excitability

*Chapter 3 adopts figures and text from ref (1): **Kim, S.;** Eig, E.; Yue, J.; Yang, A.; Comerci, C. J.; Laune, M.; Yang, C.; Kamath, A.; Shi, J.; Li, P.; Cheng, Z.; Sun, C.; Guo, T.; Tian, V.; Süel, G. M.; Tian, B. Bioelectronic Drug-Free Control of Opportunistic Pathogens through Selective Excitability. *Device* **2024**, *2* (11), 100596.

3.1 Introduction

3.1.1 Bioelectrical interface targeting mammalian system

Leveraging the innsate electrical excitability of eukaryotic cells has enabled bioelectrical modes of tissue modulation, providing alternatives to drug-based therapies. Excellent examples are electroceuticals, therapeutic bioelectronic devices that stimulate the body's naturally excitable circuits.[2] Bioelectronic devices such as cardiac pacemakers,[3,4] retinal prostheses,[5,6] and nerves stimulators[7] demonstrate how understanding and harnessing natural excitability in tissues can bring extensive health benefits. In these devices, well-known excitable cells such as neurons have been the main target of modulation.[8,9] However, the recent discovery of innate electrical excitability in microbes suggests a potential for the bioelectrical control of commensal bacteria that are crucial to human health.[10] To target bacteria inhabiting the human body, it would be preferable to use low-voltage stimulation to modulate bacterial physiology and pathology similarly to how electroceuticals are used in human medicine.

3.1.2 Bioelectrical interface targeting microbial system

There is a need to effectively control the bacteria residing on the human body, as many of them can become opportunistic pathogens under certain conditions.[11] For example, *Staphylococcus epidermidis*, commonly found on healthy skin, typically promotes tissue homeostasis and aids in wound healing.[12] However, factors such as compromised skin barrier, immunosuppression, and biofilm formation can shift its behavior toward pathogenicity.[13,14] In the virulent state, *S. epidermidis* is a significant contributor to neonatal morbidity[15] and is the second-leading cause of hospital infections due to the formation of antibiotic-resistant biofilm in clinical implants.[16] Moreover, the severity of dermatological

disorders like atopic dermatitis[17] and scalp seborrheic dermatitis (i.e., dandruff)[18] is linked to an over-proliferation of *S. epidermidis* on the skin. Effective management of opportunistic pathogens is a major challenge that, if overcome, could have far-reaching implications.

Bioelectronic control of opportunistic pathogens may offer unique advantages over antibiotic treatments. Antibiotics carry widespread side effects, such as nausea, drug fever, and nephrotoxicity.[19] Repeated exposure to antibiotics increases the risk factor for chronic inflammatory disorders[20] and contributes to antimicrobial resistance, a global health threat.[21,22] Recently, three strains of *S. epidermidis* that are pan-resistant to all classes of antibiotics have emerged,[23] exposing the fragility of drug-based methods. Unlike drugs, bioelectrical treatments may allow for localized and targeted therapy, thereby minimizing systemic side effects.[24] Bioelectronic methods may also be applied automatically with programmable stimulation parameters that can be optimized for individual patients to enable personalized medication.[25,26]

Despite being a potential drug-free alternative, existing electrical treatment for bacteria is less developed compared to those acting on mammalian systems, as bacterial electrophysiology is still being elucidated. Conventional electrical treatment for bacteria has primarily focused on the electrostatic surface detachment of cells, high-voltage electroporation, and electrochemical biocide generation that irreversibly kills bacteria.[27–29] This contrasts with electroceuticals targeting mammalian tissues that leverage innate cellular excitability to elicit non-lethal and programmable bioelectrical responses.[30] Given that bioelectrical potential is closely related to growth, virulence, and antibiotic resistance in bacteria,[31] bioelectronic devices that exploit excitatory responses in opportunistic pathogens could offer a powerful handle to steer bacterial physiology in our favor (**Figure 3-1A**).

3.1.3 Exploring Excitable Microbial Biointerface

Several gaps in knowledge must be filled to engineer devices that can exploit excitatory responses in opportunistic pathogens. Among the human microbiota, only two species have been conclusively shown

to be electrically excitable, demonstrating the ability to generate changes in membrane potential in response to electrical stimulation.[32] Specifically, *Escherichia coli* and *Bacillus subtilis*, which reside in the gastrointestinal tract, exhibit changes in membrane potential when electrically stimulated.[33] This number of reported electrically excitable species is remarkably small compared to the thousands of bacterial species that reside in our bodies.[34] Consequently, molecular mechanisms underlying bacterial electrophysiology have only been elucidated for a few model organisms such as *B. subtilis*,[35,36]and far less is known about more medically relevant species. Furthermore, the long-term effects and the clinical relevance of excitatory responses in opportunistic pathogens remain unclear.[32,37] This gap in understanding has impeded the development of wearable or implantable bioelectronics designed to control resident bacteria by harnessing their innate electrical excitability.

In this study, we engineered a microelectronic platform to examine the electrical excitability of the skin-residing opportunistic pathogen *S. epidermidis*. Our findings show that *S. epidermidis* can be excited by a non-lethal electrical stimulus, causing reversible changes in membrane potential. Intriguingly, *S. epidermidis* and other skin pathogens were excitable only when subjected to an acidic epidermal pH. Hence, we have coined the term "selective excitability" to describe excitatory behavior that occurs only under select conditions, such as in this case, the epidermal pH. The bioelectrical stimulation inhibited growth, virulence gene expression, and biofilm formation in *S. epidermidis*. Leveraging these findings, we developed an electroceutical patch that exploits selective excitability of *S. epidermidis*, preventing skin colonization using a voltage that is safe and imperceptible to humans. Our research highlights the discovery and utilization of selective excitability in bacteria, enabling drug-free bioelectronic control of opportunistic pathogens.

3.2 Results and Discussions

3.2.1. A tailored device platform enables the assessment of bacterial excitability in response to electrical stimulation

To observe the effects of electrical stimulation at single-cell resolution, we developed a customized setup for bacterial electrophysiology. Interdigitated gold electrodes were fabricated on a 0.17-mm glass coverslip, compatible with the use of 63× and 100× microscope objectives that have a short working distance (**Figure 3-1B and Figure 3-1C**). Interdigitated designs enable electric potential localization between adjacent fingers for effective cell modulation,[38,39] while gold provides superior biocompatibility.[40] After inoculating the bacteria on agarose pads, these were placed on the electrode surface, and a potentiostat was used to deliver an alternating current (AC) at specified frequencies and voltages. The electrodes were designed with a width and gap of 40 μm (**Figure 3-1D**), suitable for the small size of *S. epidermidis*, which ranges from approximately 1 to 2 μm.[41] Incorporating a 2 × 2 grid within a single device enabled us to perform parallel experiments with varying conditions, facilitating statistical analysis. The customized setup allowed us to deliver exogenous electrical stimuli and monitor electrophysiological changes in bacteria through fluorescence and phase-contrast microscopy (**Figure 3-1E).**

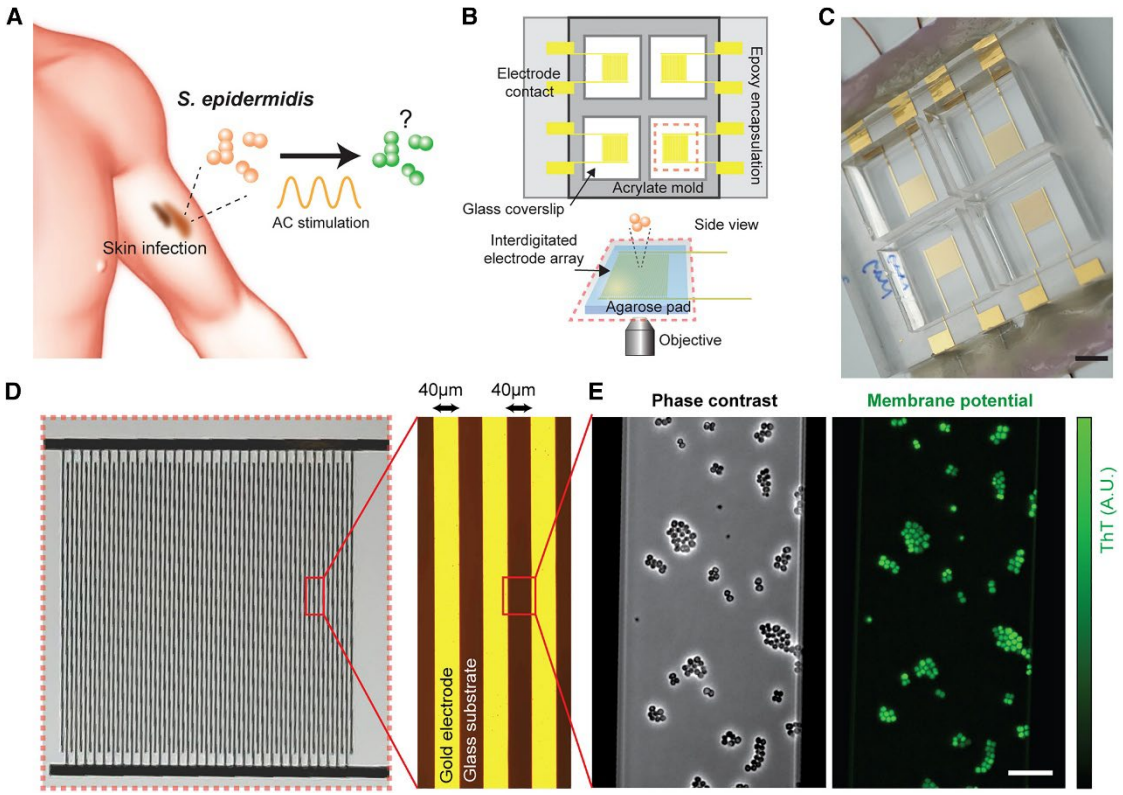

Figure 3-1. An interdigitated stimulation platform enables the assessment of bacterial excitability in response to electrical stimulation. A. Opportunistic infections by *S. epidermidis* serve as a leading source of healthcare-associated infections. We investigate whether we can induce an excitatory response in *S. epidermidis* through electrical stimulation, enabling drug-free, bioelectrical modulation. **B**. Schematics of the electrical simulation device used to study the excitability of *S. epidermidis*. **C**. The electrical stimulation device. Scale bar, 5 mm. **D**. Magnified image of interdigitated gold microelectrodes. **E**. Phase contrast (left) and fluorescence image of ThT-stained *S. epidermidis* (right) located between the interdigitated gold electrode array. ThT reports on the membrane potential. The color bar illustrates the intensity range of ThT-stained cells. Scale bar, 10 µm.

3.2.2 Epidermal pH confers electrical excitability to *S. epidermidis*

Skin-residing bacteria are exposed to diverse pH conditions, with healthy skin typically ranging from 4.7 to 5.2[42] and skin with atopic dermatitis from 5.5 to 5.9.[43] Acne vulgaris presents a skin pH of around 6.4,[44] whereas chronic wounds have pH varying from 7.2 to 8.9.[45] Considering the varied

environmental pH levels to which the bacteria are subjected, we explored the electrical excitability of *S. epidermidis* across external pH (pH_e) ranges of 4–9. The electrical stimulation condition (75 millivolts peak-to- peak [mVpp]/µm, AC, 0.1 kHz for 10 s) was selected based on the work on *B. subtilis* stimulation by Stratford et al.[33] and optimization processes outlined in **Figure 3-2**.

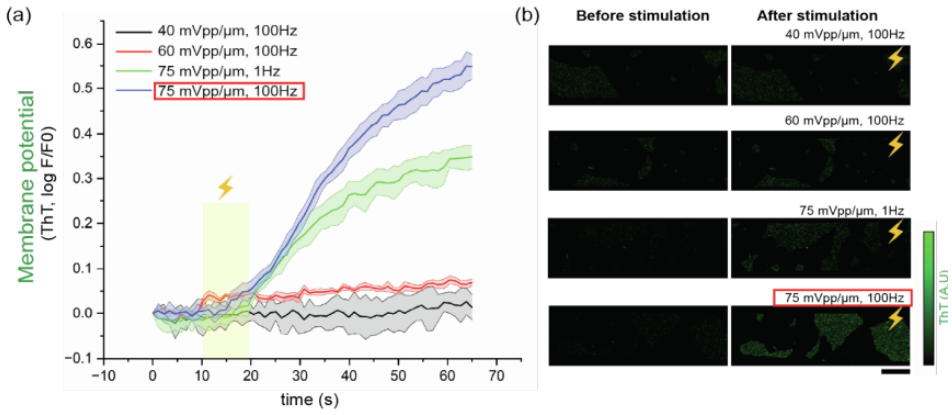

Figure 3-2 Optimization of electrical stimulation conditions. A. ThT intensity trace of electrically stimulated *S. epidermidis* at pH 5 (n=4). **B**. Fluorescence image of ThT stained *S. epidermidis* before and after stimulation. Scale bar, 20 µm. Excitatory response was not observed at 40mVpp/µm. Increasing the field strength to 60mVpp/µm resulted in subtle membrane potential change. 75mVpp/µm elicited the most measurable response. Field strength was not increased further to prevent potential damages to the electrode. While the frequency of 1Hz elicited changes in membrane potential, the response was weaker than at 100Hz. Altogether, 75mVpp/µm at 0.1kHz AC was selected as the stimulation condition. This condition strongly aligns with the parameters used in Stratford, J. P. et al. pioneering work on B. subtilis stimulation.3 All data are presented as mean values ± SD

Electrical stimulation increased the fluorescence intensity of the membrane potential indicator thioflavin T (ThT) in cells, indicative of hyperpolarization. However, this response was observed only at pH_e = 5, matching the pH of healthy skin (**Figure 3-3A-C**).[46] Hyperpolarization of *S. epidermidis* upon electrical stimulation was confirmed with another membrane potential indicator, tetramethylrhodamine (**Figure 3-4**). We also studied changes in the bacteria's intracellular pH using pHrodo staining. Electrical

stimulation increased pHrodo fluorescence, suggesting cytoplasmic acidification. Like the membrane potential, the change was observed only at $pH_e = 5$ (**Figure 3-3D-F**).

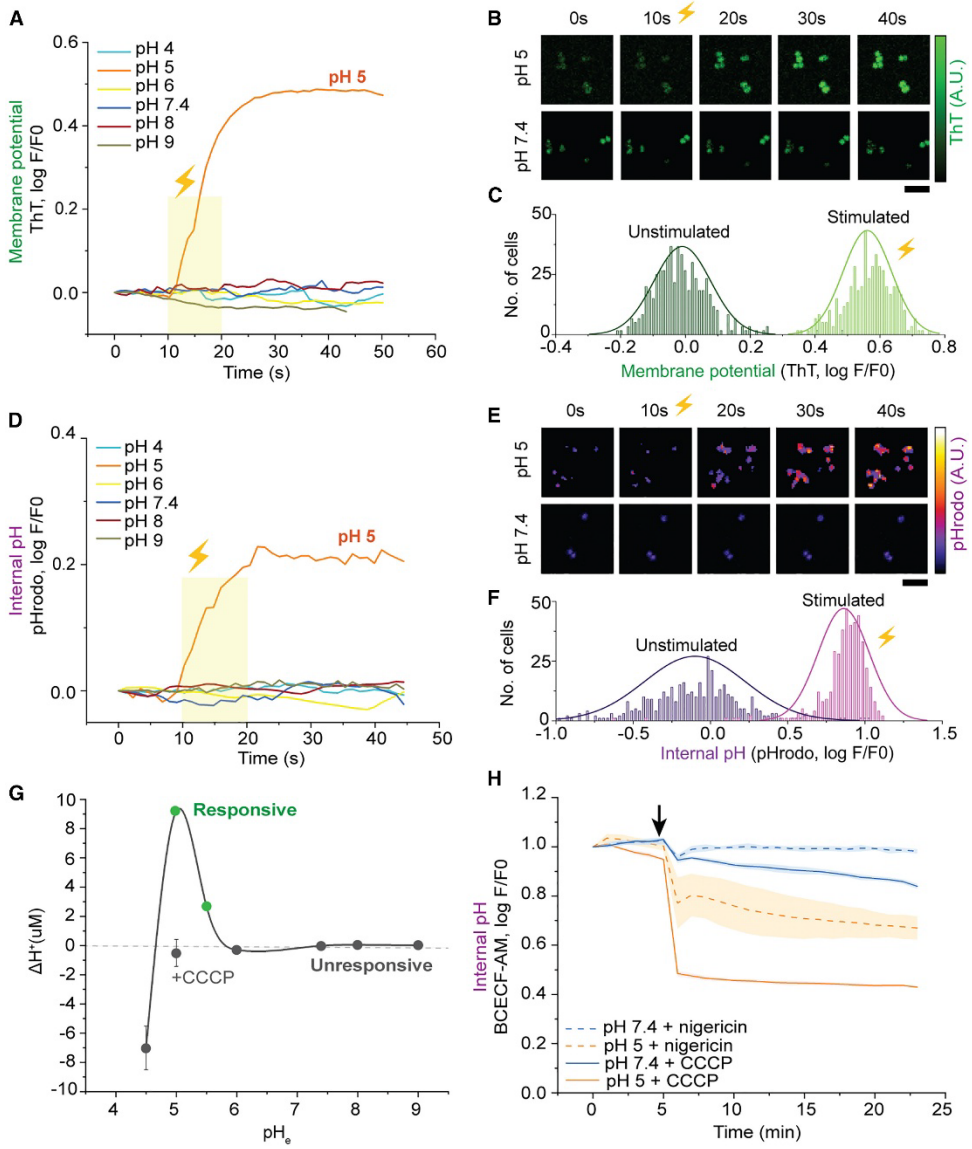

Figure 3-3. Epidermal pH confers electrical excitability to *S. epidermidis*. **A**. ThT intensity traces show that electrical stimulation hyperpolarizes *S. epidermidis* only at $pH_e = 5$. Fluorescence intensity is calculated as log(F/F0), where F is the fluorescence and F0 is the fluorescence at the resting state. **B**. Confocal images show that electrical stimulation elicits hyperpolarization at $pH_e = 5$, but not at $pH_e = 7.4$.

The pH of 7.4 represents the unmodified pH of TSB medium, where the bacteria grow most optimally. Scale bar, 5 µm. The color bar illustrates the intensity range of ThT-stained cells. **C**. Intensity histogram of ThT-stained cells at rest and post-stimulation at $pH_e = 5$ ($n \geq 300$). **D**. pHrodo intensity traces show that electrical stimulation acidifies the cytoplasm of *S. epidermidis* only at $pH_e = 5$. pHrodo reports on the internal pH, with its fluorescence increasing at a lower internal pH. **E**. Confocal images show that electrical stimulation induces acidification of cytoplasm at $pH_e = 5$, but not at $pH_e = 7.4$. Scale bar, 5 µm. The color bar illustrates the intensity range of pHrodo-stained cells. **F**. Intensity histogram of pHrodo-stained cells at rest and post-stimulation at $pH_e = 5$ ($n \geq 300$). **G.** The maximum of transmembrane proton gradient, ΔH^+, exists near $pH_e = 5$, which could be abolished by the addition of 150 µM CCCP ($n = 4$). Experimentally, cells are electrically excitable (green) only near the epidermal pH, where substantial ΔH^+ is present. **H.** Upon addition of CCCP (150 µM) and nigericin (3 µM), *S. epidermidis* shows greater cytoplasmic acidification at $pH_e = 5$ compared to $pH_e = 7.4$. BCECF-AM reports on internal pH, with its fluorescence decreasing at a lower internal pH. The black arrow denotes the point of addition ($n = 4$). All data are presented as means ±SDs.

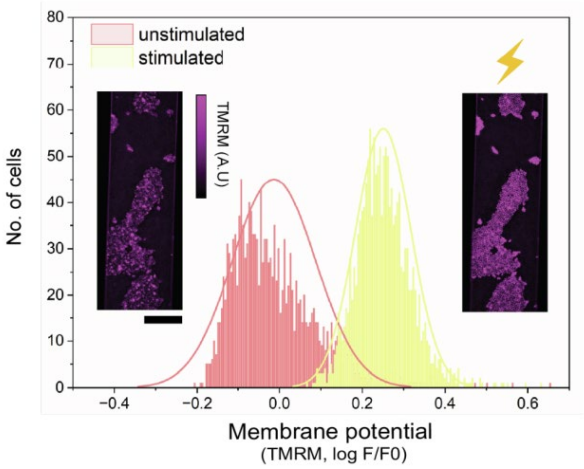

Figure 3-4. Electrical stimulation at pH 5 causes a hyperpolarization of *S. epidermidis*, shown by tetramethylrhodamine (TMRM) staining. *S. epidermidis* was stained with the TMRM membrane voltage

indicator (200nM) which shows increase in fluorescence after electrical stimulation, indicating hyperpolarization (n>1000). Scale bar, 20µm.

An acidic epidermal pH, used as the skin's first line of defense against microbes, presents an adverse environment for bacterial growth.[47] Surprisingly, *S. epidermidis* exhibited electrical excitability at the epidermal pH of 5, but remained completely unresponsive to stimulation at its optimal growth condition at pH 7.4 (**Figure 3-5**). We coined the term "Selective excitability" to describe how the bacteria became excitable only when select conditions, deviating from the best thriving environment, were met.

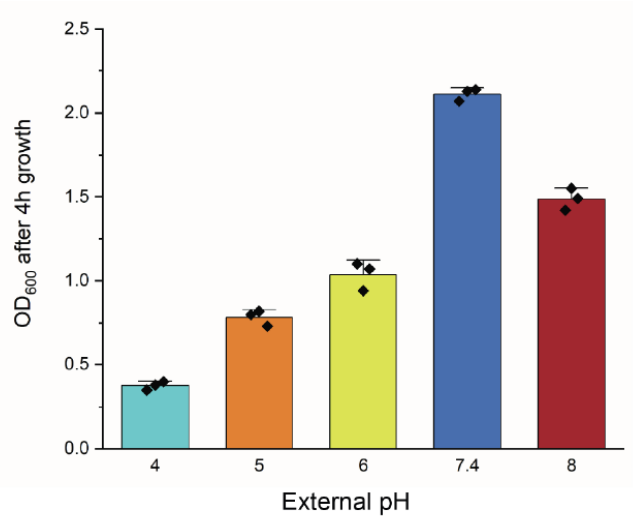

Figure 3-5. *S. epidermidis* grows optimally at pH 7.4. The optical density of *S. epidermidis* was adjusted to OD600=0.27 in TSB medium and incubated for 4 hours at 37°C in a shaker incubator before taking the final OD600 measurements. The results indicate that pH 5 is an unfavourable pH for bacterial growth. *S. epidermidis* grows most optimally at pH 7.4, which is the unmodified pH of the TSB medium used for routine bacterial culture (n=3). All data are presented as mean values ± SD.

Next, several control experiments were conducted to demonstrate the reversibility and non-lethality of the excitation response. Changes in membrane potential and intracellular pH were not due to cell death or electroporation (**Figure 3-6**), as the proportion of propidium iodide-stained cells remained unchanged upon stimulation. Indeed, the electric field we applied (75 mVpp/µm) was about two orders of magnitude

lower than the lethal electroporation threshold for *S. epidermidis* reported in the literature, which ranges from 1,000–3,500 mV/μm.[48] The electric field was generated with an AC voltage (V_{ac}) of 1.5 V_{ac}, which is considered safe and imperceptible to humans.[49] Importantly, the hyperpolarized membrane potential could be reversed back to the resting state within a 6-h time frame, during which the bacteria resumed growth (**Figure 3-7**). This shows the reversibility and non-lethal nature of the bioelectrical response.

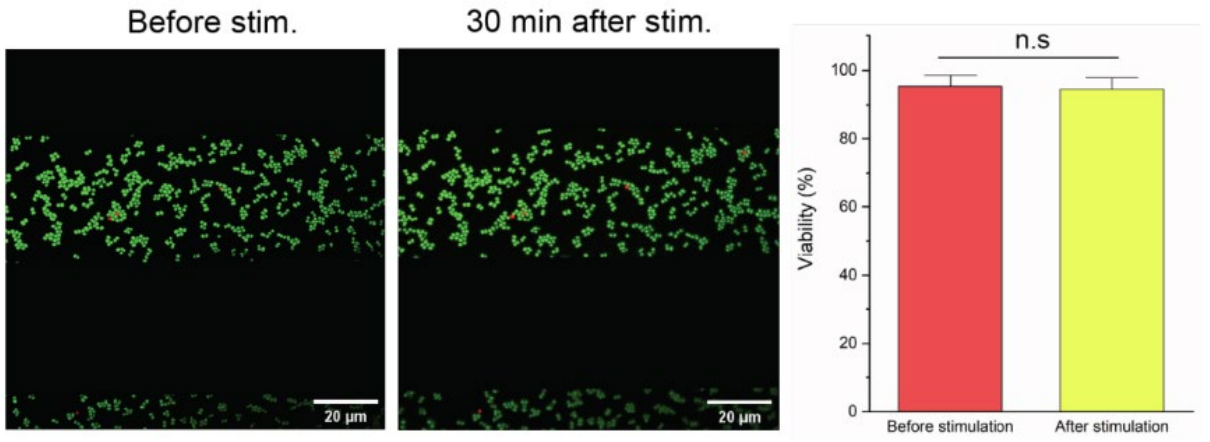

Figure 3-6. The electrical stimulation does not permeabilize the bacterial membrane. Live cells are stained with SYTO9 (green), while dead cells with a compromised membrane are stained with propidium iodide (PI, red). No significant decrease in viability was observed 30 minutes after an electrical stimulation (n=3). All data are presented as mean values ± SD.

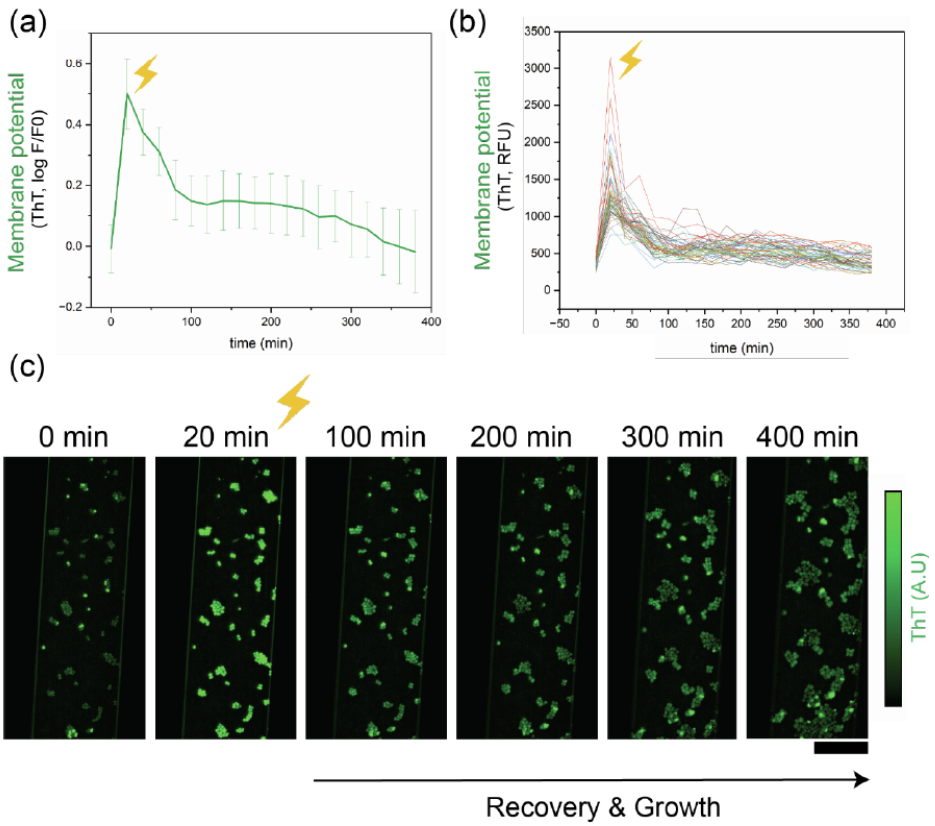

Figure 3-7. ThT intensity trace of electrically stimulated *S. epidermidis* at pH 5 shows recovery of membrane potential and growth. A. Mean intensity trace of ThT-stained *S. epidermidis*. The electrical stimulation was applied at the 20 minutes timepoint, reflected by the initial increase in ThT fluorescence intensity (n=50). **B**. Single-cell ThT intensity traces (n=50). **C.** Upon electrical stimulation at 20 min, *S. epidermidis* recovers its membrane potential over time and resumes growth. 3μM ThT was used for the long-term timelapse. Scale bar, 20μm. All data are presented as mean values ± SD.

More control experiments were conducted to understand the nature of the excitatory response. Using fluorescein as a pH probe, we verified that external pH, which is known to affect membrane potential, remains unaltered during and after the stimulation (**Figure 3-8**). Furthermore, we found that the excitation laser for ThT and pHrodo alone does not trigger an increase in fluorescence (**Figure 3-9**). The simultaneous rise in ThT and pHrodo fluorescence during electrical stimulation aligned with reported connections between internal pH and membrane potential. Specifically, it is known that the decrease in internal pH is

balanced by hyperpolarization of the membrane potential as part of bacterial pH homeostasis (**Figure 3-10**).[50,51] Overall, the experiments suggested that the observed phenomenon is an authentic electrophysiological response elicited by electrical stimulation.

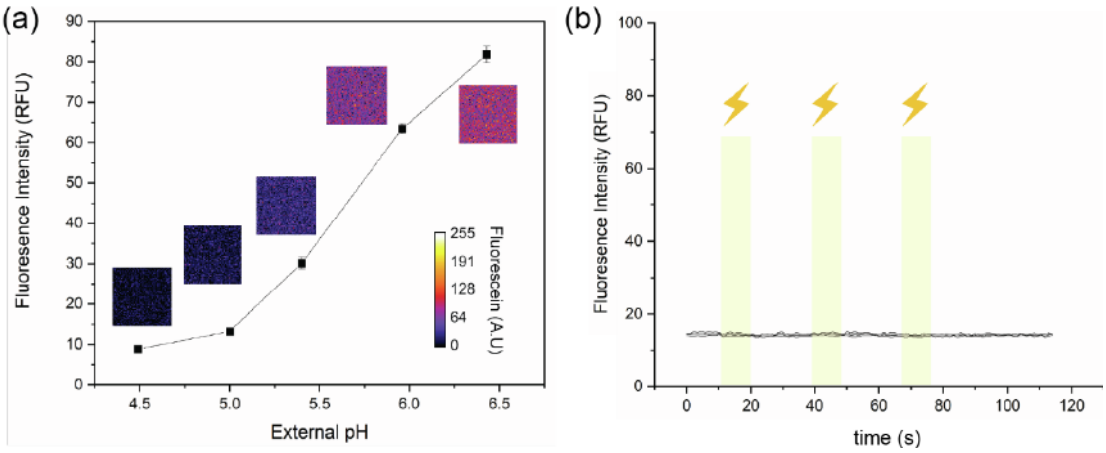

Figure 3-8. Intensity trace of fluorescein dye shows that no change in external pH occurs upon electrical stimulation. A. Calibration of fluorescein intensity (8μM) verses external pH (n=4). **B**. No change in fluorescein intensity occurred upon electrical stimulation at pH 5, showing that external pH does not fluctuate during stimulation (n=3). All data are presented as mean values ± SD.

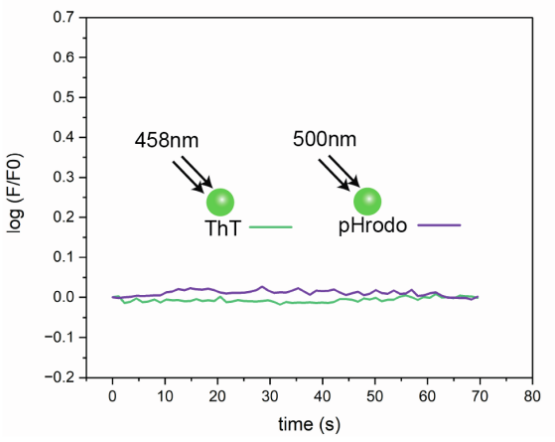

Figure 3-9. Excitation laser for ThT and pHrodo alone does not influence their membrane potential and internal pH. No change in fluorescence intensity was observed for ThT and pHrodo stained cells without electrical stimulation.

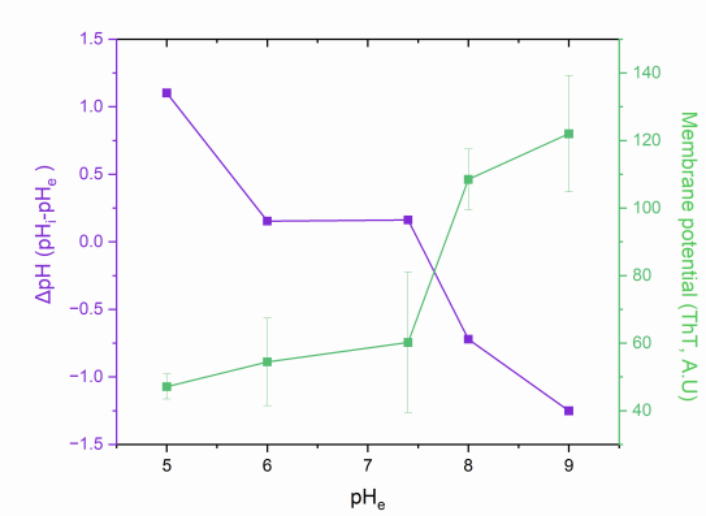

Figure 3-10. Correlation between the transmembrane pH gradient (ΔpH) and membrane potential. As the ΔpH decreases, membrane potential hyperpolarizes, evidenced by increased ThT fluorescence. This compensation of ΔpH through alterations in membrane potential is well-documented across various bacteria as a homeostatic mechanism to maintain the proton motive force (PMF), approximated as PMF (mV) = Δψ – (59 × ΔpH), where Δψ is the membrane potential. During electrical excitation, pHrodo staining indicates decrease in internal pH (pHi) while external pH (pHe) remains unchanged, resulting in reduction of ΔpH. Therefore, we observe a hyperpolarization response, consistent with the experimental and literature trends. ΔpH was measured by BCECM-AM staining (n≥4). All data are presented as mean values ± SD

Next, we investigated why bacteria only responded at pH 5 and how the epidermal pH confers excitability to *S. epidermidis*. By using the intracellular pH dye BCECF-AM, we found that the transmembrane proton gradient ΔH^+ is small at $pH_e \geq 6$, and collapses at acidic $pH_e \leq 4.5$. The ΔH^+, however, strongly peaks at $pH_e = 5$ (**Figure 3-3G**). Since electrical excitation of *S. epidermidis* involves proton influx, the large ΔH^+ near epidermal pH can be correlated with a greater driving force for the electrical response. Indeed, we observed that *S. epidermidis* can be excited only when significant ΔH^+ is present, at pH 5 and 5.5 (**Figure 3-3G, Figure 3-11**). Conversely, abolishing the proton gradient by adding the protonophore carbonyl cyanide *m*-chlorophenyl hydrazone (CCCP) completely inhibited the excitation

response (**Figure 3-12**). The results indicated that the presence of ΔH^+ is critical for the excitability of *S. epidermidis*.

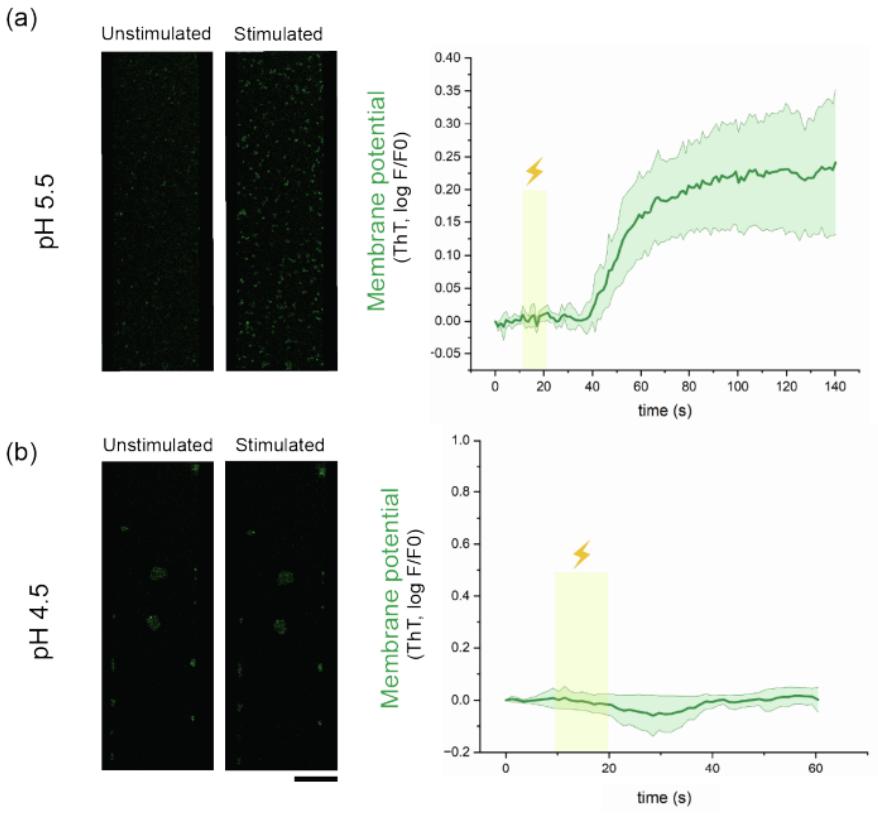

Figure 3-11. Electrical stimulation of *S. epidermidis* at intermediate pH levels. A. Mean ThT intensity trace shows that *S. epidermidis* can be electrically excited at pH 5.5 to hyperpolarize the membrane potential (n=3). **B.** Mean ThT intensity trace shows that *S. epidermidis* cannot be electrically excited at pH 4.5 to hyperpolarize the membrane potential (n=3). Scale bar, 20µm. All data are presented as mean values ± SD.

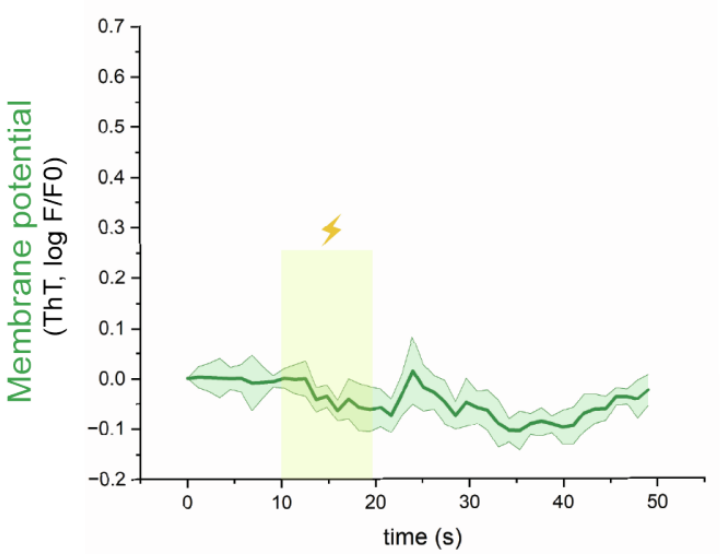

Figure 3-12. Mean ThT intensity trace upon electrical stimulation at pH= 5 with carbonyl cyanide m-chlorophenyl hydrazone (CCCP). The addition of CCCP, 150μM, mutes the hyperpolarization response (n=5). All data are presented as mean values ± SD.

To demonstrate how large ΔH^+ drives proton influx when cells are perturbed, we conducted kinetic measurements of BCECF-AM fluorescence (**Figure 3-3H**). Upon adding CCCP and nigericin, two ionophores known to induce proton influx, there is a significant drop in BCECF-AM fluorescence, indicative of cytoplasmic acidification, at $pH_e = 5$. At $pH_e = 7.4$, however, the change is less pronounced. The differences were expected as ΔH^+ at $pH_e = 5$ is orders of magnitude larger than at $pH_e = 7.4$ (**Figure 33G**). The result suggests that selective excitability at the epidermal pH range of 5–5.5 arises due to a large ΔH^+ gradient, which provides driving force for proton influx when perturbations, such as electrical stimulation, are applied. Greater molecular details about the selective excitability have been reviewed by Micheal and Chen.[52]

Interestingly, we also noted that epidermal pH confers electrical excitability to other opportunistic pathogens—*S. capitis* and *S. saprophyticus*. *S. capitis*, part of the normal skin flora, causes opportunistic infections in prosthetic medical devices and neonatal sepsis.[53] *S. saprophyticus*, prevalent in the acidic environment of the skin, vagina, and urogenital tract, is responsible for 10%–20% of urinary tract infection

in sexually active young women worldwide.[54] Upon electrical stimulation, *S. capitis* were hyperpolarized, only at pH 5 (**Figure 3-13-A and Figure 3-13B**). Similar to *S. epidermidis*, the driving force for proton influx, ΔH^+, was two orders of magnitude larger at $pH_e = 5$ than at $pH_e = 7.4$ (**Figure 3-13C**). Identical trends were observed for *S. saprophyticus* (**Figure 3.13D-F**). The results demonstrate the existence of selective excitability in the skin-residing microbes that were previously not known to be excitable. While exploring trends in the electrical response of resident bacteria is beyond the scope of this paper, future investigation into this topic will help determine how selectively electrical stimulation can modulate bacteria on skin.

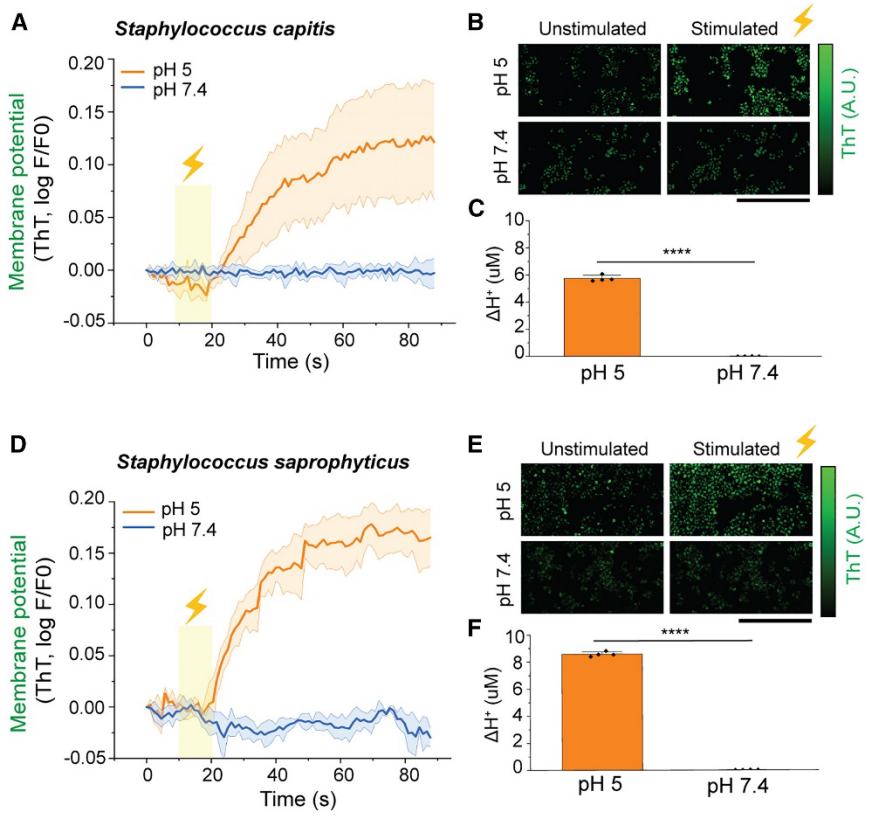

Figure 3-13 Epidermal pH confers selective excitability to two other skin-residing opportunistic pathogens. A. Mean ThT intensity traces show that electrical stimulation hyperpolarizes *S. capitis* at $pH_e = 5$, but not at $pH_e = 7.4$ ($n = 5$). **B**. Confocal images show that electrical stimulation at $pH_e = 5$ hyperpolarizes *S. capitis*, but not at $pH_e = 7.4$. Scale bar, 20 μm. The color bar illustrates the intensity range

of ThT-stained cells. **C**. The transmembrane proton gradient of *S. capitis* at $pH_e = 5$ is significantly larger than at $pH_e = 7.4$ ($n = 4$). **D**. ThT intensity traces show that electrical stimulation hyperpolarizes *S. saprophyticus* at $pH_e = 5$, but not at $pH_e = 7.4$ ($n = 5$). **E**. Confocal images show that electrical stimulation at $pH_e = 5$ hyperpolarizes *S. saprophyticus*, but not at $pH_e = 7.4$. Scale bar, 20 μm. The color bar illustrates the intensity range of ThT-stained cells. **F**. The transmembrane proton gradient of *S. saprophyticus* at $pH_e = 5$ is significantly larger than at $pH_e = 7.4$ ($n = 4$). All data are presented as means ± SDs.

3.2.3 Programmable electrical stimulation suppresses virulence factors in *S. epidermidis*

We next aimed to understand the long-term effects of electrical stimulation on *S. epidermidis* at a population level. We observed that electrical stimulation reduces both growth and ATP levels in *S. epidermidis* with successive stimulation cycles (**Figure 3-14A**). This was expected, since perturbations in membrane potential and intracellular pH have been reported to interfere with normal cellular functions, including proliferation and respiration.[55,56] The effect was not observed at $pH_e = 7.4$, where no excitation response was observed. Moreover, transcriptional analysis post-electrical stimulation revealed a decrease in the expression of virulence genes responsible for surface adhesion (*SdrG*), polysaccharide intracellular adhesin (*icaB*, *icaC*), protease (*Clp*), oxidative damage resistance (*MsrA*), and virulence regulation (*SarA*) (**Figure 3-14B**).[13,57,58] The results show that the excitatory response accompanies a suppressive effect on the virulence of the opportunistic pathogen.

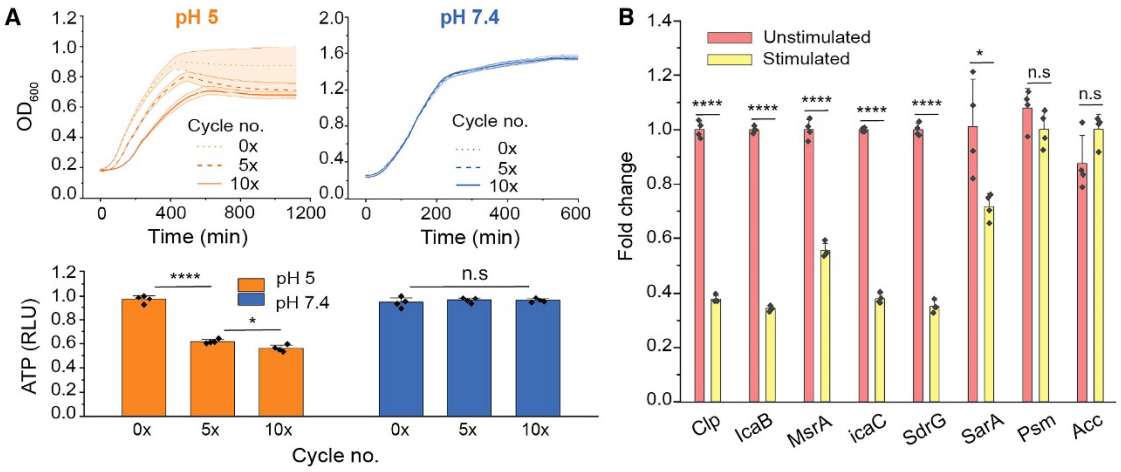

Figure 3-14. Population response of *S. epidermidis* reveals the suppressive effect of electrical stimulation. A. Electrical stimulation reduces the growth and ATP levels in *S. epidermidis* at $pH_e = 5$, but not at $pH_e = 7.4$ ($n = 4$). **B**. Electrical stimulation at $pH_e = 5$ reduces virulence gene expression in *S. epidermidis*, measured by the RT-qPCR ($n = 4$). The fold change was normalized relative to the expression level of the guanylate kinase (*gmk*) housekeeping gene. Each stimulation cycle consists of a 75 mVpp/μm amplitude at 0.1 kHz AC for a duration of 10 seconds. All data are presented as means ± SDs.

We further investigated whether electrical stimulation could assist in controlling biofilm formation, the defining virulence factor in *S. epidermidis*.[59] Given that electrical stimulation hyperpolarizes *S. epidermidis*, making the cells more negatively charged, we hypothesized that this would electrostatically increase the vulnerability of the cell to positively charged aminoglycoside antibiotics such as gentamicin. Indeed, co-staining *S. epidermidis* with ThT and gentamicin-Texas red (GTTR) shows that repeated stimulation leads to successive hyperpolarization and accumulation of gentamicin (**Figure 3-15A**). Hence, we programmed a protocol to enhance the inhibitory effect of a drug through electrical pretreatment. The protocol involved 5 cycles of stimulation pretreatment to induce hyperpolarization, followed by incubation with a sublethal dose of gentamicin for 18 h. While electrical pretreatment or a sublethal dosage of gentamicin alone failed to reduce biofilm coverage by more than 30%, their combined application resulted in a 94% decrease in biofilm coverage (**Figure 3-15B and Figure 3-15C**). This demonstrates that

electrical stimulation can enhance the effect of the drug, enabling biofilm inhibition with reduced dosages of antibiotics.

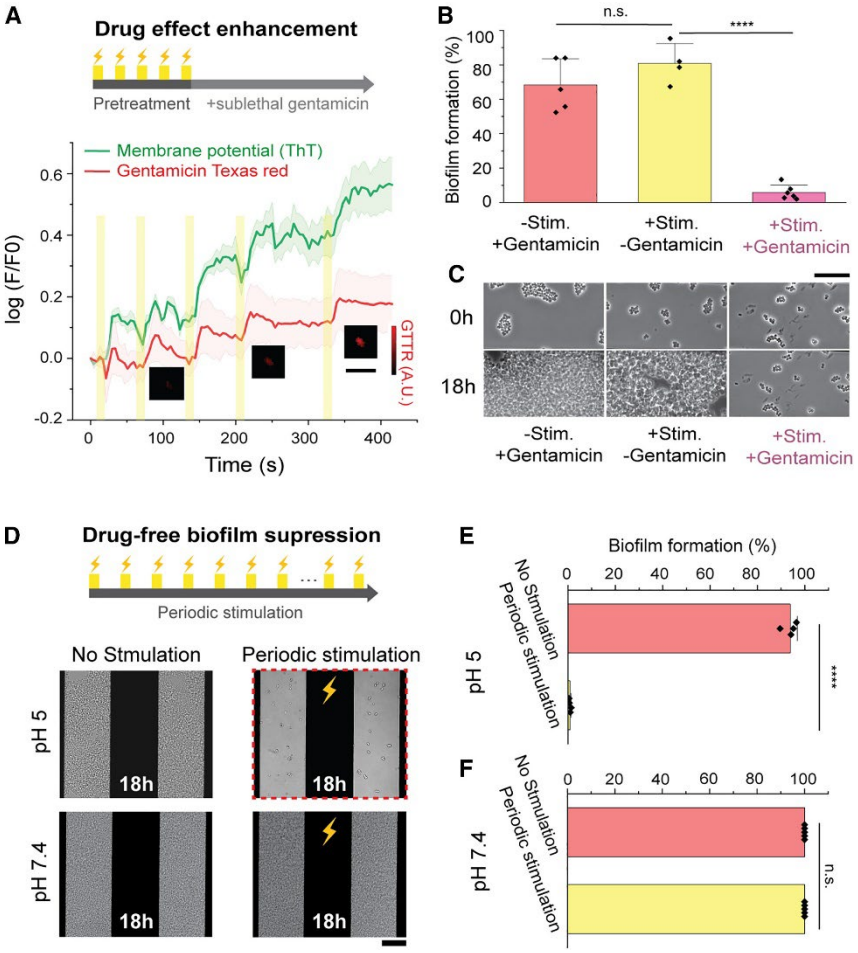

Figure 3-15 Selective excitability enables programmable biofilm suppression. A. Mean intensity trace of *S. epidermidis* co-stained with ThT and GTTR. Electrical stimulation at pH_e = 5 results in hyperpolarization accompanied by the accumulation of gentamicin (n = 5). Scale bar, 5 μm. The color bar illustrates the intensity range of GTTR-stained cells. **B**. Electrical pretreatment at pH_e = 5 enhances the suppressive effect of sublethal gentamicin (30 μg/mL) toward *S. epidermidis* biofilm formation ($n \geq 4$). Stim., stimulation. **C**. Phase contrast images show that electrical pretreatment at pH_e = 5 combined with a sublethal gentamicin stops bacterial growth. Scale bar, 20 μm. **D.** Phase contrast images

of *S. epidermidis* biofilm after 18 h of periodic electrical stimulation, applied every 10 min. Periodic stimulation abolishes biofilm formation at pH_e = 5, but not at pH_e = 7.4. Scale bar, 20 μm. **E**. Periodic electrical stimulation abolishes biofilm growth at pH_e = 5 (n = 4). **F**. Periodic electrical stimulation does not reduce biofilm growth at pH_e = 7.4 (n = 4), indicating a non-lethal bioelectrical stimulation condition. Each stimulation cycle consists of a 75 mVpp/μm amplitude at 0.1 kHz AC for a duration of 10 seconds. All data are presented as means ± SDs.

Next, we investigated the possibility of controlling biofilm formation solely through electrical means, without the use of drugs. As mentioned earlier, *S. epidermidis* can recover its membrane potential and resume growth upon stimulation (**Figure 3-7**). Thus, we developed a protocol that applies electrical stimulation at periodic intervals, every 10 min, to prevent recovery and achieve long-term suppression. The periodic stimulation at pH_e = 5 eradicated biofilm formation by 99% without the need for antibiotics (**Figure 3-15D to E**). The effect of inhibition was localized where the bulk interdigitated electrode arrays were present (**Figure 3-16**). No reduction in biofilm formation was observed at pH_e = 7.4 (**Figure 3-15F**), where excitation response was not observed, indicating that the periodic electrical stimulation itself is non-lethal for the bacteria. In the absence of an excitatory response at pH 7.4, a voltage as high as 9.5 V_{ac} was required to achieve a similar, albeit less effective, level of biofilm suppression using the identical protocol (**Figure 3-17**). The low-voltage and drug-free electrical suppression of biofilm growth was uniquely enabled at the epidermal pH where *S. epidermidis* displays selective excitability.

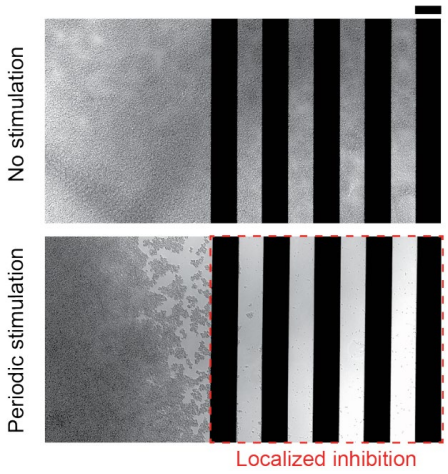

Figure 3-16. Periodic electrical stimulation at pH 5 results in localized inhibition of *S. epidermidis* biofilm formation. Biofilm inhibition only occurs at interdigitated electrode arrays. Outside the electrode region, biofilm growth occurs. Scale bar, 40µm.

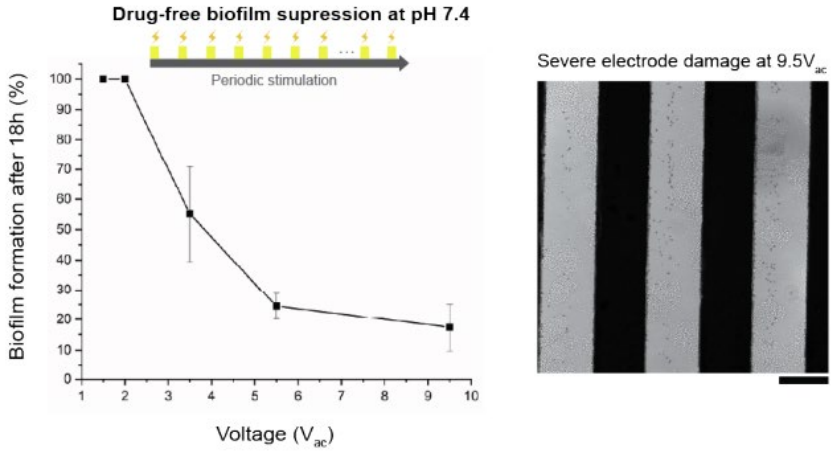

Figure 3-17. Significantly higher voltages are required for biofilm suppression in the absence of selective excitability. At pH 7.4, where the excitatory response was absent, a voltage as high as 9.5Vac was required to achieve around 90% biofilm inhibition. Moreover, severe electrode corrosion was observed at these high voltages. This demonstrates the advantages of our method, which leverages the selective excitability of *S. epidermidis* to achieve 99% biofilm suppression with a voltage as low as 1.5 Vac, while maintaining device stability over repeated stimulation cycles (n=3). Scale bar, 40µm. All data are presented as mean values ± SD.

3.2.4 Bioelectronic localized antimicrobial stimulation therapy

Chronic skin inflammation and wounds are linked with elevated pH levels and colonization of virulent *S. epidermidis* that can exacerbate the conditions.[60–63] To address the issue, we developed an electroceutical device that can restore the acidic pH of the skin, sensitizing *S. epidermidis* to electrical stimulation and suppression. The device was used to deliver bioelectronic localized antimicrobial stimulation therapy (BLAST), which controls proliferation of the opportunistic pathogen through a drug-free bioelectrical stimulation. The stimulation parameters for BLAST were set identically to the drug-free suppression protocol in **Figure 3-15D**.

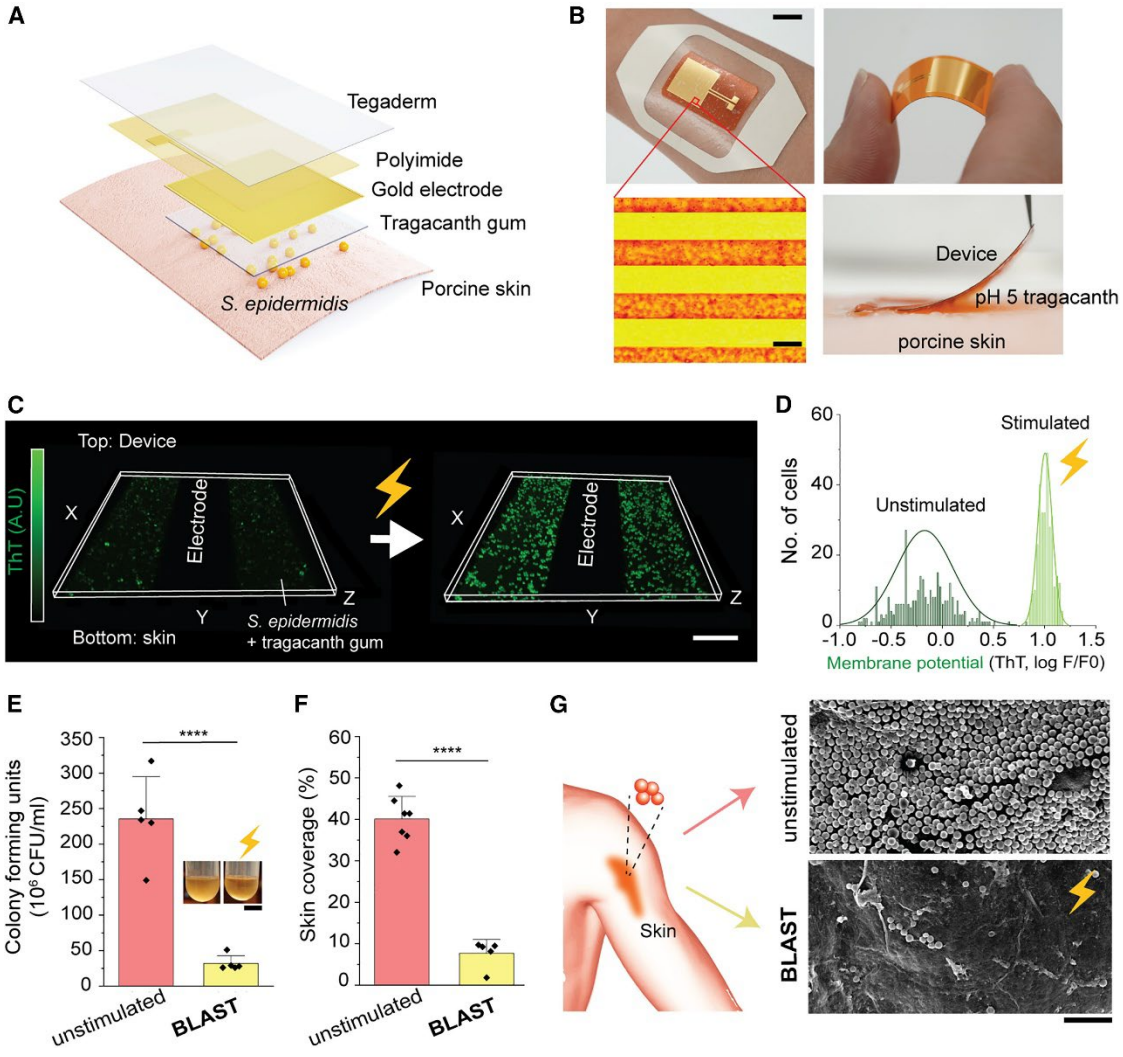

Figure 3-18. BLAST reduces colonization of porcine skin by *S. epidermidis.* **A**. Schematic diagram showing structural components of the electroceutical skin patch used to stimulate *S. epidermidis*. **B**. Photograph showing wearability and flexibility of the skin patch. Scale bar, 1 cm (top), 40 μm (bottom). **C**. Three-dimensional reconstruction of confocal z stack images shows hyperpolarization of ThT-stained *S. epidermidis* upon electrical stimulation. Scale bar, 20 μm. The color bar illustrates the intensity range of ThT-stained cells. **D**. ThT intensity histogram shows population-wide hyperpolarization response elicited upon electrical stimulation of *S. epidermidis* ($n \geq 600$). **E.** BLAST significantly reduces the colony-forming units of *S. epidermidis* on porcine skin after 18 h ($n = 5$). Insets show visible reduction in the opacity of *S. epidermidis* collected and cultured from porcine skin. Scale bar, 1 cm. **F.** BLAST significantly reduces the *S. epidermidis* biofilm coverage on porcine skin after 18 h ($n \geq 5$). **G**. SEM imaging shows that BLAST decreases *S. epidermidis* biofilm coverage on the porcine skin surface. Scale bar, 5 μm. All data are presented as means ± SDs.

The electroceutical device featured an interdigitated electrode array on a flexible polyimide (PI) substrate (**Figure 3-18A and Figure 3-18B**). pH 5-adjusted tragacanth gum served as a hydrogel interlayer between the skin and device, which provided an acidic environment that confers excitability to *S. epidermidis*. Tragacanth gum was selected for its biocompatibility and its natural ability to form an acidic pH upon gelation.[64] With 500 cycles of periodic stimulation lasting 5 days, the device showed no significant decline in impedance, indicating its stability (**Figure 3-19**). The stimulation condition was benign for humans; we utilized a voltage of 1.5 V_{ac}, which is an order of magnitude below the most conservative 15-V_{ac} voltage limit deemed imperceptible and safe for wet contact.[49] When we applied the device to a surface inoculated with *S. epidermidis*, together with tragacanth gum, electrical stimulation elicited the hyperpolarization response as shown by confocal z stack imaging (**Figure 3-18C and Figure 3-18D**). This confirmed that our device can stimulate *S. epidermidis*.

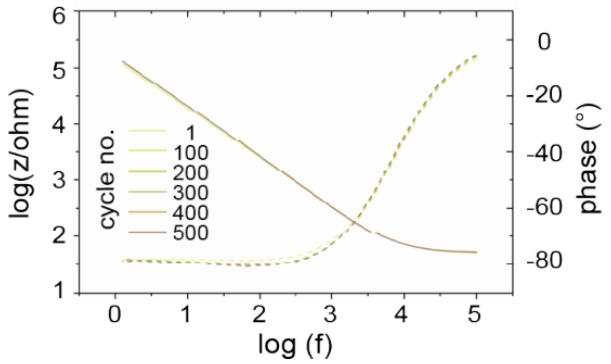

Figure 3-19. Stability of the bioelectronic skin patch for BLAST treatment, in contact with TSB agarose pad. Electrochemical impedance spectroscopy shows the stability of device impedance over 500 cycles of periodic electrical stimulation, which could last 5 days when applied at 10 min intervals. Each datapoint is an average of five repeated measurements.

To showcase the potential of BLAST in controlling opportunistic pathogens, we interfaced the device with porcine skin inoculated with *S. epidermidis*. Porcine skin was selected for its similarity to human skin.[65] After 18 h of BLAST treatment, we discovered a nearly 10-fold reduction in the colony-forming units on porcine skin for stimulated groups (**Figure 3-18E**). Scanning electron microscopy (SEM) imaging further confirmed the reduction in the porcine skin colonization by *S. epidermidis*, showing a substantial decrease in biofilm coverage (**Figure 3-18F and Figure 3-18G**). Furthermore, we examined whether BLAST could be applied to control *S. epidermidis* biofilm formation on other clinically relevant surfaces. Following an identical protocol, we inoculated *S. epidermidis* on the silicone surface utilized for catheter tubing and the surface of ultra-high molecular weight polyethylene utilized for prosthetic implants. Upon applying periodic electrical stimulation, significant reduction in the colony-forming units was observed for stimulated groups (**Figure 3-20**). This demonstration highlights a bioelectronic device exploiting selective excitability of the opportunistic pathogen, enabling drug-free control.

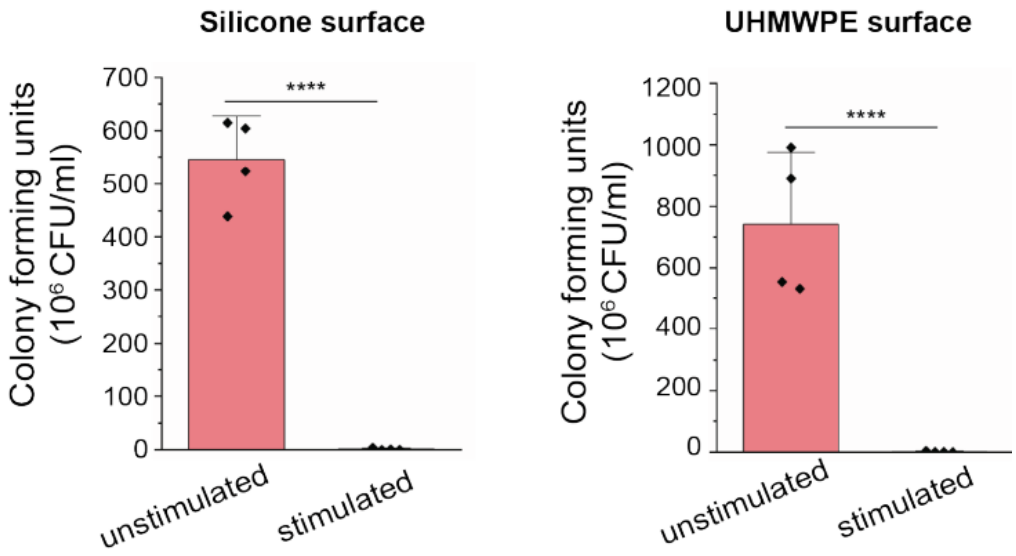

Figure 3-20. BLAST treatment on other medically relevant surfaces. When the identical device was applied to the silicone and ultra-high molecular weight polyethylene surfaces (UHMWPE) commonly used for catheter and prosthetic implants, periodic electrical stimulation significantly decreased colony forming units of *S. epidermidis* on the surfaces. All data are presented as mean values ± SD.

3.3 Discussion and Outlook

We engineered a microelectronic device to investigate the electrical excitability of the skin-residing opportunistic pathogen *S. epidermidis*. We discovered that *S. epidermidis* can be excited by exogenous electrical stimuli, resulting in cytoplasmic acidification and reversible changes in membrane potential. The presence of a large transmembrane proton gradient near the epidermal pH conferred selective excitability to *S. epidermidis* and other skin-residing opportunistic pathogens. The bioelectrical stimulation programmably suppressed growth and biofilm formation in *S. epidermidis*. Finally, we developed a drug-free electroceutical device that exploits the selective excitability of *S. epidermidis*, reducing its colonization on a porcine skin model through BLAST treatment.

We demonstrated that matching the acidic pH of the skin confers electrical excitability to opportunistic pathogens not previously known to be excitable. This selective excitability arises within a narrow pH range of 5–5.5, a hostile condition that deviates from the optimum growth pH for the organism.

Given that bacteria have evolved mechanisms to maintain their H^+ gradient under varying environments, each species may possess a different regime for electrical excitation.[66,67] While *B. subtilis* and *E. coli* are the only two non-electroactive bacteria reported to be electrically excitable,[33,68] selective excitability could be a key to uncovering hidden excitatory responses in other microorganisms. Exploring the excitability of functional microbes may facilitate electrical control of bacterial physiology for diverse applications.

We utilized the finding of *S. epidermidis*' selective excitability to develop a bioelectronic device for controlling bacterial physiology and pathology. Through a low-voltage AC stimulation that is safe and imperceptible to humans, we elicited a non-lethal excitation response in *S. epidermidis* through reversible changes in membrane potential. This bioelectrical method allowed us to control growth, ATP, and biofilm formation of *S. epidermidis* at a benign voltage that was ineffective to the bacteria outside their selective pH. In the absence of the excitatory response, significantly higher voltage was required to achieve a similar level of biofilm suppression while risking device degradation. Our method contrasts with conventional electrical stimulation typically used to either electrolytically kill bacteria through toxic chemicals or electroporate cells at dangerously high voltages.[27,28] Our results will promote further research into bioelectrical control of medically relevant bacteria, extending beyond lethal electroporation.

Our bioelectronic treatment not only enables drug-free control of opportunistic pathogens but also demonstrates effectiveness and advantages over drug-based methods. Periodic electrical stimulation reduced biofilm formation by over 90%, with the reduction localized at the interdigitated electrodes. By programming the stimulation protocol, we could transition from drug-enhanced to drug-free modes of biofilm suppression. In addition, growth, ATP levels, and antibiotic accumulation could be controlled stepwise by adjusting the number of stimulation cycles. The localized, programmable, and highly controllable therapy demonstrates the unique advantages of bioelectronic treatment over antibiotics-based methods. This approach is very easy to customize for individual patients and their treatment needs.

While we demonstrated an electroceutical device that exploits the excitability of opportunistic pathogens, much more work is needed to apply the device in practical settings. Molecular-level studies are

needed to identify which ion channels could be involved in mediating electrical responses in bacteria. Improved fundamental understanding of ionic responses could also enable an engineering approach to amplify the electrical response. Also, it should be noted that AC stimulation may be less convenient for wearable device applications due to the complexity of design and higher power consumption. To improve practicality, developing power-efficient methods and optimized circuit designs is essential. A better molecular understanding of bacterial stimulation mechanisms—including the role of ion channels and the contributions of capacitive and faradic components—may enable the exploration of alternative signal types for stimulation.

Exploring the environmental factors that grant electrical responsivity to bacteria may offer valuable insights into the evolutionary interplay between microorganisms and their host environments. For example, the stable proton gradient at pH 5 suggests that *S. epidermidis* can endure unfavorable epidermal pH levels to maintain the driving force for ATP synthesis, surviving as a part of the commensal skin flora. From the host's perspective, evolution has maintained acidic skin pH, which is crucial for enzymatic regulation, barrier integrity, and microbial defense.[47] However, the impact of epidermal pH on conferring electrical excitability to bacterial inhabitants remains largely unexplored. The presence of natural electrical phenomena on the skin, such as *trans*-epidermal electric potential[73] and electrostatic discharge,[74] prompts intriguing questions regarding their potential influence on the electrophysiology of commensal microbes. Investigating this interaction warrants further scientific exploration.

Within the broader scope of this thesis, **Chapter 3** explores the dynamic interactions at the interface between electronics and living microbial materials. We demonstrate that microbes can sense and integrate subtle electrical signals from electronic devices, triggering excitatory responses that enable potent modulation. This excitable biointerface holds significant promise for drug-free strategies in pathogen control.

3.4 Experimental

3.4.1. Strains and growth conditions

S. epidermidis (strain NIHLM087, provided by Dr. Julia Segre at NIH, NCBI taxonomy ID: 979201) was cultured overnight in tryptic soy broth (TSB) using a shaker incubator (37°C, 200 rpm). A 1-mL sample of the overnight liquid culture (optical density 600 [OD_{600}] ~3.00) was pelleted and resuspended in an equal volume of pH-adjusted TSB buffer. The resuspended bacterial solution was then added to an aerated culture tube and incubated in the shaker incubator (37°C, 200 rpm) for 3 h.

For imaging membrane potential or antibiotics accumulation, 10 μM ThT (Acros Organics), 200 nM trimethylrhodamine (TMRM, Invitrogen), or 2 μg/mL of GTTR (AAT Bioquest) was added after 2 h of incubation. At 3 h of incubation, 1 μL cells were inoculated onto pH-adjusted TSB agarose pads containing the same concentration of ThT, TMRM, or GTTR. The inoculated agarose pad was placed on the interdigitated gold electrode device for imaging and stimulation. Imaging of bacterial viability was done using the LIVE/DEAD BacLight Bacterial Viability Kit (Molecular Probes) following the identical procedure, using suggested dye concentration from the manufacturer. The agarose pad was prepared by melting ultrapure agarose (Invitrogen), which was then solidified on a 22 × 22-mm cover glass and cut to an 8 × 8-mm size. When abolishing the transmembrane pH gradient, the agarose pad was supplemented with 150 μM of CCCP (Cayman Chemical).

For imaging of intracellular pH, 1 mL of the overnight cultured *S. epidermidis* was resuspended in 1 mL of pH 7.4 TSB. Then, 2 μL pHrodo Green AM Ester and 20 μL PowerLoad concentrate (Invitrogen) were added to the suspension and left at room temperature for 30 min. After this, the cells loaded with pHrodo were washed twice with pH 7.4 TSB and resuspended in 1 mL of the pH-adjusted TSB buffers. The bacteria were incubated for 3 h (37°C, 200 rpm) in an aerated culture tube and inoculated on a TSB agarose pad without any added dyes. The inoculated agarose pad was placed on the interdigitated gold electrode device for imaging and stimulation. An identical procedure was used for the culturing and stimulation

of *S. capitis* (American Type Culture Collection [ATCC] no. 35661), *S. saprophyticus* (ATCC no. 15305), and *E. coli* (MG1655).

3.4.2. Device fabrication and characterization

To fabricate the interdigitated stimulation device for the assessment of bacterial excitability, no. 1.5 thickness microscope cover glass (Brain Research Lab, no. 4860-1.5D) was sonicated in acetone and isopropyl alcohol for 15 min. After blow drying with N_2, the cover glass was subjected to hexamethyldisilazane (HMDS) vapor priming. A SiO_2 wafer (NOVA Electronic Materials) of identical dimensions (60 × 48 mm) was spin-coated with AZ nLOF 2070 (2,500 rpm, 45 s). Following HMDS treatment, the cover glass substrate was placed on top of the photoresist-coated SiO_2 wafer and baked at 110°C for 3 min. This process was used to bond cover glass to the wafer substrate, reducing thermal expansion during subsequent fabrication processes. Next, the substrate was spin-coated with AZ nLOF 2020 and soft-baked at 110°C for 2 min. The substrate was exposed with a Heidelberg MLA150 Direct Write Lithographer. After a post-exposure bake at 110°C for 2 min, the pattern was developed in AZ 300 MIF for 50 s. After washing in deionized water, 10 nm titanium and 100 nm gold were deposited using an EvoVac Electron Beam Evaporator (Angstrom). The photoresist and bonding to the SiO_2 wafer were lifted off in Remover PG at 80°C overnight, releasing the cover glass substrate with interdigitated gold electrode patterns. Acrylic plastic (Alfa Aesar) was cut with a VLS 4.60 laser cutter to make a 2 × 2 well, which was bound to the cover glass substrate using Kwik-Sil (World Precision Instruments). The device was wired using copper wire (Remington) and PELCO conductive silver paint (Ted Pella), which was insulated with epoxy (JB Weld). For the fabrication of the electroceutical skin patch for BLAST, an identical procedure was used, replacing the cover glass substrate with PI film up to the lift-off stage using Remover PG. The released PI film with interdigitated gold electrodes was wired and attached to Tegaderm (3M). The dimensions of the interdigitated electrode were checked using LEXT OLS5100 confocal microscope (Olympus) and Merlin SEM (ZEISS) and processed with the manufacturer's software. Electrochemical

impedance spectroscopy of the device, in contact with agarose pad, was performed using SP200 Potentiostat (BioLogic).

3.4.3. Electrical stimulation of *S. epidermidis*

Electric stimulation was applied using an SP200 Potentiostat (BioLogic). One stimulation cycle consisted of 75 mVpp/μm, AC, 0.1 kHz for 10 s. For enhancing the inhibitory effect of antibiotics, *S. epidermidis* was preconditioned with five cycles of stimulation (1-min intervals) and then incubated with a sublethal concentration (30 μg/mL) of gentamicin for 18 h at 37°C. For drug-free biofilm suppression, stimulation cycles were applied periodically at 10-min intervals for 18 h at 37°C.

3.4.4. Fluorescence microscopy

Short-term time-lapse images with an imaging duration under 10 min were acquired using a Stellaris 8 WLL confocal microscope (Leica Microsystems) with a 63× objective (63×/1.4 numerical aperture, UV transmission, oil immersion, 0.14 mm working distance, 506350). ThT fluorescence was detected with an excitation laser of 458 nm and an emission detection window of 490–545 nm using the HyD X2 detector. pHrodo fluorescence was detected with an excitation laser of 500 nm and an emission detection window of 530–600 nm using the HyD X2 detector. GTTR fluorescence was detected with an excitation laser of 595 nm and an emission detection window of 630–750 nm using the HyD S3 detector. For overnight time-lapse experiments, phase contrast images of *S. epidermidis* were captured using an Axio Observer 7 microscope (Zeiss) with a 100× or 63× objective (1.4 numerical aperture, oil immersion) in an incubator box maintained at 37°C. Images were background subtracted and adjusted for brightness and contrast using ImageJ.

3.4.5. Intracellular pH assay with BCECF-AM

A total of 1 mL of the overnight cultured *S. epidermidis* was pelleted and resuspended in an equal volume of pH-adjusted TSB buffers. The resuspended bacterial solution was added to an aerated culture tube and incubated in a shaker incubator (37°C, 200 rpm) for 3 h. After the incubation, 25 μM BCECF-AM

(Invitrogen) was added to the culture tubes and incubated at 30°C for 30 min. BCECF-AM fluorescence was measured using a Synergy NEO HTS Plate Reader according to the manufacturer's instructions. The Intracellular pH Calibration Buffer Kit (Invitrogen, P35379) was used to calibrate BCECF-AM fluorescence with intracellular pH, allowing for the quantification of transmembrane pH gradient ΔpH. Transmembrane proton gradient ΔH^+ was measured by taking the negative anti-log of pH to find proton concentration $[H^+]$ to calculate $\Delta H^+ = [H^+]_{external} - [H^+]_{internal}$. For the kinetics experiment using BCECF-AM, fluorescence measurements were taken every minute in the Synergy NEO HTS Plate Reader. After 5 min, the plate was taken out and 150 μM CCCP or 3 μM nigericin (Invitrogen) was added to the wells. Upon addition, changes in BCECF-AM fluorescence were continuously monitored for 30 min.

3.4.6. Measurement of ATP and growth

Upon applying the desired cycles of electrical stimulation, the agarose pad and electrode surface were flushed with TSB medium to collect *S. epidermidis*. Using a Synergy NEO HTS Plate Reader, the OD of the stimulated and non-stimulated cells was adjusted to $OD_{600} = 0.2$. ATP levels in stimulated cells were measured using the BacTiter-Glo Microbial Cell Viability Assay and normalized to those of non-stimulated controls. For the measurement of growth, 200 μL of the $OD_{600} = 0.2$ samples were added to a 96-well plate, and OD was monitored overnight using a Tecan Infinite 200 microplate reader at 37°C under orbital shaking. The percentage of biofilm formation was quantified using ImageJ by examining the area of coverage from phase contrast images taken after 18 h incubation.

3.4.7. Electrical stimulation and characterization of porcine skin

Porcine skin (Fisher Scientific, NC1275387) was soaked in TSB buffer overnight before the experiment. *S. epidermidis*, 3 μL, was inoculated onto the porcine skin surface. pH 5-adjusted tragacanth gum (3% w/v, Sigma-Aldrich) was applied to the electrode surface (8 μL/cm^2). Finally, the electrode was placed on the inoculated porcine skin and BLAST treatment was applied, applying an electrical stimulation every 10 min for 18 h at 37°C. To quantify colony-forming units on the porcine skin, the skin and electrode

were flushed with pH 7.4 TSB to collect the attached bacteria. The TSB containing the collected *S. epidermidis* was incubated for 6 h in an aerated bacterial culture tube before being inoculated on a TSB agar plate for colony counting. The identical procedure was used for BLAST treatment on silicone and polyethylene surfaces.

To determine the pH of porcine skin before and after applying tragacanth gum, a 1-cm^2 piece of skin was soaked in PBS at pH 7.4 overnight. After soaking, the skin was gently shaken to remove excess PBS, and MQuant pH-indicator strips (range: pH 5–10) were placed on the skin's surface. Then, 8 μL/cm^2 of pH 5 tragacanth gum was spread on the skin, and the pH was allowed to equilibrate for 10 min. Excess gum was gently dried off with a towel, and another pH-indicator strip was placed on the skin. The strip's color was analyzed by photographing it, converting the image to HSB stack in ImageJ, and quantifying the hue, saturation, and brightness. The quantified color was then compared to control strips applied to PBS and pH 5-tragacanth gum.

For SEM characterization, the porcine skin was fixed with 3% glutaraldehyde for 16 h at 4°C. The fixed porcine skin was subjected to increasing concentrations of acetone and isopropyl alcohol solvent series and dried with a Leica EM CPD300 Critical Point Drier following the manufacturer's protocol on preparing bacterial samples. The dried samples were sputtered with 8 nm of platinum/palladium using a Cressington Sputter Coater 208 and imaged with a Merlin FE SEM (Zeiss). The percentage of skin coverage was quantified using ImageJ by examining the area of coverage from the SEM images.

3.4.8. Real-time quantitative reverse transcription PCR

Upon applying 10 cycles of electric stimulation at 1-minute intervals, the agarose pad and electrode were flushed with TSB medium to collect *S. epidermidis*. Using a Synergy Neo HTS Plate Reader, the optical density of the stimulated and non-stimulated cells was adjusted to OD600 = 0.03. Then, 200 μl of the cells were added to a 96-well plate and incubated for 8 hours at 37°C with orbital shaking in a Tecan Infinite 200 microplate reader, until they reached the mid-exponential growth phase. Subsequently, RNA

was extracted using the Qiagen RNeasy Mini Kit (Cat. No. 74104). Quantitative RT-PCR was performed using the One-Step TB Green® PrimeScript™ RT-PCR Kit II (Takara, Cat. No. RR086A) and a QuantStudio Pro 6 PCR system (Applied Biosystems). ΔCt values were calculated relative to the guanylate kinase (gmk) housekeeping gene, 2 and fold changes were calculated relative to the non-stimulated control samples. The virulence gene sequence of *S. epidermidis* was obtained from the NCBI database, and primers were designed and evaluated using Primer3 software. Primer sequences: icaC-u:TCACTACCGGAAACAGCGAT, icaC-d:TTCTTAGGTGGTTACATTGGCT icaB-u: ACTTTGCGTCGTGTGCTTTA, icaB-d: GCACTCGCGTTAAACTATCAC Psm-u: CGCTAACGCCACTTTCTACG, Psm-d: GCAGCACAAGATCAAGATTGG gmk-u: CCTTCAGGTGTTGGAAAGG, gmk-d: CACCTTCACGCATATGACGC Clp-u: ACATAAACTCGTCGGGTGGT, Clp-d: AGCGATCACACTTGCGATTG msrA-u: TCTTGATGGTATGCTTCCGC, msrA-d: TCCTTTGGATGATGGTGGTC SarA-u: TGCTTCTGTGATACGGTTGT, SarA-d: TGAACACGATGAGAGAACTGTT SdrG-u: CAACAAGTCAGCCGTCTAGC, SdrG-d: CTTGTTCCGCCGCTAATTGA Acc-u: TGTTTCTTAGTTGCTGCAGGT, Acc-d: TTAGGAGACATGCACACGGT

3.4.9. Statistical analysis

OriginPro 2024 was employed for all statistical analyses. Unless stated otherwise, the error bars represent 1 SD. For biological data analysis, multiple t tests were performed. A significance threshold of $p < 0.05$ was used to determine statistical significance. In the figure panels, the following symbols were used to indicate significance levels: n.s., non-significant ($p > 0.05$); $*p < 0.05$; $**p < 0.01$; $***p < 0.001$; $****p < 0.0001$.

3.5 Bibliography

(1) Kim, S.; Eig, E.; Yue, J.; Yang, A.; Comerci, C. J.; Laune, M.; Yang, C.; Kamath, A.; Shi, J.; Li, P.; Cheng, Z.; Sun, C.; Guo, T.; Tian, V.; Süel, G. M.; Tian, B. Bioelectronic Drug-Free Control of Opportunistic Pathogens through Selective Excitability. *Device* **2024**, *2* (11), 100596. https://doi.org/10.1016/j.device.2024.100596.

(2) Li, P.; Kim, S.; Tian, B. Beyond 25 Years of Biomedical Innovation in Nano-Bioelectronics. *Device* **2024**, *2*, 100401. https://doi.org/10.1016/j.device.2024.100401.

(3) Li, P.; Zhang, J.; Hayashi, H.; Yue, J.; Li, W.; Yang, C.; Sun, C.; Shi, J.; Huberman-Shlaes, J.; Hibino, N.; Tian, B. Monolithic Silicon for High Spatiotemporal Translational Photostimulation. *Nature* **2024**, *626* (8001), 990–998. https://doi.org/10.1038/s41586-024-07016-9.

(4) Prominski, A.; Shi, J.; Li, P.; Yue, J.; Lin, Y.; Park, J.; Tian, B.; Rotenberg, M. Y. Porosity-Based Heterojunctions Enable Leadless Optoelectronic Modulation of Tissues. *Nat. Mater.* **2022**, *21* (6), 647–655. https://doi.org/10.1038/s41563-022-01249-7.

(5) Nirenberg, S.; Pandarinath, C. Retinal Prosthetic Strategy with the Capacity to Restore Normal Vision. *Proc. Natl. Acad. Sci. U. S. A.* **2012**, *109* (37), 15012–15017. https://doi.org/10.1073/pnas.1207035109.

(6) Majmudar, A.; Kim, S.; Li, P.; Tian, B. Perspectives on Non-Genetic Optoelectronic Modulation Biointerfaces for Advancing Healthcare. *Med-X* **2024**, *2*. https://doi.org/10.1007/s44258-024-00030-6.

(7) Guyot, M.; Simon, T.; Ceppo, F.; Panzolini, C.; Guyon, A.; Lavergne, J.; Murris, E.; Daoudlarian, D.; Brusini, R.; Zarif, H.; Abélanet, S.; Hugues-Ascery, S.; Divoux, J. L.; Lewis, S. J.; Sridhar, A.; Glaichenhaus, N.; Blancou, P. Pancreatic Nerve Electrostimulation Inhibits Recent-Onset Autoimmune Diabetes. *Nat. Biotechnol.* **2019**, *37* (12), 1446–1451. https://doi.org/10.1038/s41587-019-0295-8.

(8) Balasubramanian, S.; Weston, D. A.; Levin, M.; Davidian, D. C. C. Charging Ahead: Examining the Future Therapeutic Potential of Electroceuticals. *Adv. Ther.* **2024**, *7* (7), 2300344. https://doi.org/10.1002/adtp.202300344.

(9) Balasubramanian, S.; Weston, D. A.; Levin, M.; Davidian, D. C. C. Electroceuticals: Emerging Applications beyond the Nervous System and Excitable Tissues. *Trends Pharmacol. Sci.* **2024**, *45* (5), 391–394. https://doi.org/10.1016/j.tips.2024.03.001.

(10) Prindle, A.; Liu, J.; Asally, M.; Ly, S.; Garcia-Ojalvo, J.; Süel, G. M. Ion Channels Enable Electrical Communication in Bacterial Communities. *Nature* **2015**, *527* (7576), 59–63. https://doi.org/10.1038/nature15709.

(11) Erin Chen, Y.; Fischbach, M. A.; Belkaid, Y. Skin Microbiota-Host Interactions. *Nature* **2018**, *553* (7689), 427–436. https://doi.org/10.1038/nature25177.

(12) Shi, J.; Kim, S.; Li, P.; Dong, F.; Yang, C.; Nam, B.; Han, C.; Eig, E.; Shi, L. L.; Niu, S.; Yue, J.; Tian, B. Active Biointegrated Living Electronics for Managing Inflammation. *Science (80-.).* **2024**, *384* (6699), 1023–1030. https://doi.org/10.1126/science.adl1102.

(13) Severn, M. M.; Horswill, A. R. Staphylococcus Epidermidis and Its Dual Lifestyle in Skin Health and Infection. *Nat. Rev. Microbiol.* **2023**, *21* (2), 97–111. https://doi.org/10.1038/s41579-022-00780-3.

(14) Otto, M. Staphylococcus Epidermidis - The “accidental” Pathogen. *Nat. Rev. Microbiol.* **2009**, *7* (8), 555–567. https://doi.org/10.1038/nrmicro2182.

(15) Dong, Y.; Speer, C. P.; Glaser, K. Beyond Sepsis: Staphylococcus Epidermidis Is an Underestimated but Significant Contributor to Neonatal Morbidity. *Virulence* **2018**, *9* (1), 621–633. https://doi.org/10.1080/21505594.2017.1419117.

(16) Landemaine, L.; Da Costa, G.; Fissier, E.; Francis, C.; Morand, S.; Verbeke, J.; Michel, M. L.; Briandet, R.; Sokol, H.; Gueniche, A.; Bernard, D.; Chatel, J. M.; Aguilar, L.; Langella, P.; Clavaud, C.; Richard, M. L. Staphylococcus Epidermidis Isolates from Atopic or Healthy Skin Have Opposite Effect on Skin Cells: Potential Implication of the AHR Pathway Modulation. *Front. Immunol.* **2023**, *14* (May), 1–19. https://doi.org/10.3389/fimmu.2023.1098160.

(17) Hon, K. L.; Tsang, Y. C. K.; Pong, N. H.; Leung, T. F.; Ip, M. Exploring Staphylococcus Epidermidis in Atopic Eczema: Friend or Foe? *Clin. Exp. Dermatol.* **2016**, *41* (6), 659–663. https://doi.org/10.1111/ced.12866.

(18) Clavaud, C.; Jourdain, R.; Bar-Hen, A.; Tichit, M.; Bouchier, C.; Pouradier, F.; El Rawadi, C.; Guillot, J.; Ménard-Szczebara, F.; Breton, L.; Latgé, J. P.; Mouyna, I. Dandruff Is Associated with Disequilibrium in the Proportion of the Major Bacterial and Fungal Populations Colonizing the Scalp. *PLoS One* **2013**, *8* (3). https://doi.org/10.1371/journal.pone.0058203.

(19) Cunha, B. A. Antibiotic Side Effects. *Med. Clin. North Am.* **2001**, *85* (1), 149–185. https://doi.org/10.1016/s0025-7125(05)70309-6.

(20) Weidinger, S.; Beck, L. A.; Bieber, T.; Kabashima, K.; Irvine, A. D. Atopic Dermatitis. *Nat. Rev. Dis. Prim.* **2018**, *4* (1). https://doi.org/10.1038/s41572-018-0001-z.

(21) Larsson, D. G. J.; Flach, C. F. Antibiotic Resistance in the Environment. *Nat. Rev. Microbiol.* **2022**, *20* (5), 257–269. https://doi.org/10.1038/s41579-021-00649-x.

(22) Darby, E. M.; Trampari, E.; Siasat, P.; Gaya, M. S.; Alav, I.; Webber, M. A.; Blair, J. M. A. Molecular Mechanisms of Antibiotic Resistance Revisited. *Nat. Rev. Microbiol.* **2023**, *21* (5), 280–295. https://doi.org/10.1038/s41579-022-00820-y.

(23) Lee, J. Y. H.; Monk, I. R.; Gonçalves da Silva, A.; Seemann, T.; Chua, K. Y. L.; Kearns, A.; Hill, R.; Woodford, N.; Bartels, M. D.; Strommenger, B.; Laurent, F.; Dodémont, M.; Deplano, A.; Patel, R.; Larsen, A. R.; Korman, T. M.; Stinear, T. P.; Howden, B. P. Global Spread of Three Multidrug-Resistant Lineages of Staphylococcus Epidermidis. *Nat. Microbiol.* **2018**, *3* (10), 1175–1185. https://doi.org/10.1038/s41564-018-0230-7.

(24) Koo, J.; MacEwan, M. R.; Kang, S. K.; Won, S. M.; Stephen, M.; Gamble, P.; Xie, Z.; Yan, Y.; Chen, Y. Y.; Shin, J.; Birenbaum, N.; Chung, S.; Kim, S. B.; Khalifeh, J.; Harburg, D. V.; Bean, K.; Paskett, M.; Kim, J.; Zohny, Z. S.; Lee, S. M.; Zhang, R.; Luo, K.; Ji, B.; Banks, A.; Lee, H. M.; Huang, Y.; Ray, W. Z.; Rogers, J. A. Wireless Bioresorbable Electronic System Enables Sustained Nonpharmacological Neuroregenerative Therapy. *Nat. Med.* **2018**, *24* (12), 1830–1836. https://doi.org/10.1038/s41591-018-0196-2.

(25) Pavlov, V. A.; Tracey, K. J. Bioelectronic Medicine: Preclinical Insights and Clinical Advances. *Neuron* **2022**, *110* (21), 3627–3644. https://doi.org/10.1016/j.neuron.2022.09.003.

(26) Moritz, C.; Field-Fote, E. C.; Tefertiller, C.; van Nes, I.; Trumbower, R.; Kalsi-Ryan, S.; Purcell, M.; Janssen, T. W. J.; Krassioukov, A.; Morse, L. R.; Zhao, K. D.; Guest, J.; Marino, R. J.; Murray, L. M.; Wecht, J. M.; Rieger, M.; Pradarelli, J.; Turner, A.; D’Amico, J.; Squair, J. W.; Courtine, G. Non-Invasive Spinal Cord Electrical Stimulation for Arm and Hand Function in

Chronic Tetraplegia: A Safety and Efficacy Trial. *Nat. Med.* **2024**, *30* (5), 1276–1283. https://doi.org/10.1038/s41591-024-02940-9.

(27) Sultana, S. T.; Babauta, J. T.; Beyenal, H. Electrochemical Biofilm Control: A Review. *Biofouling* **2015**, *31* (9), 745–758. https://doi.org/10.1080/08927014.2015.1105222.

(28) Czerwińska-Główka, D.; Krukiewicz, K. A Journey in the Complex Interactions between Electrochemistry and Bacteriology: From Electroactivity to Electromodulation of Bacterial Biofilms. *Bioelectrochemistry* **2020**, *131*, 107401. https://doi.org/10.1016/j.bioelechem.2019.107401.

(29) Kim, S.; Eig, E.; Tian, B. The Convergence of Bioelectronics and Engineered Living Materials. *Cell Reports Phys. Sci.* **2024**, *5*, 102149. https://doi.org/10.1016/j.xcrp.2024.102149.

(30) Li, P.; Kim, S.; Tian, B. Nanoenabled Trainable Systems: From Biointerfaces to Biomimetics. *ACS Nano* **2022**, *16* (12), 19651–19664. https://doi.org/10.1021/acsnano.2c08042.

(31) Benarroch, J. M.; Asally, M. The Microbiologist's Guide to Membrane Potential Dynamics. *Trends Microbiol.* **2020**, *28* (4), 304–314. https://doi.org/10.1016/j.tim.2019.12.008.

(32) Jones, J. M.; Larkin, J. W. Toward Bacterial Bioelectric Signal Transduction. *Bioelectricity* **2021**, *3* (2), 116–119. https://doi.org/10.1089/bioe.2021.0013.

(33) Stratford, J. P.; Edwards, C. L. A.; Ghanshyam, M. J.; Malyshev, D.; Delise, M. A.; Hayashi, Y.; Asally, M. Electrically Induced Bacterial Membrane-Potential Dynamics Correspond to Cellular Proliferation Capacity. *Proc. Natl. Acad. Sci. U. S. A.* **2019**, *116* (19), 9552–9557. https://doi.org/10.1073/pnas.1901788116.

(34) Sender, R.; Fuchs, S.; Milo, R. Are We Really Vastly Outnumbered? Revisiting the Ratio of Bacterial to Host Cells in Humans. *Cell* **2016**, *164* (3), 337–340. https://doi.org/10.1016/j.cell.2016.01.013.

(35) Larkin, J. W.; Zhai, X.; Kikuchi, K.; Redford, S. E.; Prindle, A.; Liu, J.; Greenfield, S.; Walczak, A. M.; Garcia-Ojalvo, J.; Mugler, A.; Süel, G. M. Signal Percolation within a Bacterial Community. *Cell Syst.* **2018**, *7* (2), 137-145.e3. https://doi.org/10.1016/j.cels.2018.06.005.

(36) Yang, C. Y.; Bialecka-Fornal, M.; Weatherwax, C.; Larkin, J. W.; Prindle, A.; Liu, J.; Garcia-Ojalvo, J.; Süel, G. M. Encoding Membrane-Potential-Based Memory within a Microbial Community. *Cell Syst.* **2020**, *10* (5), 417-423.e3. https://doi.org/10.1016/j.cels.2020.04.002.

(37) Comerci, C. J.; Gillman, A. L.; Galera-Laporta, L.; Gutierrez, E.; Groisman, A.; Larkin, J. W.; Garcia-Ojalvo, J.; Süel, G. M. Localized Electrical Stimulation Triggers Cell-Type-Specific Proliferation in Biofilms. *Cell Syst.* **2022**, *13* (6), 488-498.e4. https://doi.org/10.1016/j.cels.2022.04.001.

(38) Fang, Y.; Prominski, A.; Rotenberg, M. Y.; Meng, L.; Acarón Ledesma, H.; Lv, Y.; Yue, J.; Schaumann, E.; Jeong, J.; Yamamoto, N.; Jiang, Y.; Elbaz, B.; Wei, W.; Tian, B. Micelle-Enabled Self-Assembly of Porous and Monolithic Carbon Membranes for Bioelectronic Interfaces. *Nat. Nanotechnol.* **2021**, *16* (2), 206–213. https://doi.org/10.1038/s41565-020-00805-z.

(39) Ortega, M. A.; Fernández-Garibay, X.; Castaño, A. G.; De Chiara, F.; Hernández-Albors, A.; Balaguer-Trias, J.; Ramón-Azcón, J. Muscle-on-a-Chip with an on-Site Multiplexed Biosensing System for: In Situ Monitoring of Secreted IL-6 and TNF-α. *Lab Chip* **2019**, *19* (15), 2568–2580. https://doi.org/10.1039/c9lc00285e.

(40) Liu, N.; Gao, Y. Recent Progress in Micro-Supercapacitors with In-Plane Interdigital Electrode

Architecture. *Small* **2017**, *13* (45), 1–10. https://doi.org/10.1002/smll.201701989.

(41) Chiera, S.; Bosco, F.; Mollea, C.; Piscitello, A.; Sethi, R.; Nollo, G.; Caola, I.; Tessarolo, F. Staphylococcus Epidermidis Is a Safer Surrogate of Staphylococcus Aureus in Testing Bacterial Filtration Efficiency of Face Masks. *Sci. Rep.* **2023**, *13* (1), 1–10. https://doi.org/10.1038/s41598-023-49005-4.

(42) Lambers, H.; Piessens, S.; Bloem, A.; Pronk, H.; Finkel, P. Natural Skin Surface PH Is on Average below 5, Which Is Beneficial for Its Resident Flora. *Int. J. Cosmet. Sci.* **2006**, *28* (5), 359–370. https://doi.org/10.1111/j.1467-2494.2006.00344.x.

(43) O'Goshi, K. ichiro; Okada, M.; Iguchi, M.; Tagami, H. The Predilection Sites for Chronic Atopic Dermatitis Do Not Show Any Special Functional Uniqueness of the Stratum Corneum: Measurements of the Water Barrier Function, Hydration State, Skin Surface Lipids, Corneocyte Size and PH in Patients and Normal Indi. *Exog. Dermatology* **2002**, *1* (4), 195–202. https://doi.org/10.1159/000066233.

(44) Prakash, C.; Bhargave, P.; Tiwari, S.; Majumdar, B.; Bhargava, R. K. Skin Surface PH in Acne Vulgaris: Insights from an Observational Study and Review of the Literature. *J. Clin. Aesthet. Dermatol.* **2017**, *10* (7), 33–39.

(45) Sim, P.; Strudwick, X. L.; Song, Y. M.; Cowin, A. J.; Garg, S. Influence of Acidic PH on Wound Healing In Vivo: A Novel Perspective for Wound Treatment. *Int. J. Mol. Sci.* **2022**, *23* (21), 13655. https://doi.org/10.3390/ijms232113655.

(46) Proksch, E. PH in Nature, Humans and Skin. *J. Dermatol.* **2018**, *45* (9), 1044–1052. https://doi.org/10.1111/1346-8138.14489.

(47) Lukić, M.; Pantelić, I.; Savić, S. D. Towards Optimal PH of the Skin and Topical Formulations: From the Current State of the Art to Tailored Products. *Cosmetics* **2021**, *8* (3), 69. https://doi.org/10.3390/cosmetics8030069.

(48) Wang, T.; Chen, H.; Yu, C.; Xie, X. Rapid Determination of the Electroporation Threshold for Bacteria Inactivation Using a Lab-on-a-Chip Platform. *Environ. Int.* **2019**, *132* (August), 105040. https://doi.org/10.1016/j.envint.2019.105040.

(49) Dorr, D. Determining Voltage Levels of Concern for Human and Animal Response to AC Current. *IEEE* **2009**, 1–6. https://doi.org/10.1109/PES.2009.5275848.

(50) Krulwich, T. A.; Sachs, G.; Padan, E. Molecular Aspects of Bacterial PH Sensing and Homeostasis. *Nat. Rev. Microbiol.* **2011**, *9* (5), 330–343. https://doi.org/10.1038/nrmicro2549.

(51) Padan, E.; Zilberstein, D.; Schuldiner, S. PH Homesstasis in Bacteria. *Biochim. Biophys. Acta* **1981**, *650* (2–3), 151–166. https://doi.org/10.1016/0304-4157(81)90004-6.

(52) Chen, M. W.; Dai, Y. Selective Excitation of Bacteria Enables Growth Suppression without Antibiotics. *Cell* **2025**, *188* (1), 1–3. https://doi.org/10.1016/j.cell.2024.11.035.

(53) Chong, C. E.; Bengtsson, R. J.; Horsburgh, M. J. Comparative Genomics of Staphylococcus Capitis Reveals Species Determinants. *Front. Microbiol.* **2022**, *13*, 1005949. https://doi.org/10.3389/fmicb.2022.1005949.

(54) Lawal, O. U.; Barata, M.; Fraqueza, M. J.; Worning, P.; Bartels, M. D.; Goncalves, L.; Paixão, P.; Goncalves, E.; Toscano, C.; Empel, J.; Urbaś, M.; Domiìnguez, M. A.; Westh, H.; de Lencastre, H.; Miragaia, M. Staphylococcus Saprophyticus From Clinical and Environmental Origins Have Distinct Biofilm Composition. *Front. Microbiol.* **2021**, *12* (June), 1–13.

https://doi.org/10.3389/fmicb.2021.663768.

(55) Lagadic-Gossmann, D.; Huc, L.; Lecureur, V. Alterations of Intracellular PH Homeostasis in Apoptosis: Origins and Roles. *Cell Death Differ.* **2004**, *11* (9), 953–961. https://doi.org/10.1038/sj.cdd.4401466.

(56) Lee, D. yeon D.; Galera-Laporta, L.; Bialecka-Fornal, M.; Moon, E. C.; Shen, Z.; Briggs, S. P.; Garcia-Ojalvo, J.; Süel, G. M. Magnesium Flux Modulates Ribosomes to Increase Bacterial Survival. *Cell* **2019**, *177* (2), 352-360.e13. https://doi.org/10.1016/j.cell.2019.01.042.

(57) Tormo, M. Á.; Martí, M.; Valle, J.; Manna, A. C.; Cheung, A. L.; Lasa, I.; Penadés, J. R. SarA Is an Essential Positive Regulator of Staphylococcus Epidermidis Biofilm Development. *J. Bacteriol.* **2005**, *187* (7), 2348–2356. https://doi.org/10.1128/JB.187.7.2348-2356.2005.

(58) Wang, C.; Li, M.; Dong, D.; Wang, J.; Ren, J.; Otto, M.; Gao, Q. Role of ClpP in Biofilm Formation and Virulence of Staphylococcus Epidermidis. *Microbes Infect.* **2007**, *9* (11), 1376–1383. https://doi.org/10.1016/j.micinf.2007.06.012.

(59) Fey, P. D.; Olson, M. E. Current Concepts in Biofilm Formation of Staphylococcus Epidermidis. *Future Microbiol.* **2010**, *5* (6), 917–933. https://doi.org/10.2217/fmb.10.56.

(60) Williams, M. R.; Bagood, M. D.; Enroth, T. J.; Bunch, Z. L.; Jiang, N.; Liu, E.; Almoughrabie, S.; Khalil, S.; Li, F.; Brinton, S.; Cech, N. B.; Horswill, A. R.; Gallo, R. L. Staphylococcus Epidermidis Activates Keratinocyte Cytokine Expression and Promotes Skin Inflammation through the Production of Phenol-Soluble Modulins. *Cell Rep.* **2023**, *42* (9), 113024. https://doi.org/10.1016/j.celrep.2023.113024.

(61) Gawande, P. V.; Leung, K. P.; Madhyastha, S. Antibiofilm and Antimicrobial Efficacy of Dispersinb®-KSL-w Peptide-Based Wound Gel against Chronic Wound Infection Associated Bacteria. *Curr. Microbiol.* **2014**, *68* (5), 635–641. https://doi.org/10.1007/s00284-014-0519-6.

(62) Brackman, G.; De Meyer, L.; Nelis, H. J.; Coenye, T. Biofilm Inhibitory and Eradicating Activity of Wound Care Products against Staphylococcus Aureus and Staphylococcus Epidermidis Biofilms in an in Vitro Chronic Wound Model. *J. Appl. Microbiol.* **2013**, *114* (6), 1833–1842. https://doi.org/10.1111/jam.12191.

(63) Schierle, C. F.; De La Garza, M.; Mustoe, T. A.; Galiano, R. D. Staphylococcal Biofilms Impair Wound Healing by Delaying Reepithelialization in a Murine Cutaneous Wound Model. *Wound Repair Regen.* **2009**, *17* (3), 354–359. https://doi.org/10.1111/j.1524-475X.2009.00489.x.

(64) Taghavizadeh Yazdi, M. E.; Nazarnezhad, S.; Mousavi, S. H.; Sadegh Amiri, M.; Darroudi, M.; Baino, F.; Kargozar, S. Gum Tragacanth (Gt): A Versatile Biocompatible Material beyond Borders. *Molecules* **2021**, *26* (6), 1510. https://doi.org/10.3390/molecules26061510.

(65) Uhm, C.; Jeong, H.; Lee, S. H.; Hwang, J. S.; Lim, K. M.; Nam, K. T. Comparison of Structural Characteristics and Molecular Markers of Rabbit Skin, Pig Skin, and Reconstructed Human Epidermis for an Ex Vivo Human Skin Model. *Toxicol. Res.* **2023**, *39* (3), 477–484. https://doi.org/10.1007/s43188-023-00185-1.

(66) Michels, M.; Bakker, E. P. Generation of a Large, Protonophore-Sensitive Proton Motive Force and PH Difference in the Acidophilic Bacteria Thermoplasma Acidophilum and Bacillus Acidocaldarius. *J. Bacteriol.* **1985**, *161* (1), 231–237. https://doi.org/10.1128/jb.161.1.231-237.1985.

(67) Mulkidjanian, A. Y.; Dibrov, P.; Galperin, M. Y. The Past and Present of Sodium Energetics: May the Sodium-Motive Force Be with You. *Biochim. Biophys. Acta* **2008**, *1777* (7–8), 985–992.

https://doi.org/10.1016/j.bbabio.2008.04.028.

(68) Pirbadian, S.; Chavez, M. S.; El-Naggar, M. Y. Spatiotemporal Mapping of Bacterial Membrane Potential Responses to Extracellular Electron Transfer. *Proc. Natl. Acad. Sci. U. S. A.* **2020**, *117* (33), 20171–20179. https://doi.org/10.1073/PNAS.2000802117.

Chapter 4. Conclusion and Outlook

4.1 Conclusion

In conclusion, this thesis investigated living bioelectronic interfaces aimed at controlling inflammation and infection (**Figure 4-1**). **Chapter 2** explored the use of LMs as bioactive interfacial components for immunomodulation. We developed a system called *Active Bio-Integrated Living Electronics* (ABLE), which combines a bioelectronic framework with a hydrogel composite encapsulating *Staphylococcus epidermidis*. This living interface enables microbial-driven intervention in psoriasis through the release of bioactive compounds. The hydrogel, prepared by thermally releasing amylose polymers, maintains bacterial viability through its viscoelastic extracellular matrix. When combined with electrophysiological and wireless sensors, ABLE enables simultaneous treatment and monitoring of inflammatory skin disease.

Chapter 3 explored the dynamic interactions at the interface between electronics and living microbes at an electrified interface. The electrical excitability of *S. epidermidis* only emerged under acidic skin pH, suggesting that the bacterium's electrical responsiveness is environmentally gated. Through selective excitability microbes could integrate subtle electrical signals from electronic devices, triggering excitatory responses that drives potent virulence suppression. We demonstrated the application of the excitable living biointerface for drug-free pathogen control.

Together, these studies demonstrate the potential of living biointerfaces in managing complex biological conditions. While Chapter 2 pioneered different modes of integrating between bioelectronics and LMs (ie. LMs used as bioactive interfacial material), Chapter 3 delved into the 'mode of interaction' between electronic devices and living microbes (ie. bioelectronic control of

bacterial excitation). These approaches led to effective strategies in inflammation and infection control.

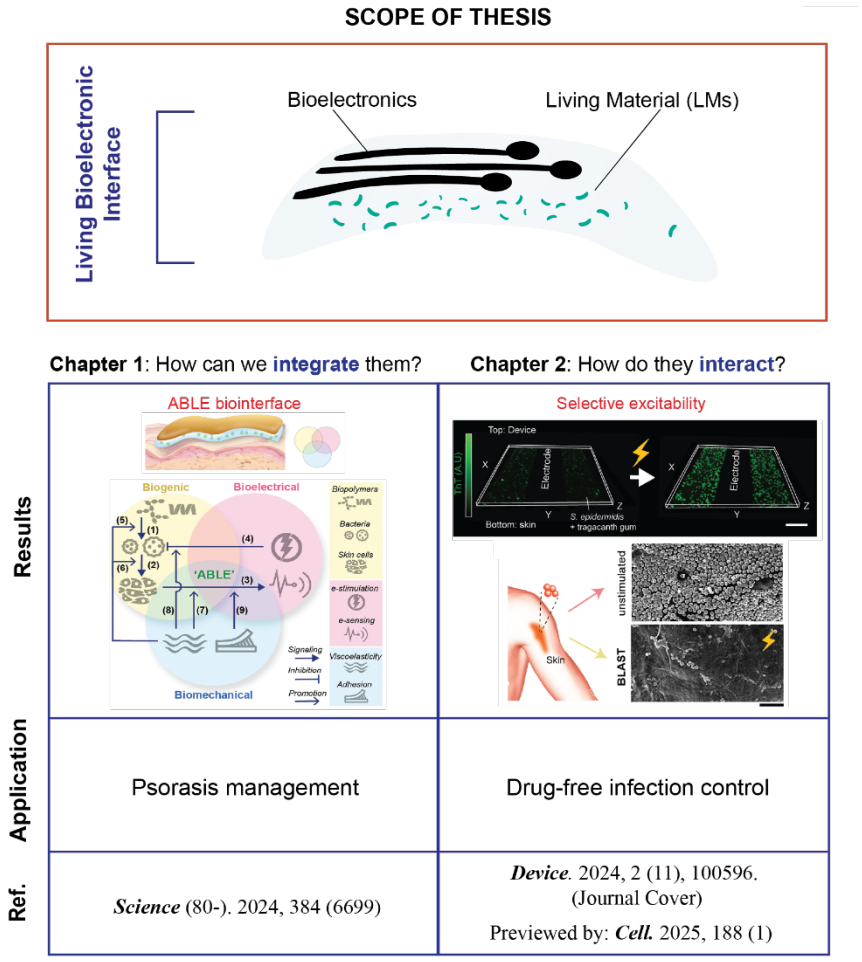

Figure 4-1. Summary of the thesis

4.2 Outlook

Looking forward, we anticipate that integration strategies between living and non-living components will continue to evolve, unlocking richer interactions and broader therapeutic applications. Interfacial mode of integration utilizes LMs as a soft, moisturized and bioactive interface between electronics and the tissue. This was demonstrated by our ABLE device (**Chapter**

2), which integrates *S. epidermidis*-encapsulated hydrogel for inflammation treatment and monitoring. Exploring different modes of integrating bioelectronics and LMs would be an important step towards diversifying the application of living bioelectronics.

Another crucial step toward advancing the field of living bioelectronics would be to study and exploit interaction between bioelectronics and LMs. Bacterial response to electrified interface was thoroughly studied in **Chapter 3**, unlocking opportunities in drug-free suppression of opportunistic pathogen. We envisage that uncovering various microbial behaviors at the electrified interface will enable a next-generation biointerface with highly dynamic and reconfigurable properties.